Title
Study of Cu-Pt Alloy Catalysis for Unsaturated Aldehyde Hydrogenation

Author
Han, Tongxin

Publication Date
2023

UNIVERSITY OF CALIFORNIA
RIVERSIDE

Study of Cu-Pt Alloy Catalysis for Unsaturated Aldehyde Hydrogenation

A Dissertation submitted in partial satisfaction
of the requirements for the degree of

Doctor of Philosophy

in

Chemistry

by

Tongxin Han

March 2023

Dissertation Committee:
    Dr. Francisco Zaera, Chairperson
    Dr. Gregory Beran
    Dr. Ludwig Bartels

The Dissertation of Tongxin Han is approved:

Committee Chairperson

University of California, Riverside

Acknowledgments

First and foremost, I would like to express my deepest gratitude to my Ph.D. advisor, Professor Francisco Zaera for offering me such a great opportunity to study and conduct research in his lab. He has always been a professional chemist and thoughtful tutor. My journey started in 2016, when I got the chance to work in this lab as a volunteer. After about three months of study, I applied to work in this great place as a graduate student and got admitted starting in 2017. During my five years of study, I can't remember how many times I was inspired by his advice and the way he thought about nature behind the piles of data and observations. He has also let me realize how important it is to properly organize and summarize my data to find the most interesting result. I believe these experiences will benefit me from now on. I can never say enough about my appreciation.

I also would like to thank Professor Gregory Beran and Professor Ludwig Bartels for participating in my oral exam and final defense as committee members, giving me the opportunity to further polish my research results.

I also appreciate the professional assistance from Dr. Yueqiang Cao when I first started my research as a graduate student. To his patience and helpful advice on liquid phase reaction, X-ray adsorption spectra analysis.

A special thanks to Dr. Ilkeun Lee, the lab manager, for his professional help during my five years of study in this group. He turned unfixable situations into fixable ones. I appreciate his advice and his consistent help with my TEM analysis and XPS analysis.

And all my other colleagues at the Zaera Group have been kind and helpful. Dr Yufei Ni, Dr. Tianyi Yu, Dr. Wang Ke, and Dr. Yang Xu, Dr. Clinton Lien, give me helpful advice both on my research and life in the U.S. The postdocs in our group – Dr. Xiangdong Qin, Dr Bo Chen, Dr. Tilan Nayakasinghe, Dr. Md. Abdul Motin, and Dr. Juan Pablo Simonovis, helped me solve numerous problems I've encountered during my research. And to all my other group members, I have truly enjoyed my time with you.

I will always remember the study from Professor Xiaoyun Hu at Northwestern University for providing me the opportunity to do research under her supervision. Without her, I would never even have started my career as a chemist.

I also appreciate the help from Dr. Yuanyuan Li, Professor Anatoly Frenkel, and other collaborators at Brookhaven National laboratory, SLAC National Accelerator Laboratory, and Argonne National Laboratory for helping me obtain useful data and observations during my research.

I would also like to thank the staff working at the Department of Chemistry, from enrollment, processing purchase order and everything else. I can't imagine a single day without their professionalism. Special thanks to Gary Qin at the Graduate Writing Center for helping me polish up the dissertation draft.

Last but not least, I want to say thank all my friends at UCR – Ge Sun, Yuchen Xiao, and many others. It was a great time having fun with you guys.

COPYRIGHT ACKNOWLEDGEMENT

The text of this dissertation, in part or in full, is a reprint of the material as is appearing in the publications below, with authorization obtained from the copyright via RightsLink. The research presented here was conducted under the direction and supervision of Dr. Francisco Zaera.

1. Chapter 6 was reproduced verbatim from our article: Han, T.; Lee, I.; Cao, Y.; Zhou, X.; Zaera, F., Thermodynamics of Carbon Monoxide Adsorption on Cu/SBA-15 Catalysts: Under Vacuum versus under Atmospheric Pressures. The Journal of Physical Chemistry C 2022, 126 (6), 3078-3086.
2. Chapter 3 was reproduced verbatim from our article: Han, T.; Li, Y.; Cao, Y.; Lee, I.; Zhou, X.; Frenkel, A. I.; Zaera, F., In situ identification of surface sites in Cu–Pt bimetallic catalysts: Gas-induced metal segregation. The Journal of Chemical Physics 2022, 157 (23), 234706.
3. Parts of Chapter 4 and Chapter 5 were copied from a draft of a manuscript written by Dr. Francisco Zaera for future submission to a scientific journal.
4. Part of Chapter 2 were copied and modified from the manual of our Tensor system prepared by Dr. Ilkeun Lee.

DEDICATION

To my Grandmother

Peiqin Han

For my enlightenment education from her

To my parents

Hua Yang and Yunbo Han

For their love all along

To my wife

Ying Gao

For her love and support

ABSTRACT OF THE DISSERTATION

Study of Cu-Pt Alloy Catalysis for Unsaturated Aldehyde Hydrogenation

by

Tongxin Han

Doctor of Philosophy, Graduate Program in Chemistry
University of California, Riverside, March 2023
Dr. Francisco Zaera, Chairperson

One of the major challenges in heterogeneous catalysis is the preparation of highly selective catalysts. Cu catalysts have been ubiquitous in many applications, including for the promotion of the low temperature water-shift reaction and hydrogenation of carbon monoxide. By combining with a second metal, Cu can also assist in the selective hydrogenation of organic molecules with multiple double and triple bonds. In this work, Pt-Cu alloy catalysts have been studied to obtain better understanding of some fundamental questions, such as what the oxidation state of Cu under reaction conditions is, where the atoms of the two metals are.

The majority of this work has focused on the Pt-Cu bimetallic catalyst, so-called single atom catalyst, where Pt atoms are diluted in Cu nanoparticles. Pt is presumed to activate H_2 while Cu is believed to aid in the selective addition of the resulting H atoms to C=O bonds. In fact, catalysts with Pt content as low as 0.1% of the total composition have shown improved selectivity. In this catalysis, it is reasonable to expect the active catalyst

to be metallic copper. However, in situ x-ray absorption spectroscopy (XAS) and CO infrared (IR) titration experiments have suggested that at low temperatures, below 100°C, copper-containing nanoparticles dispersed on silica support develop a thin layer of copper oxide film. This was found even in the presence of a hydrogen atmosphere for several different experiment setups. However, our latest synchrotron-based experiment indicated that such oxidation may be prevented, although the way to accomplish this may require further investigation. At high temperatures, Cu is fully reduced to metallic state, and the interconversion is reversible. Nonetheless, plenty of hydrogenation catalysis is carried out under mild temperature, under which reaction may take place on oxidized copper sites.

In addition to the oxidation of Cu surface, several CO IR titration experiments were carried out and suggested that Pt sites are not available on the surface until the Pt content surpasses about 10% of the total metal loading. Where are the Pt atoms during reaction, on the surface or inside Cu nanoparticles, or attached to the oxide support? XAS absorption spectroscopies and in-situ IR have been carried out. Both in vacuum and under gaseous atmospheres, Pt atoms are found to be diffusing within the Cu-Pt nanoparticles. From in situ IR in CO atmosphere, for diluted single atom catalysts, Pt was found to reversibly segregate to the surface and diffuse back into the bulk when ramp up the temperature from 295 K to 495 K and cool back.

A comparison of the thermodynamics of the adsorption of CO on the metal surface of a Cu/SBA-15 catalysts was made as well, under two different environments: under vacuum versus in the presence of atmospheric pressures of CO. Changes associated with entropic effects introduced by the presence of CO gas such as adsorbate displacement and adsorbate-assisted adsorption steps need to be introduced to explain the differences seen between the two environments.

Also, core-shell Pt@Cu catalysts were prepared successfully, and it will be utilized to study the behavior of Pt atoms under reaction conditions.

Future follow-up work of this project might include designing a flow reactor for in-site infrared experiments and optimizing current core-shell Pt@Cu catalysts to minimize the amount of single Cu atom site on the surface and test them with in situ IR and XAS absorption spectroscopies.

Table of Contents

List of Figures

List of Tables

Chapter 1 Introduction and Overview

1.1 Selective Heterogeneous Catalysis

Catalysis, a term used to describe the phenomenon in which the rate of a chemical reaction is promoted by a substance (the catalyst) that is not consumed during the process, was first created by Berzelius in 1835 and well-defined by Ostwald in 1895. By decreasing the activation energy of reactions, catalysts can thereby facilitate efficient, cost-effective, and environmentally sustainable production of chemicals. In recent decades, catalysts are playing a significant role in about 90% of the entire chemical industrial processes and contribute to approximately 35% of the world's gross domestic product (GDP)[1]. Catalysis can be mainly divided into two types; heterogeneous and homogeneous.

In the field of heterogeneous catalysis, the development of highly selective catalysts represents a significant challenge. Historically, the primary focus of catalysis has been to enhance reaction rates. However, in recent years, selectivity has increasingly become a crucial aspect in the design of contemporary catalytic processes. Many benefits can be found for selective catalysts, such as the requirement of lower amounts of feedstocks, the elimination of the requirement for additional separation steps, and the decrease of the formation of byproducts that may have a negative environmental impact.

The selective hydrogenation of double bonds plays an important role in the synthesis of many fine chemicals, especially for flavor and fragrance chemistry[2] and the production of medicine[3]. However, compared to homogeneous catalysis with discrete molecules[4], heterogeneous media often shows the limitation of relatively lower chemical selectivity. The reason is that, typically, complex catalytic sites which are capable of distinguishing among a number of similar molecular functionalities, are one of the keys in improving selectivity in the conversion of organic compounds. In addition, such need is easier to be achieved in discrete molecular homogeneous catalysts than from solid surfaces[5].

1.2 Copper-Platinum Bimetallic Catalysts

In an attempt to address the lack of complex sites in heterogeneous catalysts, one way that has been discovered is by introducing several components within the solid. Typically, a vast majority of hydrogenation reactions involving organic feedstocks are facilitated through the utilization of late transition metals.[6-8]. In the past, such approaches have been extensively developed for converting unsaturated aldehyde[9-10]. For example, Pt, Pd, and Rh possess significant catalytic activity and are widely employed in various industrial processes. However, the drawback of these metals is their lack of selectivity, leading to the hydrogenation of both double and triple bonds present in organic molecules with multiple unsaturations. For instance, supported platinum-group metals have shown relatively low selectivity[11]. To our knowledge, there are a handful of studies that have been conducted regarding this and several factors are considered to impact the selectivities. For example, the work by Ruiz et al.[12], indicated that the degree of steric hindrance around the C=C double bonds is affecting the selectivity, which is suggested by work by Bernard[13] and Ponec V.[14]. In addition, numerous works show reaction conditions (including pressure[15-16], solvent used[16-18], temperature[17, 19]) are playing an important role on the effect of selectivity. It should also be noted that the size and morphology of the loading metal nanoparticles, and the selection of supporting materials lead to different selectivity. Among a considerable number of ways to modify supported platinum-group metals, it has been long developed that introducing a suitable additive can substantially improve the selectivity[14, 20-24]. Among numerous published works, Germanium, [10, 25-28] tin, [10, 26, 28-32] and iron [33-37] are the most researched additives in relation to catalyst systems and a lot of studies have shown the mechanism regarding the modification of the performance of the catalysts. For example, In Mónica L. Casella's work [28], it was indicated that adding germanium as the promoter shows good selectivity to obtain furfuryl alcohol. Typically, selectivity towards unsaturated alcohol can be improved by adding a metal that is more electropositive, but there is still insufficient understanding of the reason. In addition, the oxidation state of the second metal is still under hot debate. Some work argues it could be an adatom in a metallic form ,[38-39] in alloy form,[40-44] in an ionic state,[45-46] or in a partially oxidized form.[44, 47]

As noted above, the utilization of Bi- and multi-metallic catalysts has a long history and has been extensively used for decades;[48-50] mixed metals may display unique electronic properties, often (but not always) a weighted average of the electronic properties of the individual components,[51-54] and/or mixed-metal ensembles of atoms on the surface with unique catalytic properties [55-57]. However, an agreement regarding how the second metal is promoting the reaction is not reached yet. As previously stated, the bulk of the recent work has been focusing on combining tin with platinum. It would benefit the field if the set of additives has been expanded. Therefore, in this work we propose to investigate the Cu-Pt catalysts. There are a number of reasons to choose Cu as the additive due to its attractive properties. For example, copper is stable under oxidation states, such as Cu^+, and Cu^{2+}, but the reduction of oxidized copper is easy, and this offers flexibility regarding the exploration of the role of different oxidation states of Cu during the reaction. In addition, Cu behaves as a good catalyst with atomic hydrogen for hydrogenation reactions.[58]

1.3 Single-Atom Alloy Catalysis with $CuPt_x$/SBA-15

To improve the design of alloyed Cu-Pt alloy catalysts and predict their activities, the Brønsted−Evans−Polanyi (BEP) relationship can be employed as a methodology to obtain valuable insight without having to discuss all the factors mentioned previously (particle size, ligand effects, pressure, temperature). BEP implies a linear correlation between the activation barrier and the reaction energy associated with a chemical transformation.[59-60] Namely, the reaction energy can be estimated from utilizing thermodynamic scaling relationships and assessing the binding energies of key intermediates.[61] It was suggested that alloying catalysts allows tuning the surface binding energies, therefore moving the position along the linear BEP line. Nevertheless, this approach is constrained by BEP scaling, which entails a compromise between low activation energy and weak binding. Therefore, it is crucial to explore a potential solution for which alloy catalysis can escape the BEP linear scaling.

In recent years, a new type of alloying in catalysis has garnered attention where single atoms of one metal are mixed with another metal in an isolated form to create so-called single-atom alloys (SAAs). Different from traditional bimetallic catalysts, in SAA, it is believed that the minority metal atoms are dispersed on the surface layer of the majority component.[62-63] For SAA catalysts, the premise guiding the design is by adding the single-atom sites then therefore improve the specific functionality lacking in the majority component, which was originally designed to selectively promote the reaction. In the case of designing hydrogenation catalysis with SAA catalysts, for example, Pt or Pd can be used as the minority component and providing single-atom sites were used to help with the activation of molecular hydrogen, for which coinage metals such as Cu or Au are not effective.

It has become clear that SAA catalysts can significantly enhance the activity of the majority component, coupled with exceptional selectivity. [64-66] However, an understanding of how that occurs, is still being developed. Some significant surface-science work using model metal surfaces such as single crystals and controlled ultra-high vacuum (UHV) environments has been performed. This elegant work has been complemented with quantum mechanics calculations, supporting a proposed mechanism for the dissociation of molecular hydrogen on individual Pt or Pd atoms on the surface.

The resulting adsorbed H atoms then spill over to the Cu or Au surface, where organic molecules are subsequently hydrogenated. On the other hand, our preliminary result has suggested that the performance of SAA catalysts under realistic hydrogenation conditions may be affected by additional factors, in particular the single-atom metal may segregate to the surface and/or diffuse into the metal bulk upon exposure to different chemical environments. It has been observed that at room temperature, typically under which hydrogenation reactions are performed, Pt atoms diffuse to the bulk for single-atom catalyst $CuPt_{0.005}$/SBA-15. Based on the proposed mechanism, if the active metal in SAAs was to diffuse deep into the bulk, its activity may be hindered. In other words, the hindrance of molecular hydrogen dissociation due to the diffusion of Pt atoms into the bulk may restrict the reaction rate, as anticipated. Surprisingly, this catalyst was found to show the best reaction performance in our preliminary result. It appears that Pt inside the bulk could promote the dissociation of hydrogen molecules in a remote way, which is different from the proposed mechanism. The details are provided in the following chapters.

1.4 Work of dissertation

In this thesis, we aimed to study Cu-Pt nanoparticles (NPs) on SBA-15. Various characterizations will be conducted to investigate the nature of Cu-Pt catalysts for hydrogenation reactions. What is the oxidation state of copper as the additive for those Pt-Cu catalysts? Where is platinum among those NPs during the reaction? These are the fundamental questions in this thesis work. The specific objectives of the thesis were the following:

1.4.1 In Situ Identification of Surface Sites in Cu-Pt Bimetallic Catalysts: Gas-Induced Metal Segregation

The problem of where the position of Pt is discussed in this part. The study of the impact of various gaseous species on the surface of Cu-Pt nanoparticles has revealed that Pt atoms exhibit diffusion within the bimetallic structure, both in a vacuum and in the presence of a gaseous atmosphere. It has been found that the surface composition of Cu-Pt catalysts is temperature-sensitive and that the position of Pt within the bimetallic structure is unstable. These findings highlight the importance of considering the effect of gaseous exposure on the stability and performance of Cu-Pt bimetallic catalysts.

1.4.2 Oxidation State of Copper in Cu-Pt Single-Atom Catalysts under Hydrogenation Conditions

A comprehensive examination of the oxidation state of copper in Cu-Pt catalysts was performed utilizing in-situ X-ray absorption (XAS) and infrared absorption (IR) spectroscopies. The results indicated that a thin layer of oxidized copper sometimes forms on the supporting material, even in hydrogen atmospheres, at low temperatures. More recent XAS experiments failed to reproduce our earlier observations, however, suggesting that the copper oxidation may be related to the way the experiments are performed; more research is needed to settle this. Additional, full reduction of copper can be expected at higher temperatures, the interconversion between the metallic and oxidized states is considered to be reversible. These findings have significant implications for hydrogenation catalysis, as the reaction may occur at oxidized copper sites under mild reaction conditions which is where hydrogenation catalysis usually takes place.

1.4.3 Thermodynamics of Carbon Monoxide Adsorption on Cu/SBA-15 Catalysts: In Vacuum versus Under Atmospheric Pressures

In this part of the work, data from in situ infrared absorption spectroscopy experiments are studied and thermodynamics properties of the adsorption of carbon monoxide on a copper-based catalyst are discussed.

1.4.4 Core-shell Pt@Cu catalyst

To better understand how Cu-Pt bimetallic catalysts, such a unique nanostructured Pt@Cu was made. Various characterizations were conducted here to confirm its structure, such as in situ infrared spectroscopy, Energy dispersive spectrometry, and Inductive coupled plasma.

1.5 Reference

1. Armor, J. N., A history of industrial catalysis. *Catalysis Today* **2011,** *163* (1), 3-9.

2. Bauer, K.; Garbe, D.; Surburg, H., *Common fragrance and flavor materials: preparation, properties and uses*. John Wiley & Sons: 2008.

3. Weissermel, K.; Arpe, H.-J., *Industrial organic chemistry*. John Wiley & Sons: 2008.

4. Blaser, H. U.; Malan, C.; Pugin, B.; Spindler, F.; Steiner, H.; Studer, M., Selective hydrogenation for fine chemicals: Recent trends and new developments. *Advanced Synthesis & Catalysis* **2003,** *345* (1-2), 103-151.

5. Sheldon, R. A.; Van Bekkum, H., *Fine chemicals through heterogeneous catalysis*. John Wiley & Sons: 2008.

6. Bond, G. C., *Metal-Catalysed Reactions of Hydrocarbons*. Springer: New York, 2005.

7. Sanfilippo, D.; Rylander, P. N., Hydrogenation and Dehydrogenation. In *Ullmann's Encyclopedia of Industrial Chemistry*, Wiley-VCH Verlag GmbH & Co. KGaA: Weinheim, 2012; Vol. 18, pp 451-471.

8. Ma, Z.; Zaera, F., Heterogeneous Catalysis by Metals. In *Encyclopedia of Inorganic and Bioinorganic Chemistry*, Scott, R. A., Ed. John Wiley & Sons, Ltd: Chichester, 2014; p eibc0079.

9. Ponec, V., On the role of promoters in hydrogenations on metals; α, β-unsaturated aldehydes and ketones. *Applied Catalysis A: General* **1997,** *149* (1), 27-48.

10. Claus, P., Selective hydrogenation of ά, β-unsaturated aldehydes and other C= O and C= C bonds containing compounds. *Topics in Catalysis* **1998,** *5* (1), 51-62.

11. Giroir-Fendler, A.; Richard, D.; Gallezot, P., Selectivity in cinnamaldehyde hydrogenation of group-VIII metals supported on graphite and carbon. In *Studies in Surface Science and catalysis,* Elsevier: 1988; Vol. 41, pp 171-178.

12. Beccat, P.; Bertolini, J. C.; Gauthier, Y.; Massardier, J.; Ruiz, P., Crotonaldehyde and methylcrotonaldehyde hydrogenation over Pt(111) and Pt80Fe20(111) single crystals. *Journal of Catalysis* **1990,** *126* (2), 451-456.

13. Coq, B.; Figuéras, F.; Moreau, C.; Moreau, P.; Warawdekar, M., Hydrogenation of substituted acrolein over alumina supported ruthenium catalysts. *Catalysis letters* **1993,** *22* (3), 189-195.

14. Marinelli, T.; Nabuurs, S.; Ponec, V., Activity and Selectivity in the Reactions of Substituted α, β-Unsaturated Aldehydes. *Journal of Catalysis* **1995,** *151* (2), 431-438.

15. Sokolskii, D.; Anisimova, N.; Zharmagambetova, A.; Ualikhanova, A., Effect of hydrogen pressure on the selectivity of 2-butene-1-al hydrogenation. *Reaction Kinetics and Catalysis Letters* **1981,** *17* (3), 419-421.

16. Neri, G.; Mercadante, L.; Donato, A.; Visco, A.; Galvagno, S., Influence of Ru precursor, support and solvent in the hydrogenation of citral over ruthenium catalysts. *Catalysis letters* **1994,** *29* (3), 379-386.

17. Singh, U. K.; Vannice, M. A., Kinetics of liquid-phase hydrogenation reactions over supported metal catalysts—a review. *Applied Catalysis A: General* **2001,** *213* (1), 1-24.

18. Chen, Y.; Wei, S.; Wu, K., Effect of promoter on selective hydrogenation of α, β-unsaturated aldehydes over cobalt borides. *Applied Catalysis A: General* **1993,** *99* (2), 85-96.

19. Hoang-Van, C.; Zegaoui, O., Studies of high surface area Pt/MoO3 and Pt/WO3 catalysts for selective hydrogenation reactions. II. Reactions of acrolein and allyl alcohol. *Applied Catalysis A: General* **1997,** *164* (1-2), 91-103.

20. Rylander, P. N., 1 - Platinum Metal Catalysts. In *Catalytic Hydrogenation Over Platinum Metals*, Rylander, P. N., Ed. Academic Press: 1967; pp 3-29.

21. Mäki-Arvela, P.; Hájek, J.; Salmi, T.; Murzin, D. Y., Chemoselective hydrogenation of carbonyl compounds over heterogeneous catalysts. *Applied Catalysis A: General* **2005,** *292*, 1-49.

22. Raab, C. G.; Lercher, J. A., Activity and selectivity of PtNi/TiO2 catalysts for hydrogenation of crotonaldehyde. *Catalysis letters* **1993,** *18* (1), 99-109.

23. Galvagno, S.; Donato, A.; Neri, G.; Pietropaolo, R.; Pietropaolo, D., Hydrogenation of cinnamaldehyde over platinum catalysts: influence of addition of metal chlorides. *Journal of molecular catalysis* **1989,** *49* (2), 223-232.

24. Waghray, A.; Blackmond, D. G., Infrared spectroscopic studies of the adsorption and reaction of 3-methyl-2-butenal over alkali-promoted ruthenium/silica catalysts. *The Journal of Physical Chemistry* **1993,** *97* (22), 6002-6006.

25. Galvagno, S.; Poltarzewski, Z.; Donato, A.; Neri, G.; Pietropaolo, R., Selective hydrogenation of α, β-unsaturated aldehydes to give unsaturated alcohols over platinum–germanium catalysts. *Journal of the Chemical Society, Chemical Communications* **1986,** (23), 1729-1731.

26. Marinelli, T.; Ponec, V., A Study on the selectivity in acrolein hydrogenation on platinum catalysts: a model for hydrogenation of α, β-unsaturated aldehydes. *Journal of Catalysis* **1995,** *156* (1), 51-59.

27. Passos, F. B.; Schmal, M.; Vannice, M., Effect of in and Sn on the adsorption behavior and hydrogenolysis activity of Pt/Al2O3Catalysts. *Journal of Catalysis* **1996,** *160* (1), 106-117.

28. Merlo, A. B.; Vetere, V.; Ramallo-López, J. M.; Requejo, F. G.; Casella, M. L., Liquid-phase furfural hydrogenation employing silica-supported PtSn and PtGe catalysts prepared using surface organometallic chemistry on metals techniques. *Reaction Kinetics, Mechanisms and Catalysis* **2011,** *104* (2), 467-482.

29. Poltarzewski, Z.; Galvagno, S.; Pietropaolo, R.; Staiti, P., Hydrogenation of α, β-unsaturated aldehydes over Pt Sn/Nylon. *Journal of Catalysis* **1986,** *102* (1), 190-198.

30. Coloma, F.; Llorca, J.; Homs, N.; de la Piscina, P. R.; Rodríguez-Reinoso, F.; Sepúlveda-Escribano, A., Crotonaldehyde hydrogenation over alumina-and silica-supported Pt–Sn catalysts of different composition. In situ DRIFT study. *Physical Chemistry Chemical Physics* **2000,** *2* (13), 3063-3069.

31. Taniya, K.; Jinno, H.; Kishida, M.; Ichihashi, Y.; Nishiyama, S., Preparation of Sn-modified silica-coated Pt catalysts: A new PtSn bimetallic model catalyst for selective hydrogenation of crotonaldehyde. *Journal of catalysis* **2012,** *288,* 84-91.

32. Concepción, P.; Pérez, Y.; Hernandez-Garrido, J.; Fajardo, M.; Calvino, J.; Corma, A., The promotional effect of Sn-beta zeolites on platinum for the selective hydrogenation of α, β-unsaturated aldehydes. *Physical Chemistry Chemical Physics* **2013,** *15* (29), 12048-12055.

33. Beccat, P.; Bertolini, J.; Gauthier, Y.; Massardier, J.; Ruiz, P., Crotonaldehyde and methylcrotonaldehyde hydrogenation over Pt (111) and Pt80Fe20 (111) single crystals. *Journal of Catalysis* **1990,** *126* (2), 451-456.

34. Stassi, J. P.; Zgolicz, P. D.; de Miguel, S. R.; Scelza, O. A., Formation of different promoted metallic phases in PtFe and PtSn catalysts supported on carbonaceous materials used for selective hydrogenation. *Journal of catalysis* **2013,** *306*, 11-29.

35. Richard, D.; Ockelford, J.; Giroir-Fendler, A.; Gallezot, P., Composition and catalytic properties in cinnamaldehyde hydrogenation of charcoal-supported, platinum catalysts modified by FeCl2 additives. *Catalysis letters* **1989,** *3* (1), 53-58.

36. Schroder, U.; Deverdier, L., Influence of oxygen and iron in the liquid-phase hydrogenation of α, β-unsaturated aldehydes. *Journal of Catalysis* **1993,** *142* (2), 490-498.

37. Guo, Z.; Zhou, C.; Shi, D.; Wang, Y.; Jia, X.; Chang, J.; Borgna, A.; Wang, C.; Yang, Y., Toward the decoration of Pt nanoparticles supported on carbon nanotubes with Fe oxides and its effect on the catalytic reaction. *Applied Catalysis A: General* **2012,** *435*, 131-140.

38. Mäki-Arvela, P.; Tiainen, L.-P.; Lindblad, M.; Demirkan, K.; Kumar, N.; Sjöholm, R.; Ollonqvist, T.; Väyrynen, J.; Salmi, T.; Murzin, D. Y., Liquid-phase hydrogenation of citral for production of citronellol: catalyst selection. *Applied Catalysis A: General* **2003,** *241* (1-2), 271-288.

39. Santori, G. F.; Casella, M. L.; Ferretti, O. A., Hydrogenation of carbonyl compounds using tin-modified platinum-based catalysts prepared via surface organometallic chemistry on metals (SOMC/M). *Journal of Molecular Catalysis A: Chemical* **2002,** *186* (1-2), 223-239.

40. Chandler, B. D.; Pignolet, L. H., DRIFTS studies of carbon monoxide coverage on highly dispersed bimetallic Pt-Cu and Pt-Au catalysts. *Catalysis today* **2001,** *65* (1), 39-50.

41. Candy, J.-P.; Didillon, B.; Smith, E. L.; Shay, T. B.; Basset, J.-M., Surface organometallic chemistry on metals: a novel and effective route to custom-designed bimetallic catalysts. *Journal of molecular catalysis* **1994,** *86* (1-3), 179-204.

42. Vértes, C.; Tálas, E.; Czakó-Nagy, I.; Ryczkowski, J.; Göbölös, S.; Vértes, A.; Margitfalvi, J., Mössbauer spectroscopy studies of Sn-Pt/Al2O3 catalysts prepared by controlled surface reactions. *Applied catalysis* **1991,** *68* (1), 149-159.

43. Liberková, K.; Touroude, R., Performance of Pt/SnO2 catalyst in the gas phase hydrogenation of crotonaldehyde. *Journal of Molecular Catalysis A: Chemical* **2002,** *180* (1-2), 221-230.

44. Reyes, P.; Aguirre, M. d. C.; Fierro, J.; Santori, G.; Ferretti, O., Hydrogenation of crotonaldehyde on Rh-Sn/SiO2 catalysts prepared by reaction of tetrabutyltin on prereduced Rh/SiO2 precursors. *Journal of Molecular Catalysis A: Chemical* **2002,** *184* (1-2), 431-441.

45. Margitfalvi, J.; Vankó, G.; Borbáth, I.; Tompos, A.; Vértes, A., Characterization of Sn–Pt/SiO2 catalysts used in selective hydrogenation of crotonaldehyde by mössbauer spectroscopy. *Journal of Catalysis* **2000,** *190* (2), 474-477.

46. Marchi, A. J.; Gordo, D. A.; Trasarti, A. F.; Apesteguía, C. R., Liquid phase hydrogenation of cinnamaldehyde on Cu-based catalysts. *Applied Catalysis A: General* **2003,** *249* (1), 53-67.

47. Dandekar, A.; Vannice, M., Determination of the dispersion and surface oxidation states of supported Cu catalysts. *Journal of Catalysis* **1998,** *178* (2), 621-639.

48. Sinfelt, J. H., *Bimetallic Catalysts: Discoveries, Concepts and Applications*. John Wiley and Sons: New York, 1983; p 164.

49. Ferrando, R.; Jellinek, J.; Johnston, R. L., Nanoalloys: From Theory to Applications of Alloy Clusters and Nanoparticles. *Chem. Rev.* **2008,** *108* (3), 845-910.

50. Yu, W.; Porosoff, M. D.; Chen, J. G., Review of Pt-Based Bimetallic Catalysis: From Model Surfaces to Supported Catalysts. *Chem. Rev.* **2012,** *112* (11), 5780-5817.

51. Rodriguez, J. A., Physical and Chemical Properties of Bimetallic Surfaces. *Surf. Sci. Rep.* **1996,** *24* (7-8), 223-287.

52. Wang, Y.; Balbuena, P. B., Design of Oxygen Reduction Bimetallic Catalysts: Ab-Initio-Derived Thermodynamic Guidelines. *J. Phys. Chem. B* **2005,** *109* (40), 18902-18906.

53. Medford, A. J.; Vojvodic, A.; Hummelshøj, J. S.; Voss, J.; Abild-Pedersen, F.; Studt, F.; Bligaard, T.; Nilsson, A.; Nørskov, J. K., From the Sabatier principle to a predictive theory of transition-metal heterogeneous catalysis. *J. Catal.* **2015,** *328*, 36-42.

54. Greiner, M. T.; Jones, T. E.; Beeg, S.; Zwiener, L.; Scherzer, M.; Girgsdies, F.; Piccinin, S.; Armbrüster, M.; Knop-Gericke, A.; Schlögl, R., Free-atom-like d states in single-atom alloy catalysts. *Nat. Chem.* **2018,** *10* (10), 1008-1015.

55. Ponec, V., Alloy catalysts: the concepts. *Appl. Catal. A* **2001,** *222* (1), 31-45.

56. Liu, P.; Nørskov, J. K., Ligand and ensemble effects in adsorption on alloy surfaces. *Phys. Chem. Chem. Phys.* **2001,** *3* (17), 3814-3818.

57. Gao, F.; Goodman, D. W., Pd-Au bimetallic catalysts: understanding alloy effects from planar models and (supported) nanoparticles. *Chem. Soc. Rev.* **2012,** *41* (24), 8009-8020.

58. Bent, B. E., Mimicking aspects of heterogeneous catalysis: generating, isolating, and reacting proposed surface intermediates on single crystals in vacuum. *Chemical reviews* **1996,** *96* (4), 1361-1390.

59. Pallassana, V.; Neurock, M., Electronic factors governing ethylene hydrogenation and dehydrogenation activity of pseudomorphic PdML/Re (0001), PdML/Ru (0001), Pd (111), and PdML/Au (111) surfaces. *Journal of Catalysis* **2000,** *191* (2), 301-317.

60. Liu, Z.-P.; Hu, P., General trends in CO dissociation on transition metal surfaces. *The Journal of Chemical Physics* **2001,** *114* (19), 8244-8247.

61. Abild-Pedersen, F.; Greeley, J.; Studt, F.; Rossmeisl, J.; Munter, T. R.; Moses, P. G.; Skúlason, E.; Bligaard, T.; Nørskov, J. K., Scaling Properties of Adsorption Energies for Hydrogen-Containing Molecules on Transition-Metal Surfaces. *Physical Review Letters* **2007,** *99* (1), 016105.

62. Darby, M. T.; Stamatakis, M.; Michaelides, A.; Sykes, E. C. H., Lonely Atoms with Special Gifts: Breaking Linear Scaling Relationships in Heterogeneous Catalysis with Single-Atom Alloys. *The Journal of Physical Chemistry Letters* **2018,** *9* (18), 5636-5646.

63. Hannagan, R. T.; Giannakakis, G.; Flytzani-Stephanopoulos, M.; Sykes, E. C. H., Single-Atom Alloy Catalysis. *Chemical Reviews* **2020,** *120* (21), 12044-12088.

64. Lucci, F. R.; Liu, J.; Marcinkowski, M. D.; Yang, M.; Allard, L. F.; Flytzani-Stephanopoulos, M.; Sykes, E. C. H., Selective hydrogenation of 1, 3-butadiene on platinum–copper alloys at the single-atom limit. *Nature communications* **2015,** *6* (1), 8550.

65. Liu, J.; Shan, J.; Lucci, F. R.; Cao, S.; Sykes, E. C. H.; Flytzani-Stephanopoulos, M., Palladium–gold single atom alloy catalysts for liquid phase selective hydrogenation of 1-hexyne. *Catalysis Science & Technology* **2017,** *7* (19), 4276-4284.

66. Marcinkowski, M. D.; Darby, M. T.; Liu, J.; Wimble, J. M.; Lucci, F. R.; Lee, S.; Michaelides, A.; Flytzani-Stephanopoulos, M.; Stamatakis, M.; Sykes, E. C. H., Pt/Cu single-atom alloys as coke-resistant catalysts for efficient C–H activation. *Nature chemistry* **2018,** *10* (3), 325-332.

Chapter 2 Instrumental and Catalyst Characterization

2.1 Catalysts synthesis

2.1.1 Material and Chemicals

10 of Cu-Pt bimetallic catalysts, denoted $CuPt_x$/SBA-15, copper nitrate ($Cu(NO_3)_2·3H_2O$, Sigma-Aldrich, 98% purity) and chloroplatinic acid ($H_2PtCl_6·6H_2O$, Sigma-Aldrich, ≥37.50% Pt basis) were used as metal precursors. Commercial SBA-15 (ACS Material) was used as supporting material.

For the synthesis of core-shell catalysts, Copper (II) nitrate hemi(pentahydrate) ($Cu(NO_3)_2·2.5H_2O$, Sigma-Aldrich, 98% purity) and Chloroplatinic acid hexahydrate ($H_2PtCl_6·6H_2O$, Sigma-Aldrich, ≥37.50% Pt basis) are used as metal sources. Commercial SBA-15 (ACS Material) was used as supporting material. Poly(vinylpyrrolidone) (PVP, MW = 10,000, Sigma-Aldrich) was used as a stabilizing agent for colloidal nanoparticles. All materials are used as received unless otherwise noted. Ethylene Glycol (Certified, Fisher Chemical) was used as a reducing agent for the synthesis of Pt nanoparticles. Ethanol (200 Proof, Fisher Chemical) was used to wash the catalysts. Tert-Butylamine (98%, Sigma-Aldrich) was used to remove the capping agent. L-ascorbic acid (99%, Sigma-Aldrich) was used to reduce Cu cation to metallic Cu nanoparticles.

Carbon monoxide used in in situ infrared spectroscopy was purchased from Matheson. Hydrogen and most other gases were purchased from Airgas.

2.1.2 Catalyst Synthesis

$CuPt_x$/SBA-15

In this work, $CuPt_x$/SBA-15 are prepared by a previous member of our group (Dr. Yueqiang Cao) via incipient wetness impregnation method[1]. A total of 10 $CuPt_x$/SBA-15 catalysts were prepared by using an incipient wetness impregnation method, with x, which represent the molar fraction of Pt added to the constant 5 wt% Cu load, varying from 0 (pure Cu) to ∞ (pure Pt). In detail, certain amounts of copper nitrate and chloroplatinic acid were mixed with deionized water, followed by impregnating it with approximately 2 grams of SBA-15. In all ten catalysts, the loading of Cu is about ~5wt %. In addition, the ratio of Cu/Pt was altered by changing the amount of chloroplatinic acid added in the liquid mixture before impregnation. After the impregnation step, our sample was kept at room temperature for 1 day, namely 24 hours, followed by drying it at 350 K for 24 hours again and then grounding it into powder. At the end, $CuPt_x$/SBA-15 are reduced under H_2 at 625 K prior to use.

Core-shell Pt@Cu catalysts

Detailed synthesis procedure is mentioned in the following chapter. To start with, Pt/SBA-15 was prepared by reducing Pt on SBA-15, then the catalyst was washed with deionized water/ethanol mixture. After that, TBA was used to further remove all the capping agent left on the surface of our catalyst. For the synthesis of core-shell Pt@$Cu_{5.25}$/SBA-15, Cu atoms were deposited onto Pt/SBA-15 by reducing Cu with L-ascorbic acid.

2.2 *In Situ* Infrared Absorption Spectroscopy (IR)

One of the heavily used techniques in this work is the *in situ* infrared absorption spectroscopy (IR) study. It was carried out in a homemade NaCl-terminated quartz cell capable of sustaining pressure of up to approximately 2 bar and of cooling or heating to temperatures within the range from 125 to approximately 700 K, and a Bruker Tensor 27 FTIR spectrometer equipped with a deuterated triglycine sulfate (DTGS) detector.[2-3], All spectra were acquired with a resolution of 2 cm^{-1}, and correspond to an average of 16 scans.

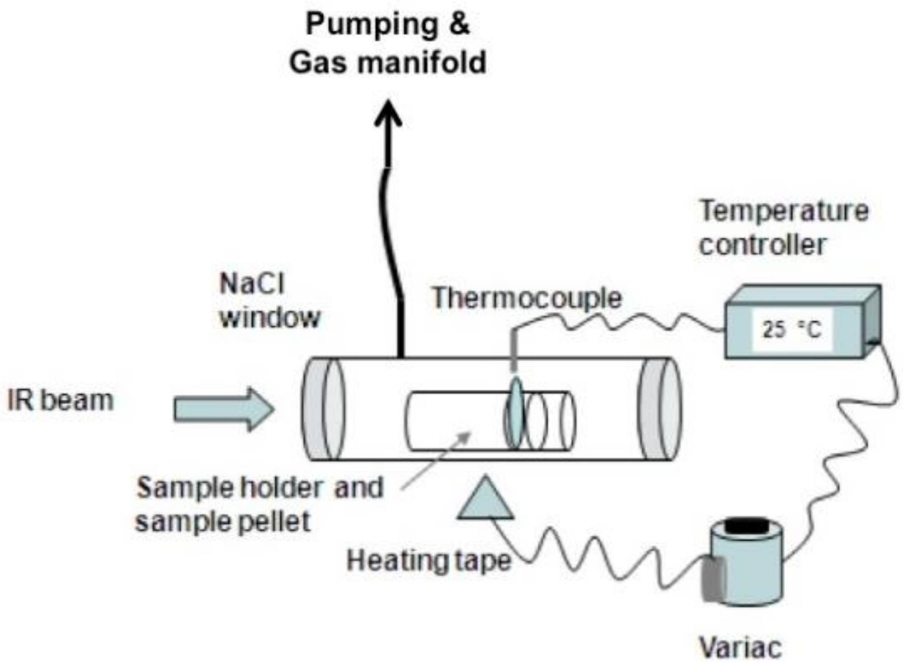

Figure 2-1. Typical experimental setup

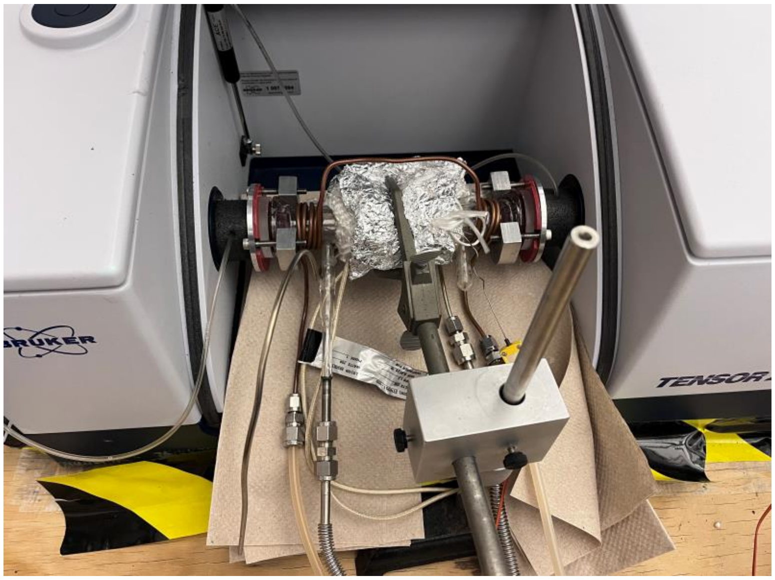

Figure 2-2. Picture of Transmission cell covered with heating type used in this dissertation.

Typically, testing IR spectra can be divided into several steps: sample preparation and loading, alignment, collecting background spectra, and taking sample spectrum. Example steps are shown below from a to g.

a) Sample Preparation, Mounting, and Processing

i. Sample Preparation and Loading

1. Powder catalyst (10-15 mg) is pressed into a self-support disk (13 mm in diameter) by using a manual press kit.
2. The catalyst pellet is mounted on a sample holder held in the center of the IR cell.
3. Both ends of the IR cell are sealed with NaCl windows.
4. The IR cell is connected to a gas manifold.
5. The IR cell is pumped to reach a background pressure to ~10^{-2} Torr range.

ii. Sample Heating and cooling.

Heating the IR cell is performed by using a Variac and a temperature controller (homemade). Usually, it can be heated above 350 ℃ by setting the Variac at 100%. For lower temperatures, a combination of electrical heating (Variac at 50%) and N_2 cooling can be used to alter the temperature. Stepped heating is accomplished by adjusting the Variac settings to alter the power ratio. From RT to 345 K, setting the Variac at 30 %. From 345 K to 395 K, setting the Variac at 35 %. From 395 K to 445 K, setting the Variac at 40 %. From 445 K to 495 K, setting the Variac at 45 %.

iii. Sample Pretreatment with H_2

1. Anneal to 350 ℃ slowly.
2. The pellet is degassed and dried in vacuum while ramping.
3. Keep the catalyst at 350 ℃ for 3~4 hours under 200~500 Torr of H_2.
4. Pump H_2 gas for 30 min.
5. Cool down to room temperature.

b) Alignment

1. Select "Measure", "Measurement" and "Check Signal" in the Measurement window.
2. If everything is OK, an interferogram will be displayed on the screen.
3. Check the amplitude; select ADC Count to see a numerical value.
4. Slowly move the IR cell within its position in the sample compartment until a maximum value is obtained.
5. Insert polyethylene foam tubes at both sides of the IR cell, between the NaCl windows of the cell and the windows of the FTIR spectrometer to purge the IR beam path (Both ends of the cell should touch the windows on the wall of the sample compartment).
6. Purge those tubes with dry air or N_2 gas.

c) Collecting Background Spectra with sample under vacuum (ex-situ)

For temperature-dependent sequences, reference spectra can be obtained during the cooling after pretreatment. These spectra are used as background spectra at the corresponding temperatures.

1. Cool down the sample to the desired or lowest temperature.
2. When the sample reaches the desired temperature, take a background spectrum.
3. Go to “Background” and Click “Save Background” to save the spectrum. The Filename (####.0) is saved automatically on the hard drive and displayed on the left (Window List) of the screen.
4. The file can be saved as other formats on the hard drive. Select "Save File As", then check the file name and path to be saved.
5. In temperature-dependent sequences, take and save background spectra during the cooling of the catalyst with about a proper interval (10 to 50 ℃).

d) Sample Spectrum (ex-situ, sample results taken without gas inside the transmission cell)

For the ex-situ experiment, once the temperature reaches the lowest temperature, introduce 20 ~ 30 Torr of the CO into the IR cell, then keep it for 5 min.

1. Pump the gas out from the IR cell until it reaches ~10^{-2} Torr.
2. Start taking the IR data with an interval of 10 K.
3. Remove the liquid N_2 reservoir until it’s reaching room temperature.
4. Start heating once the temperature reaches room temperature.
5. Take data until 473 K.

e) Reference Spectrum (in-situ, without sample pellet under different pressure of gases)

1. Empty the transmission cell by removing the previously used sample pellet.
2. Pump the cell to ~10^{-2} Torr.
3. Introduce x Torr of CO into the cell (x = 1, 2, 5, 10, 20, 50, 100, 200 Torr).
4. Start taking IR data followed by heating the transmission cell from room temperature to 495 K, with an interval of 50 K.
5. Pump the cell once all data is taken.

f) Sample Spectrum (in-situ, with sample pellet under different pressures of gases)

For the in-situ experiment, once the sample pellet is put inside the transmission cell, pump the cell to vacuum to ~10^{-2} Torr under room temperature.

1. Introduce x Torr of CO (x = 1, 2, 5, 10, 20, 50, 100, 200 Torr) into the IR cell.
2. Take data followed by heating the transmission cell from RT to 495 K, with an interval of 50 K (RT, 345, 395, 445, 495 K).
3. Cool the IR cell down to room temperature and take data at 495, 445, 395, 345, RT.
4. Pump the cell and stop the experiment.
5. Subtract the reference spectra from Reference Spectrum.

g) Taking Sample Spectrum for three cycles (in-situ, with sample pellet under different pressures of gases)

For the in-situ experiment, once the sample pellet is put inside the transmission cell, pump the cell to vacuum to ~10^{-2} Torr under room temperature.

1. Introduce x Torr of CO (x = 1, 2, 5, 10, 20, 50, 100, 200 Torr) into the IR cell.
2. Take data followed by heating the transmission cell from RT to 495 K, with an interval of 50 K (RT, 345, 395, 445, 495 K).
3. Cool the IR cell down to room temperature and take data at 495, 445, 395, 345, RT.
4. Pump the cell for 30 minutes or until the pressure is lowered to ~10^{-2} Torr.
5. Introduce another x Torr of CO.
6. Retake data during the temperature cycling process, both while heating from room temperature (RT) to 495 K and during cooling from 495 K back to RT.
7. Repeat step 4-6.
8. Pump the cell and stop the experiment.
9. Subtract the Reference Spectrum from the obtained data.

2.3 Other Characterizations

Nanoparticle size distribution

The metal NPs size distributions were estimated from electron microscopy images taken using a scanning transmission electron microscopy (STEM) FEI Titan Themis 300 instrument equipped with an X-ray spectrometer for energy dispersion spectroscopy

(EDS) imaging. The images were acquired by Dr. Ilkeun Lee at the UCR Central Facility for Advanced Microscopy and Microanalysis.

Catalyst composition

The metal loadings were quantified by inductively coupled plasma atomic emission spectrometry (ICP-AES), using a PerkinElmer Optima 7300DV ICP-OES apparatus that combines an SCD detector and an echelle optical system which enables the unit to measure all wavelengths simultaneously-in the ultraviolet wavelength range from 165 to 403 nm and in the visible wavelength range from 404 to 782 nm. The results were obtained by David H. Lyons at the Department of Environmental Sciences.

Typically, about 10 mg of sample catalyst was dissolved in 20 ml of aqua regia, namely, a mixture of 15 ml of HCl (concentrated, ~37% solution in water) and 5 ml of HNO_3 (Nitric acid, 65-75% solution in water). The entirety of the mixture was maintained in aqua regia at a temperature of 370 K for a duration of one hour, followed by an elevation to 395 K for an additional hour. Subsequently, the resultant mixture underwent filtration and was employed to formulate a 100 mL solution, intended for subsequent analysis.

X-ray Photoelectron Spectroscopy (XPS)

The *ex-situ* XPS data were acquired by using a Kratos analytical AXIS instrument equipped with a 165 mm mean radius semi-hemispherical electron energy analyzer and a monochromatized Al anode X-ray source. The spectra were taken by Dr. Ilkeun Lee at the UCR XPS Facility. The *ex-situ* XPS data in Figure 4-1 were acquired by using a Kratos analytical AXIS instrument equipped with a 165 mm mean radius semi-hemispherical electron energy analyzer and a monochromatized Al anode X-ray source.

X-ray Absorption Spectroscopy (XAS)

The *in situ* X-ray absorption spectroscopy (XAS) experiments were carried out at three different synchrotron facilities. The data for the $CuPt_{0.05}$/SBA-15 catalyst shown in Figure 4-5 was acquired at the ISS (Inner-Shell Spectroscopy) beamline of the National Synchrotron Light Source II (NSLS-II) facility of Brookhaven National Laboratory, with the assistance of Dr. YuanYuan Li and Prof. Anatoly Frenkel. For the in-situ measurements, the sample powders were loaded on a quartz tubing (O.D. = 2.4 mm, I.D. = 2 mm) and mounted in a Clausen cell.[4] The Pt L_3 XAS data were collected in fluorescence mode and the Cu K edge XAS data were collected in transmission mode.

The H_2-reduction results in Figure 4-6 and Figure 4-7, from studies with the $CuPt_{0.005}$/SBA-15 sample, were obtained by Debora Motta Meira and Mahalingam Balasubramanian at the Advanced Photon Source (APS) at Argonne National Laboratory. A Si (111) double-crystal monochromator and a toroidal focusing mirror were employed. The first harmonic of the undulator was used along with full scanning of the undulator. Harmonic rejection was facilitated by detuning 30% of the incident beam intensity at hν = 1000 eV above the edge of interest. A capillary furnace, composed of resistively-heated quartz tubes (O.D. = 1.5 mm, I.D. = 1.3 mm), was used. Each sample was treated with heat and gas, and Cu K-edge data were collected *in situ* in the presence of the gases and while heating the sample to the indicated temperatures, in fluorescence mode using a Vortex 4-element detector.

The in-situ oxidation reaction under H_2 results, from studies with $CuPt_{0.05}$/SBA-15 sample, were acquired with the assistance of Debora Motta Meira at the Advanced Photon Source (APS) at Argonne National Laboratory. About 30 mg of $CuPt_{0.05}$/SBA-15 was pressed into a pellet and tested.

Finally, the *in-situ* spectra for the $CuPt_{0.005}$/SBA-15 solid during the hydrogenation of crotonaldehyde were recorded at the Stanford Synchrotron Radiation Light source (SSRL) of the Stanford Linear Accelerator Center with the help of Jiyun Hong, Adam S. Hoffman, and Simon R. Bare. The experiment was conducted at beamline 9–3, which is a 16-pole, 2-tesla wiggler beamline with a vertically collimating mirror for harmonic rejection and a cylindrically bent mirror for focusing. The liquid-nitrogen cooled, double-crystal Si (220) monochromator was used at crystal orientation of phi = 0˚. Finely powdered and sieved ~4 mg of $CuPt_{0.005}$/ SBA15 sample was packed between Quartz wool inside a Quartz capillary tube (I.D. = 0.96 mm, O.D. = 1.0 mm) to make a 10-cm long bed. Both ends of the capillary tube were carefully glued to Swagelok connectors, which were used to connect to a flow-through reactor.[5] The reactor was mounted on the sample stage at a 45° angle relative to the incident X-ray beam. N_2-filled ion chambers were used to measure the incident X-ray intensity and the transmission signal from the sample. XAS data were acquired in situ while flowing either pure H_2 of a mixture of H_2 with crotonaldehyde at a total flow of 20 mL/min; the crotonaldehyde was added to the gas stream using a bubbler (saturator), kept at 288 K; the estimated crotonaldehyde partial pressure obtained this way was estimated to be 0.04 bar. A mass-spectrometer (Hiden QGA) was used throughout the experiments to follow the composition of the exhaust gas during catalysis: 100% hydrogenation conversion was attained at 375 K.

The Cu K-edge EXAFS data were analyzed by using a model that included Cu–O and Cu–Cu paths. For the $PtCu_{0.05}$/SBA-15 sample, the fitting k range was 2-11.5Å-1 and the r range 1-2.8 Å, and for the $PtCu_{0.005}$/SBA-15 sample they were 2-10.5 Å-1 and 1-2.8 Å, respectively. An amplitude reduction factor (0.86 ± 0.03) was obtained by fitting the Cu foil data.

2.4 Reference

1. Cao, Y.; Chen, B.; Guerrero-Sánchez, J.; Lee, I.; Zhou, X.; Takeuchi, N.; Zaera, F., Controlling Selectivity in Unsaturated Aldehyde Hydrogenation Using Single-Site Alloy Catalysts. *ACS Catalysis* **2019,** *9* (10), 9150-9157.

2. Zhu, Y.; Zaera, F., Selectivity in the catalytic hydrogenation of cinnamaldehyde promoted by Pt/SiO2 as a function of metal nanoparticle size. *Catalysis Science & Technology* **2014,** *4* (4), 955-962.

3. Cao, Y.; Chen, B.; Guerrero-Sánchez, J.; Lee, I.; Zhou, X.; Takeuchi, N.; Zaera, F., Controlling Selectivity in Unsaturated Aldehyde Hydrogenation Using Single-Site Alloy Catalysts. *ACS Catal.* **2019,** *9*, 9150-9157.

4. Chupas, P. J.; Chapman, K. W.; Kurtz, C.; Hanson, J. C.; Lee, P. L.; Grey, C. P., A versatile sample-environment cell for non-ambient X-ray scattering experiments. *J. Appl. Crystallogr.* **2008,** *41* (4), 822-824.

5. Hoffman, A. S.; Singh, J. A.; Bent, S. F.; Bare, S. R., In situ observation of phase changes of a silica-supported cobalt catalyst for the Fischer-Tropsch process by the development of a synchrotron-compatible in situ/operando powder X-ray diffraction cell. *J. Synchrotron Radiat.* **2018,** *25* (6), 1673-1682.

Chapter 3 In Situ Identification of Surface Sites in Cu-Pt Bimetallic Catalysts: Gas-Induced Metal Segregation

In this chapter we discuss the results from our studies of Cu-Pt bimetallic catalysts using in-situ infrared (IR) and X-ray (XAS) absorption spectroscopies to probe the effect of gases on the surface composition of them. It has been found that Pt atoms are diffusing within the Cu-Pt nanoparticles both in vacuum and under gaseous atmosphere. Vacuum IR spectra of CO adsorbed on $CuPt_x$/SBA-15 catalyst ($x = 0$ to ∞) at 125 K showed no bonding on Pt, no matter of Pt content. However, reservable Pt segregation to the surface of nanoparticles was observed for high-Pt-content ($x \geq 0.2$) catalysts upon heating to 225 K. In situ IR spectra in CO atmospheres also emphasize the reversible segregation of Pt to the surface and its diffusion back into the bulk when cycling the temperature from 295 K to 495 K and back, most evidently for diluted single-atom alloy catalysts ($x \leq 0.01$). Similar behavior was possibly seen under the Hydrogen atmosphere, in which a small amount of CO was used as a probe molecule. In situ X-ray absorption near-edge structure (XANES) data taken for $CuPt_{0.2}$/SBA-15 under both CO and He pointed to the metallic nature of the Pt atoms irrespective of gas or temperature, but analysis of the extended X-ray absorption fine structure (EXAFS) identified a change in coordination environment around the Pt atoms, from a (Pt-Cu):(Pt-Pt) coordination number ratio of 6:6 at or below 445 K to 8:4 at 495 K. Our main conclusion is that Cu-Pt bimetallic catalysts are dynamic, with the composition of their surfaces being dependent on temperature, especially in gaseous atmosphere.

3.1 Introduction

A new version of alloying in catalysis has garnered significant interest in recent years where a majority metal is mixed with a small amounts of a second component to create so-called single-atom alloys (SAAs).[1-4] The distinctiveness of single-atom alloys (SAAs) compared to conventional bimetallic catalysts is that, in SAA, the minority component is believed to be present on the surface of the nanoparticles (NPs) in isolated form, far from other atoms of the same metal. The premise guiding the design of SAA catalysts is that the single-atom sites add specific functionality lacking in the majority component, which otherwise is assumed to selectively promote process of interest.[4-5] In the case of hydrogenation catalysis, for example, the addition of small amounts of an active metal such as Pt or Pd may help with the activation of molecular hydrogen, something for which coinage metals such as Cu or Au exhibits insufficient efficacy;[6-8] this way, it may be possible to exploit the presumed selectivity of those coinage metals during the promotion of the hydrogenation steps.[3-4, 9-12]

Empirically, it has become clear that SAA catalysts can in many instances improve the selectivity of hydrogenation reactions.[13-18] An understanding of how that occurs, however, is still being developed. A significant amount of elegant surface-science work using model metal surfaces such as single crystals and controlled ultra-high vacuum

(UHV) environments has been performed[14, 19-21] and complemented with quantum mechanics calculations[22-24] to support a proposed mechanism by which H_2 molecules are dissociated on individual Pt or Pd atoms present on the surface, after which the resulting adsorbed H atoms spill over to the Cu or Au surfaces where the organic molecules are hydrogenated. On the other hand, most recent evidence However, more recent evidence from our group and from others has suggested that the performance of real SAA catalysts, which typically consist of SAA NPs dispersed on a high-surface-area oxide support, may be affected by additional factors, in particular the ease with which specific metals segregate to the surface and/or diffuse into the metal bulk upon exposure to various chemical environments.[17, 25-30].

The fact that one of the metals in alloys may segregate to the surface or diffuse into the bulk depending on the conditions and chemical environments is well known; a beautiful example was provided a few years ago by the Salmeron group, who showed using near-ambient-pressure X-ray photoelectron spectroscopy (NAP-XPS) that Rh-Pd core-shell NPs undergo reversible changes in composition and chemical state in response to oxidizing or reducing conditions: Rh segregates to the surface in a pure NO environment, whereas a more mixed-metal layer with significant amounts of Pd on the surface develops during NO + CO conversions.[31] In a case involving hydrogenation catalysis, for the selective conversion of cinnamaldehyde, the Rh-Au bimetallic catalyst was shown to undergo segregation into Janus NPs during catalysis.[32] If the active metal in SAAs were to diffuse deep into the bulk, its activity may be hindered. For instance, the group of

Crooks and coworkers proved that coating Pt NPs with a layer of Cu, to form Pt@Cu core-shell structures, leads to the inhibition of the electrochemical hydrogen evolution reaction (HER).[33] It is therefore imperative to characterize the composition of the surface in bimetallic catalysts *in situ* to determine the true nature of the active sites. In this work we do that for the case of Cu-Pt bimetallic catalysts by combining the use of *in situ* infrared (IR) and X-ray (XAS) absorption spectroscopies during exposures to atmospheric pressures of different gases, both reactive (CO, H_2) and inert (He). Our results indicate that, indeed, selective metal segregation does occur as a function of temperature. The details are provided below.

3.2 Results and Discussion

A total of 10 $CuPt_x$/SBA-15 catalysts were prepared by Dr. Yueqiang Cao using an incipient wetness impregnation method, using copper nitrate ($Cu(NO_3)_2 \cdot 3H_2O$, Sigma-Aldrich, 98% purity) and chloroplatinic acid ($H_2PtCl_6 \cdot 6H_2O$, Sigma-Aldrich, ≥37.50% Pt basis), as reported previously.[17-18] In our nomenclature, x represent the molar fraction of Pt added to a constant 5 wt% Cu load, and was varied from 0 (pure Cu) to ∞ (pure Pt). The physical characterization and pretreatment details of these catalysts have been provided before.[17-18]

Early indication that exposure of $CuPt_x$/SBA-15 catalysts to different gas environments may lead to metal segregation was provided by *ex situ* IR characterization experiments using carbon monoxide as a probe.[17] Figure 3-1 displays the IR spectra obtained in the C–

O stretching region for all 10 catalysts after saturation with CO at 125 K. The data were acquired under vacuum, after pumping of the CO used for dosing, while the IR cell was slowly heated; the four panels provide results for four different temperatures (125, 225, 325, and 425 K). It is seen in Figure 3-1 that the main peaks for CO adsorbed on all of the $CuPt_x$/SBA-15 SAA catalysts ($x = 0.001$ to 0.75) at low temperatures are at frequencies in the 2100 - 2135 cm^{-1} (main feature) and 2157 - 2170 cm^{-1} (shoulder) ranges, blue-shifted as the Pt content in the catalysts is increased. These values are close to those seen with the pure Cu/SBA-15 catalyst, at ~2124 and ~2160 cm^{-1} (Figure 3-1, left panel, top trace), and far from the much larger feature seen with the pure Pt/SBA-15 catalyst (bottom trace, peak at 2097 cm^{-1}). In fact, no signal that can be ascribed to CO adsorption on Pt atoms was seen in any of the alloy catalysts, with the possible exception of the broad feature seen around 2070 cm^{-1} with the $CuPt_{0.75}$/SBA-15 sample. It was concluded that no Pt atoms are present on the surfaces of any of the $CuPt_x$/SBA-15 ($x \leq 0.5$) within the detectability limit of the IR technique. In terms of the oxidation state of the Cu surface, we have, on the basis of the extensive studies available in the literature,[34-39] assigned the main 2124 cm^{-1} peak and the 2160 cm^{-1} shoulder to adsorption on metallic and oxidized Cu, respectively;[39] it would appear that the catalysts is not yet fully reduced at the start of these experiments (it does become fully reduced upon heating in the presence of CO, see below).

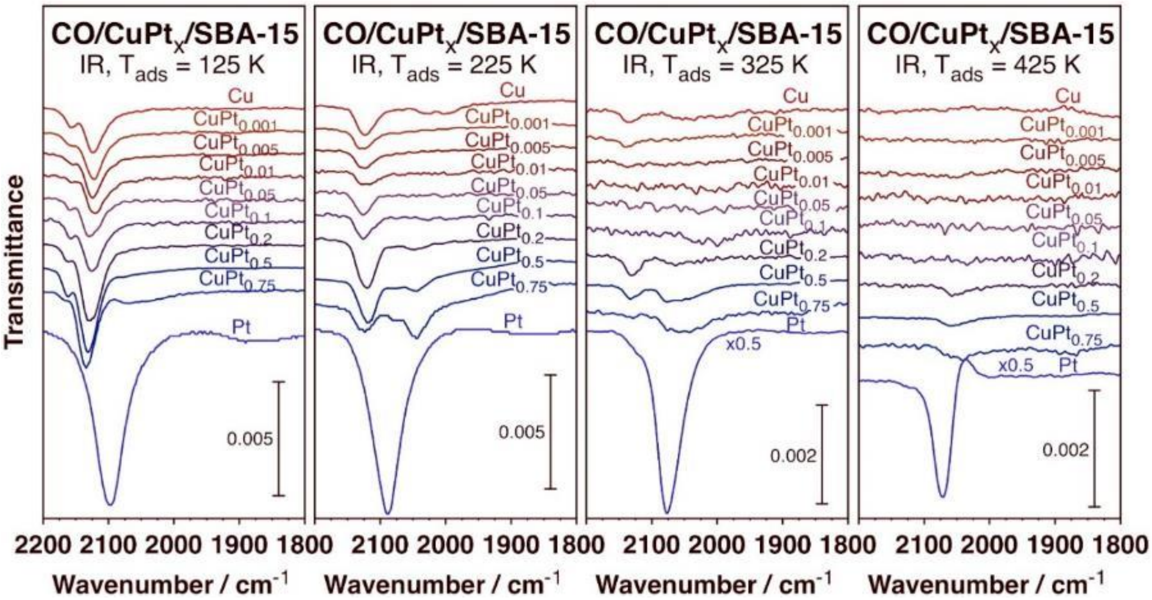

Figure 3-1. IR spectra for CO adsorbed on 10 different CuPt$_x$/SBA-15 catalysts (x = 0 to ∞) as a function of temperature: data for four values of T (125, 225, 325, and 425 K) are provided, each in a separate panel.

Heating to 225 K leads to some noticeable changes (Figure 3-1, 2nd-from-left panel). For one, the high frequency peak, associated with adsorption on oxidized Cu, is no longer evident in the spectra. It could be argued that CO bonding to those sites is weak and that, therefore, molecular desorption takes place at low temperatures, below 225 K. Alternatively, that adsorbed CO may react with the surface oxygen atoms and form CO_2, thus reducing the surface; the fact that the IR signal for gas-phase CO_2 increases upon heating of these samples (not shown) lead us to favor this second explanation. In any case, some CO desorption from metallic CO also occurs by 225 K, since the intensity of the main peak from all Cu/SBA-15 and CuPt$_x$/SBA-15 catalysts decrease. Particularly noteworthy is the evolution of a new peak in the low-frequency range for the samples with high ($x \geq 0.2$) Pt loads: that feature is weak and detected at 2050 cm^{-1} in $CuPt_{0.2}$/SBA-15 but it grows and red-shifts with increasing Pt fraction in the bimetallic NPs, to 2045 cm^{-1} in $CuPt_{0.5}$/SBA-15 and to 2044 cm^{-1} in $CuPt_{0.75}$/SBA-15. This signal is most likely associated with CO bonded to Pt atoms, which must therefore segregate to the surface. Given that the observed frequencies are below the values reported for CO adsorption on either pure Pt surfaces (even at low coverages),[40-42] or supported Pt catalysts,[43] we conclude that the Pt atoms in our bimetallic catalysts may be atomically dispersed within the Cu matrix. Similar frequencies have recently been reported for $CuPt_{0.39}/Al_2O_3$[44] and $AgPt_x/Al_2O_3$[45] SAA catalysts.

The third panel of Figure 3-1 shows the IR spectra recorded after heating to 325 K. By this temperature, most of the CO adsorbed on Cu is gone (notice the change of scale between the first two and the last two panels in Figure 3-1); the binding energy on pure Cu/SBA-15 is on the order of $\Delta H_{ads} = -82$ kJ/mol, and desorption in that case peaks at 245 K.[39] A small amount of CO on Cu is still detectable in some of the $CuPt_x$/SBA-15 samples, and the peak for CO adsorption on Pt sites in the high-content bimetallic catalysts broadens and blue-shifts, possibly because the molecules no longer interact with other CO molecules bonded to adjacent Cu sites. Finally, by 425 K (Figure 3-1, right panel), only small peaks for CO bonded to Pt are seen, and only for the high-Pt-content cases (at 2058 cm^{-1} with $CuPt_{0.1}$/SBA-15 and $CuPt_{0.2}$/SBA-15, and at 2042 cm^{-1} with $CuPt_{0.75}$/SBA-15). It should be noted that the CO seen in these high-Pt-content catalysts, although persistent to higher temperatures than the CO adsorbed on Cu, still desorbs at temperatures below those seen on pure Pt/SBA-15; the Pt–CO binding is clearly stronger than that of Cu–CO, but not as strong as on non-alloyed Pt surfaces.

In the end, the data in Figure 3-1 evidence the ability of CO to draw the Pt atoms in $CuPt_x$/SBA-15 catalysts from the bulk to the surface as those are heated. Additional experiments were performed to test the reversibility of this behavior. Figure 3-2 shows the IR data collected with the $CuPt_{0.5}$/SBA-15 (top) and $CuPt_{0.75}$/SBA-15 (bottom) catalysts as they were saturated with CO and heated under vacuum three times in a row. The left panels show the results in the form of 3D "heat" plots: the x axis represents the frequency range and the y axis temperature, and the peak intensities are color-coded from low (blue) to high (red, with yellow for intermediate values); on the right side of Figure 3-2, representative IR traces are provided for low (125 K) and high (225 K) temperatures for the three cycles. The spectra for the first cycle mimic those seen in Figure 3-1, and demonstrate that, upon heating to 225 K or above, some CO adsorbed on Cu desorbs (all of the CO on the oxide sites plus approximately half of those on metallic Cu) and new Pt–CO sites develop, the consequence of Pt segregation to the surface. The data from the second cycle looks similar to that from the first: upon cooling down the catalysts and saturating them again with CO the peaks for CO bonded to CO reappear and the signals for adsorption on Pt go away, but heating to 225 K again leads to the desorption of CO from Cu–CO sites and to the re-segregation of Pt to the surface. The results recorded during the third cycle are somewhat different, pointing to a possible irreversible change in the Cu-Pt bimetallic NPs, but the general trends are still the same, namely, the dominance of CO adsorption on Cu is restored at low temperatures but gives way to CO bonding to segregated Pt after heating the samples up. Also to notice here is the observation that the Pt–CO still desorbs by 300 K, a temperature clearly higher than that for Cu–CO but much lower than when CO desorbs from pure Pt surfaces (≥ 350 K).[46-48]

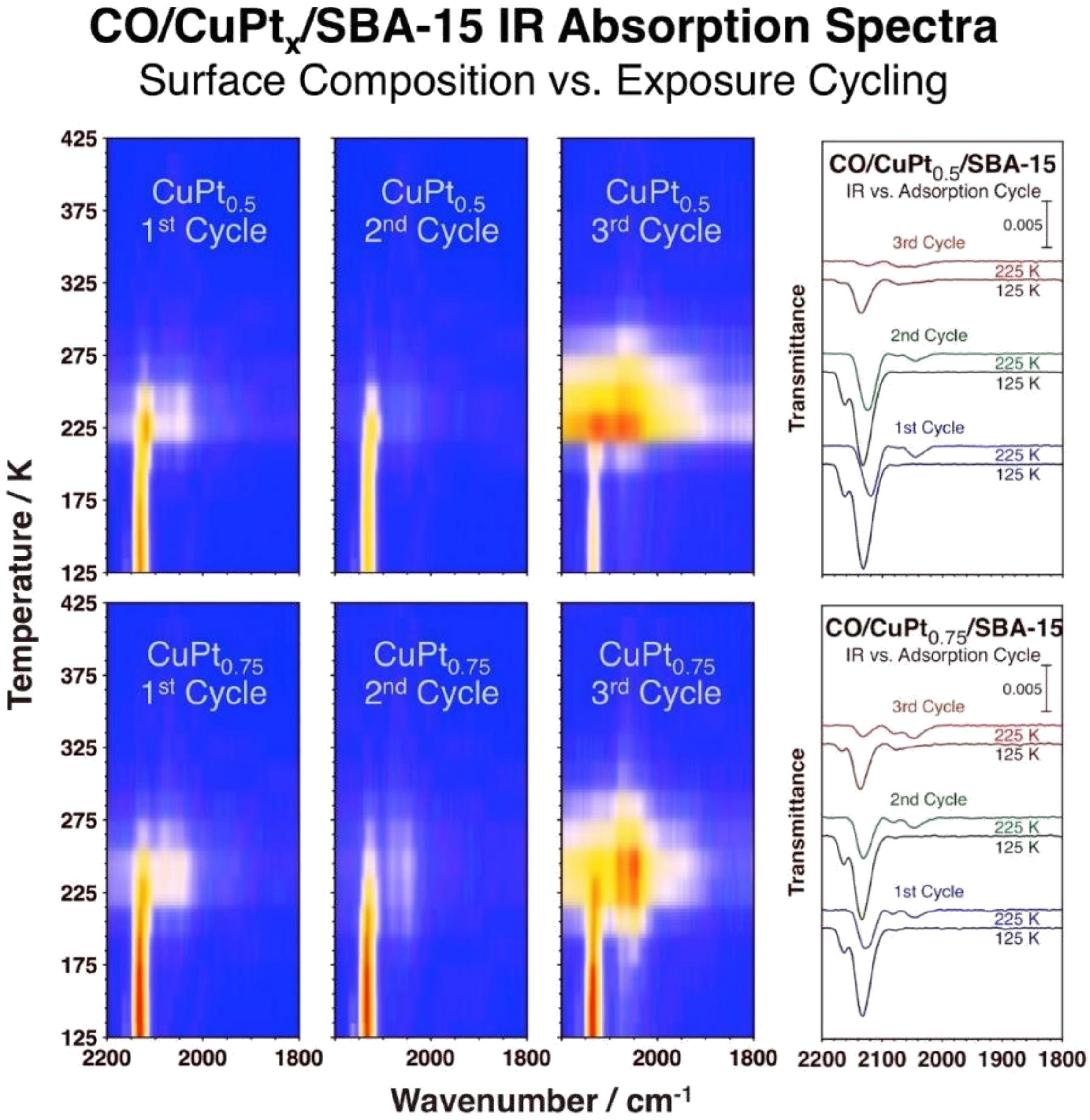

Figure 3-2. IR spectra for CO adsorbed on $CuPt_{0.5}$/SBA-15 (top) and $CuPt_{0.75}$/SBA15 (bottom) catalysts, recorded as a function of heating temperature during 3-cycle dose-pump-heat sequences. The left panels correspond to 3D "heat" plots, whereas the right figures report representative spectra for low (125 K) and high (225 K) temperatures during each of the three cycles.

The data presented so far were acquired *ex situ*, that is, under vacuum after having pumped the CO atmosphere from the IR cell. More relevant to the main goal of this project was the investigation of the behavior of the Cu-Pt bimetallic NPs *in situ*, in the presence of a gas phase. To achieve that, IR spectra were recorded under similar conditions, at different temperatures and in the presence of a fixed pressure of CO, both in the presence and in the absence of the catalysts in the path of the IR beam. This way, the contribution from the gas phase species detected in the latter could be subtracted directly from the former to extract the peaks attributable to the adsorbed species. This approach is feasible because when dealing with supported catalysts the area of the reactive surfaces is high and the total number of adsorbed molecules probed can reach values close to those of the gas-phase species. Figure 3-3 displays an example of the results acquired this way, in this case for the *in situ* titration of Cu and Pt sites in a $CuPt_{0.2}$/SBA-15 catalyst as a function of temperature using 10 Torr CO. Several features are seen, in particular a peak at 2137 cm^{-1} at low temperatures (295 K) corresponding to adsorption on copper surfaces. Interestingly, that feature slowly disappears with increasing temperature, presumably because CO binds weakly to Cu and desorbs at low temperatures, and is replaced by a new signal around 2050 cm^{-1} easily associated with Pt sites. A smaller and broader feature is already seen in this frequency region at low temperature, but the peak sharpens and grows at 495 K. It appears that the Pt atoms in the $CuPt_{0.2}$/SBA-15 catalyst, which may initially be located in the subsurface region, reversibly segregate to the surface at higher temperatures driven by the CO atmosphere.

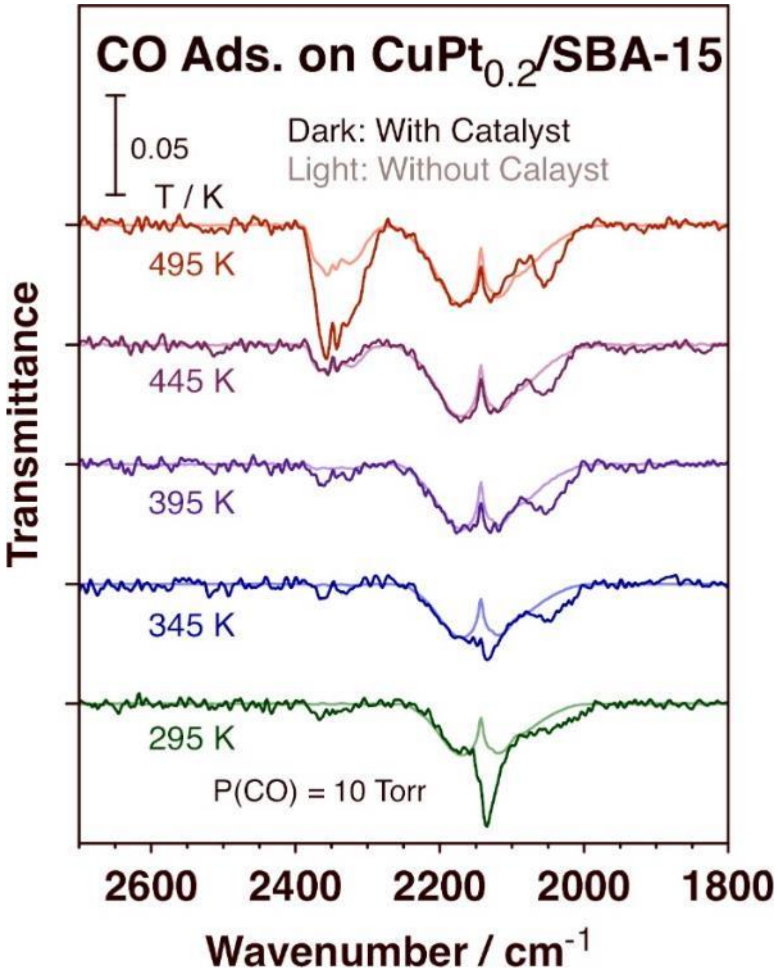

Figure 3-3. *In situ* IR spectra of CO adsorbed on a $CuPt_{0.2}$/SBA-15 catalyst as a function of temperature. The spectra were taken in the presence of 10 Torr of CO in the gas phase in order to maintain a steady-state coverage of adsorbed CO at temperatures typical of catalytic processes. Additional reference spectra were acquired without the catalyst (light traces) in order to subtract the contribution from the gas phase to the spectra.

Similar experiments were carried out with other $CuPt_x$/SBA-15 catalysts in order to characterize the behavior of these catalysts as a function of Pt content. Key results are displayed in Figure 3-4: spectra recorded under 50 Torr CO at room temperature (left panel), after heating to 495 K (center), and after cooling back down to room temperature again (to test the reversibility of the temperature-induced changes; right) with 8 catalysts, namely, the pure Cu/SBA-15 and Pt/SBA-15 samples, and $CuPt_x$/SBA-15 with x = 0.001, 0.005, 0.01, 0.05, 0.1 and 0.2. Here, the spectra after subtraction of the gas-phase contribution are shown for clarity. Similar features to those reported in Figure 3-3 were seen, namely, the peaks in the 2120 - 2130 and 2040 - 2080 cm^{-1} associated with bonding to Cu and Pt atop sites, respectively, and also an additional small feature at 2200 cm^{-1} most likely due to adsorption on oxidized Cu sites. A few trends become clear upon observation of this figure. For one, most (although not all) of the CO bonded to Cu desorbs by 495 K, due to the weak binding energy of those surface species. Not all of the CO is gone, however: the peak for Cu–CO retains approximately 20 - 30% of its initial intensity in going from 295 to 495 K, a reflection of the equilibrium that is established between the adsorbed and gas-phase molecules. In fact, the steady-state CO surface coverage can be increased by increasing the gas-phase CO pressure, as we have already demonstrated for the case of Cu/SBA-15 in a previous publication,[39] and as it can be seen in Figure 3-5, to be discussed later.

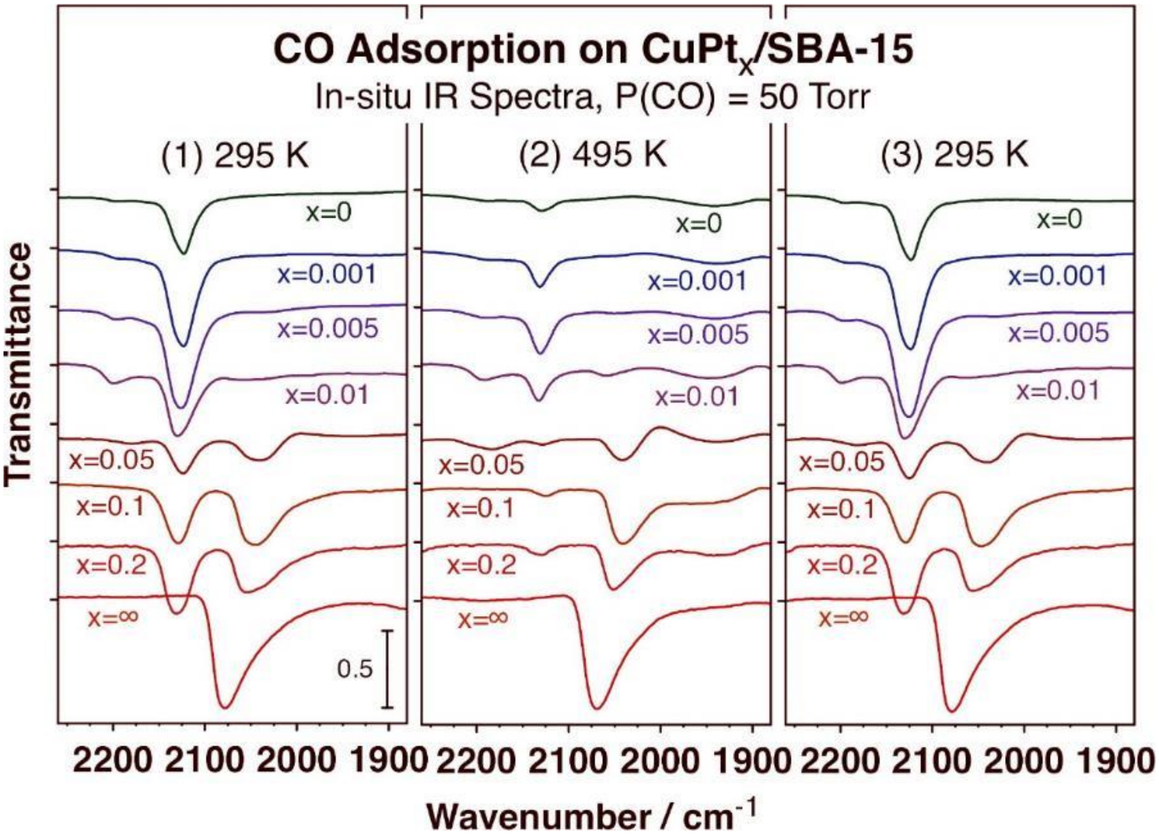

Figure 3-4. *In situ* IR spectra of CO adsorbed on a family of CuPt$_x$/SBA-15 catalyst as a function of Pt content (x), in the presence of 50 Torr of CO in the gas phase (after subtraction of the gas-phase contribution). Three panels are provided, showing the traces recorded at 295 K (left), after heating to 495 K (center), and upon cooling back down to 295 K again (right). These temperature cycling was designed to test the reversibility of the changes seen as a function of temperature.

The behavior of the IR peak associated with the Pt–CO species is somewhat different. With the more diluted alloys, for $x \leq 0.01$, the Pt content is low, and therefore the peak due to adsorption on Pt atoms is weak, as expected. What is significant is the fact that it is only seen at high temperatures, in the traces recorded at 495 K; the peaks at 2060 cm^{-1} (with CuPt$_{0.01}$/SBA-15) and 2035 cm^{-1} (CuPt$_{0.005}$/SBA-15) appear only while heating the reactor, and go away again once the sample is cooled back down to room temperature. In addition, the value of the frequencies is low but do not follow the same trends seen with higher Pt content; notice in particular that the C–O stretching of the Pt–CO species in $CuPt_{0.01}$/SBA-15 (2060 cm^{-1}) is higher than with $CuPt_{0.05}$/SBA-15 (2040 cm^{-1}), in spite of the fact that the intensity of the peak in the former case is much lower than in the latter. The Pt surface atoms in the diluted bimetallic catalysts appear to behave differently than in the catalysts with higher Pt content, and are likely to be isolated, as expected in SAAs. The most relevant observation here is the fact that, as already suggested by the *ex situ* IR experiments, adsorbed CO appears to help draw the Pt atoms toward the surface at high temperatures, and reversibly drive them into the bulk at low temperatures.

For the alloys with high Pt content, $x \geq 0.05$, the peak position associated with CO bonded to Pt blue-shifts significantly with increasing Pt content in the Cu-Pt bimetallic NPs, from 2040 cm^{-1} in $CuPt_{0.05}$/SBA-15 to 2070 cm^{-1} in Pt/SBA-15. These shifts are accompanied by related increases in peak intensity, due to increases in the surface coverage of Pt atoms, and can be explained by an increase in dipole-dipole intermolecular interactions, as has been reported and amply discussed in studies with Pt single crystals.[49-51] It seems that at these high Pt loadings CO behaves as in regular alloys with multi-atom Pt assemblies on the surface; these are not SAA catalysts. It is interesting to point out that the peak shifts seen in the IR feature for Cu–CO sites are well less marked, suggesting that the surfaces of these catalysts are still dominated by Cu. It is also worth noticing that in Figure 3-4 both the peak positions and the peak intensities of the feature for Pt–CO do not change significantly upon heating or cooling of the catalysts. Some sharpening and growth of that peak was seen in some cases, more clearly in the data in Figure 3-3 (the data in Figure 3-3 and Figure 3-4 are from different experiments, performed at different CO pressures), but the changes are not as significant as with the more diluted alloys.

That lack of sensitivity of the IR features to changes in temperature with the high-Pt content catalysts as explored in more detail next. It was found that thermal treatment of the high-Pt-content catalysts in the presence of a gaseous atmosphere still leads to intermetallic atom mobility within the individual NPs, only that the behavior is complex as it depends on both temperature and CO pressure. This can be seen more clearly in Figure 3-5, where CO IR spectra are shown for $CuPt_{0.2}$/SBA-15 as a function of temperature for several CO pressures. Peaks for both Cu–CO and Pt–CO sites are seen in all cases, but their absolute and relative intensities as well as their shapes change with varying conditions. The signals from the Cu–CO species go up in intensity with CO pressure, and down with increasing temperature, both expected behaviors. In the case of the Pt sites, however, the trends are reversed. Interestingly, in general, the peak for Pt–CO is more intense and sharper at the lower CO pressures, with the one exception of the 1 Torr CO at 495 K (in that case, the CO may have been consumed in oxidation reactions). These results suggest that at low temperatures higher gas pressures induce partial segregation of Pt into the bulk of the bimetallic NPs. It is also seen that more surface Pt is detected in going from 295 K to 395 K, following the same trend discussed above for the more diluted alloys, but then less Pt–CO is seen at 495 K. It could be thought that Pt may diffuse back into the bulk in this latter case, but in fact we believe that the observed behavior is the result of a thermodynamic effect, as the rate of CO desorption increases with T and leads to lower steady-state surface CO coverages. In the end, the *in situ* IR data are all consistent with Pt diffusing into the bulk in the presence of CO at low temperatures and segregating back to the surface as the catalysts are heated.

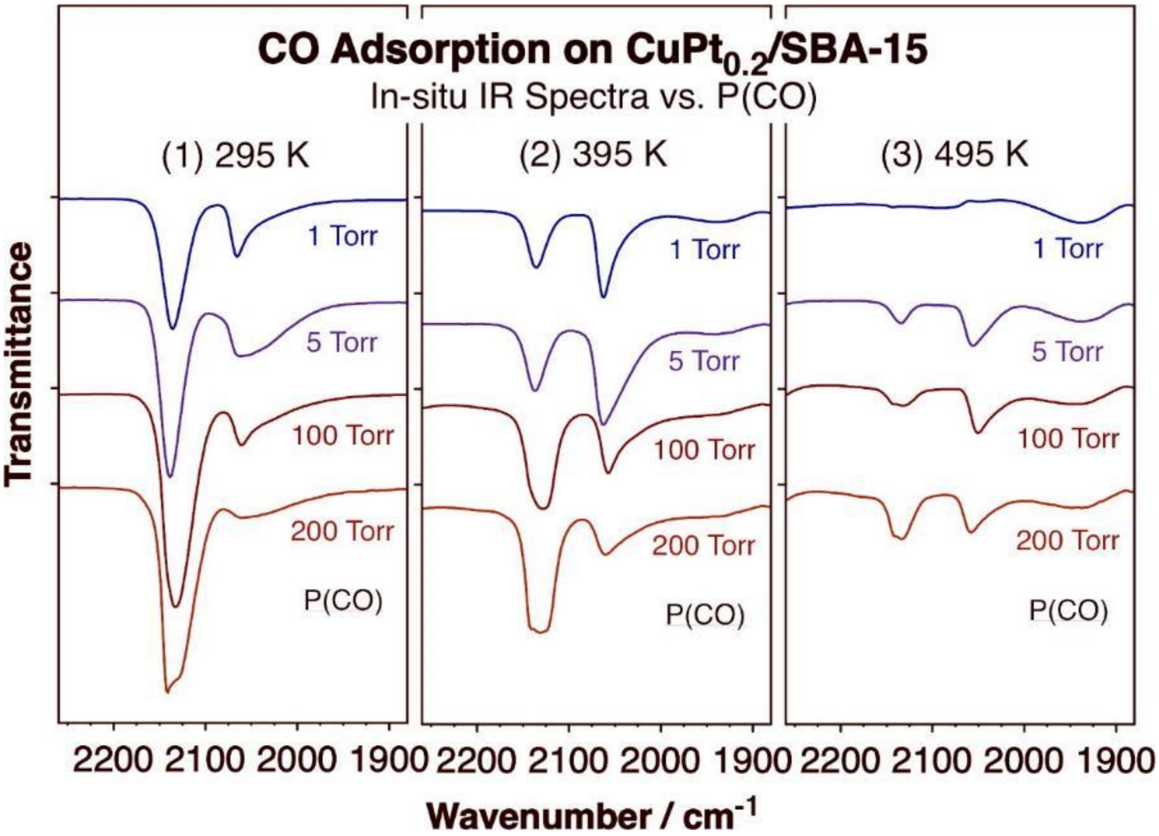

Figure 3-5. *In situ* IR spectra of CO adsorbed on the $CuPt_{0.2}$/SBA-15 catalyst as a function of CO pressure (after subtraction of the gas-phase contribution). Three panels are provided, showing the traces recorded at 295 K (left), 395 K (center), and 495 K (right).

The IR characterization of our Cu-Pt bimetallic catalysts has been carried out by using CO as a probe molecule, in a CO environment. CO is an important reactant in many catalytic processes, but is to be avoided in hydrogenation reactions. More relevant in those cases is the behavior of the surface of the catalyst under reducing conditions, H_2 atmospheres if possible. Unfortunately, adsorbed hydrogen is virtually invisible in IR, at least in supported catalysts (vibrational spectra, taken using high-resolution electron loss spectroscopy –HREELS–[52-53] or inelastic neutron scattering –INS–,[54-56] have been reported with some Pt systems). Instead, an attempt was made here to test the performance of the $CuPt_x$/SBA-15 catalysts under hydrogen atmospheres in an indirect way. Two types of experiments were carried out (Figure 3-6). In the first, the catalyst ($CuPt_{0.1}$/SBA-15 in this case) was first reduced in a H_2 atmosphere (200 Torr at 495 K) and then probed by adding a small amount of CO to the gas at room temperature (300 K; Figure 3-6, left panel): after an initial addition of 0.2 Torr CO no adsorption could be detected, but upon adding another 0.2 Torr CO, two peaks were clearly seen at 2127 and 2029 cm^{-1} corresponding to the C–O stretching mode of CO adsorbed on atop sites of metallic Cu and Pt surfaces, respectively. The interesting observation here is that the intensities of both features increase after each of two consecutive cycles of heating the sample from 300 K to 495 K and cooling it back to 300 K. The growth of the peak for Cu–CO is explained by the reduction of the Cu_2O surface layer that presumably was not fully removed during the H_2 treatment by the added CO, and to the resulting creation of additional metallic Cu sites available for CO uptake; further confirmation of this interpretation is given by the growth of the peaks in the 2300 - 2400 cm^{-1} range due to gas-phase CO_2, the product of CO oxidation. Importantly, the signal for the Pt–CO site grows faster relative to that for Cu–CO, suggesting that H_2 may help draw the Pt atoms to the surface as a result of the high-temperature cycling.

The second set of experiments were done using H_2 + CO gas mixtures, 100 Torr H_2 + 0.2 Torr CO in the example shown in the right panel of Figure 3-6 (which corresponds to a $CuPt_{0.2}$/SBA-15 catalyst). The peak at 2132 cm^{-1} for CO adsorption on metallic Cu is again seen to grow upon cycling to 495 K and back, a procedure that was carried out three times in this example. The same explanation applies to this system, namely, that the small amount of CO added to the H_2 gas helps complete the reduction of the metal NPs, removing the residual Cu_2O layer present on the surface under H_2 atmospheres at low temperatures. Unfortunately, in this case adsorption on Pt atoms was not evident at any stage of the experiments. In the end, small amounts of CO were used in both examples in order to minimize its interference in the behavior of the catalyst under H_2 atmospheres, but a CO reducing effect was nevertheless identified. Some interference is unavoidable, more obviously perhaps in the second example, where the chances of surface site poisoning are greater. An alternative experimental approach is needed to probe the surfaces of these catalysts *in situ* in atmospheres not containing CO. We addressed this challenge by incorporating XAS to our studies.

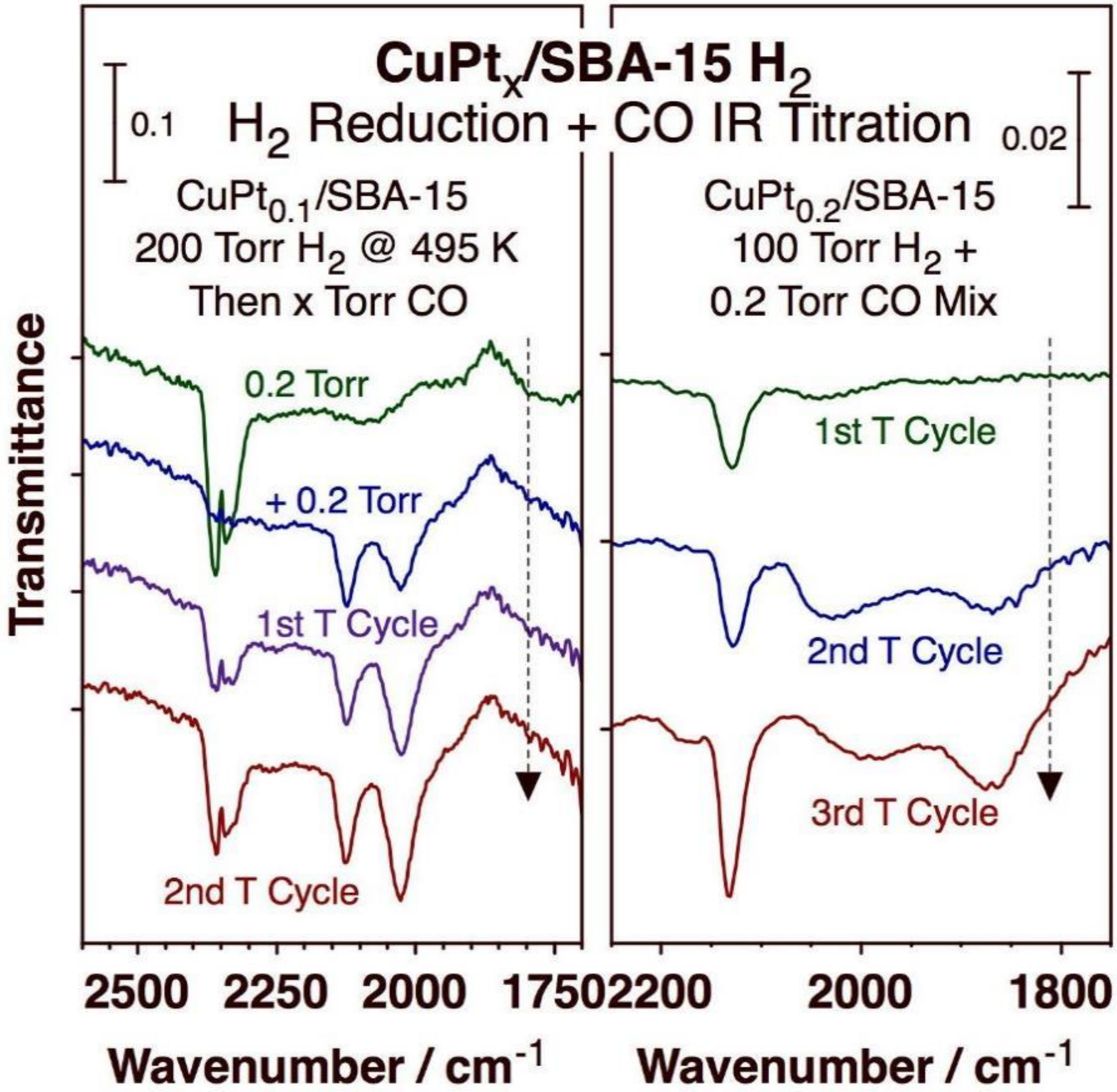

Figure 3-6. IR spectra of CO adsorbed on CuPt$_x$/SBA-15 catalysts after different H$_2$ reduction treatments. Left: Spectra for CuPt$_{0.1}$/SBA-15 reduced in a 200 Torr H$_2$ atmosphere, after adding a small amount (0.2 Torr twice) of CO and cycling the temperature to 495 K and back to 300 K. Right: Data for CuPt$_{0.2}$/SBA-15 exposed to a 100 Torr H$_2$ + 0.2 Torr CO mixture; the spectra were obtained after each of three consecutive heating cycles to 495 K and cooling back down to 300 K.

XAS characterization of our catalysts can provide information on several aspects of their physical properties. In Figure 3-7, we report data recorded *in situ* under different gas atmospheres in the near-edge region (XANES) around the Pt L_3-edge in order to probe the electronic properties of the Pt atoms. The two low traces in the left panel of that figure contrast the spectra obtained for a $CuPt_{0.2}$/SBA-15 catalyst as is, before any pretreatment, versus that for a reference PtO_2 sample. The similarity between the two indicates that, initially, the platinum in our alloy catalyst is in an oxidized state, most likely in a Pt^{4+} state. The match of the two spectra is not complete because of the dispersed nature of the Pt atoms within the Cu-based matrix in the supported NPs of the catalyst.

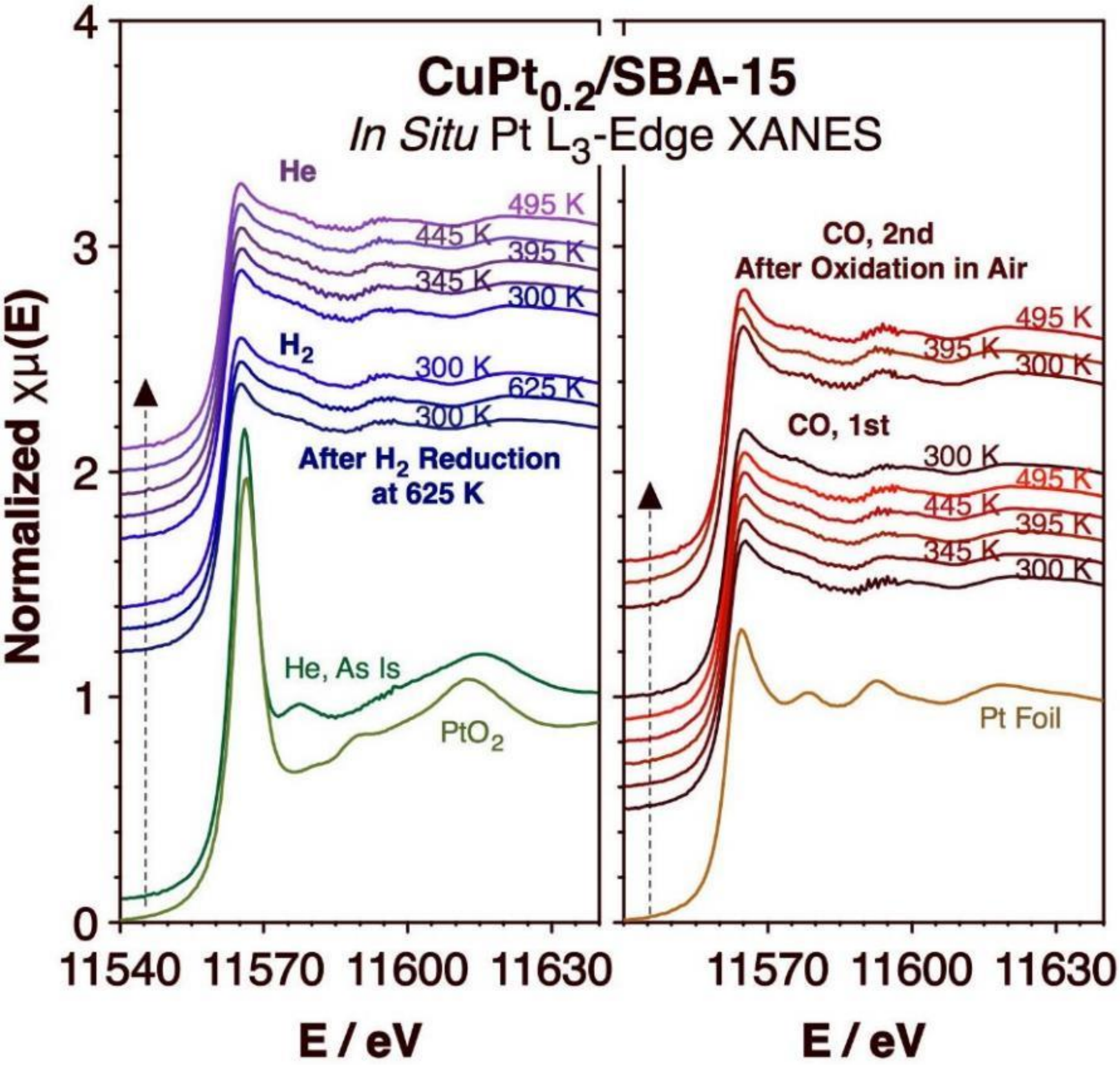

Figure 3-7. *In situ* X-ray absorption near edge spectra (XANES) recorded around the Pt L_3 edge for a CuPt$_{0.2}$/SBA-15 catalyst exposed to different gases (H_2, He, CO) and cycled between 300 and 495 K. Reference spectra from PtO$_2$ (left) and a Pt foil (right) are also provided at the bottom for reference. No detectable changes in Pt electronic properties were seen in any case after initial reduction of the catalyst.

The reminder of the traces reported in Figure 3-7 corresponds to the Pt L_3-edge XANES of the same $CuPt_{0.2}$/SBA-15 catalyst obtained after high-temperature (625 K) pretreatment in H_2. The data are grouped to highlight the behavior of the catalyst as they were subjected to heating-cooling cycles (from 300 K to 625 K and back) under different gas atmospheres: H_2 (left panel, 3rd to 5th traces, counting from the bottom), He (left panel, 5 top traces), and CO (right panel, 2nd to 6th traces from the bottom). Interestingly, all these spectra look the same, indicating that the electronic properties of the Pt atoms in the bimetallic catalyst are not significantly affected by the nature of the gas or the temperature (within the range tested here). Comparison with a spectrum obtained with a reference Pt foil (right panel, bottom) points to the fact that the Pt atoms are most likely in a zero-valent state; the peaks are seen at approximately the same energies, and their lower intensities can again be explained by the dilute nature of the Pt within the Cu-based alloy. Even after exposure to air (at room temperature, 30 min; right panel, top three traces), not much change is detected: a minor oxidation may be detectable then, but the Pt atoms in that case are readily re-reduced to metallic Pt upon re-exposure to CO.

Additional information on the local environment surrounding the Pt atoms in our catalysts can be extracted from analysis of the extended X-ray absorption fine structure (EXAFS) in the spectra at the Pt L_3-edge region. In Figure 3-8, the radial distributions obtained by Fourier transformation of that fine structure as a function of momentum (k) is reported for the $CuPt_{0.2}$/SBA-15 catalyst while cycling the temperature from 300 to 495

K and back under CO (left panel) and He (right) atmospheres. In all cases, the main peak is seen at R ~ 2.23Å, which corresponds to individual Pt atoms bonding to Cu neighbors; it suggests that the Pt is dispersed within the Cu-Pt alloyed NPs. A shoulder is also seen around 2.9 Å, pointing to the fact that some Pt atoms are directly bonded to other Pt atoms. The peak intensities decrease with increasing temperature, but that can be mostly accounted for by the so-called Debye-Waller factor that reflects the attenuation of X-ray scattering caused by thermal motion. Noticeably, similar behavior is seen in CO versus He atmospheres.

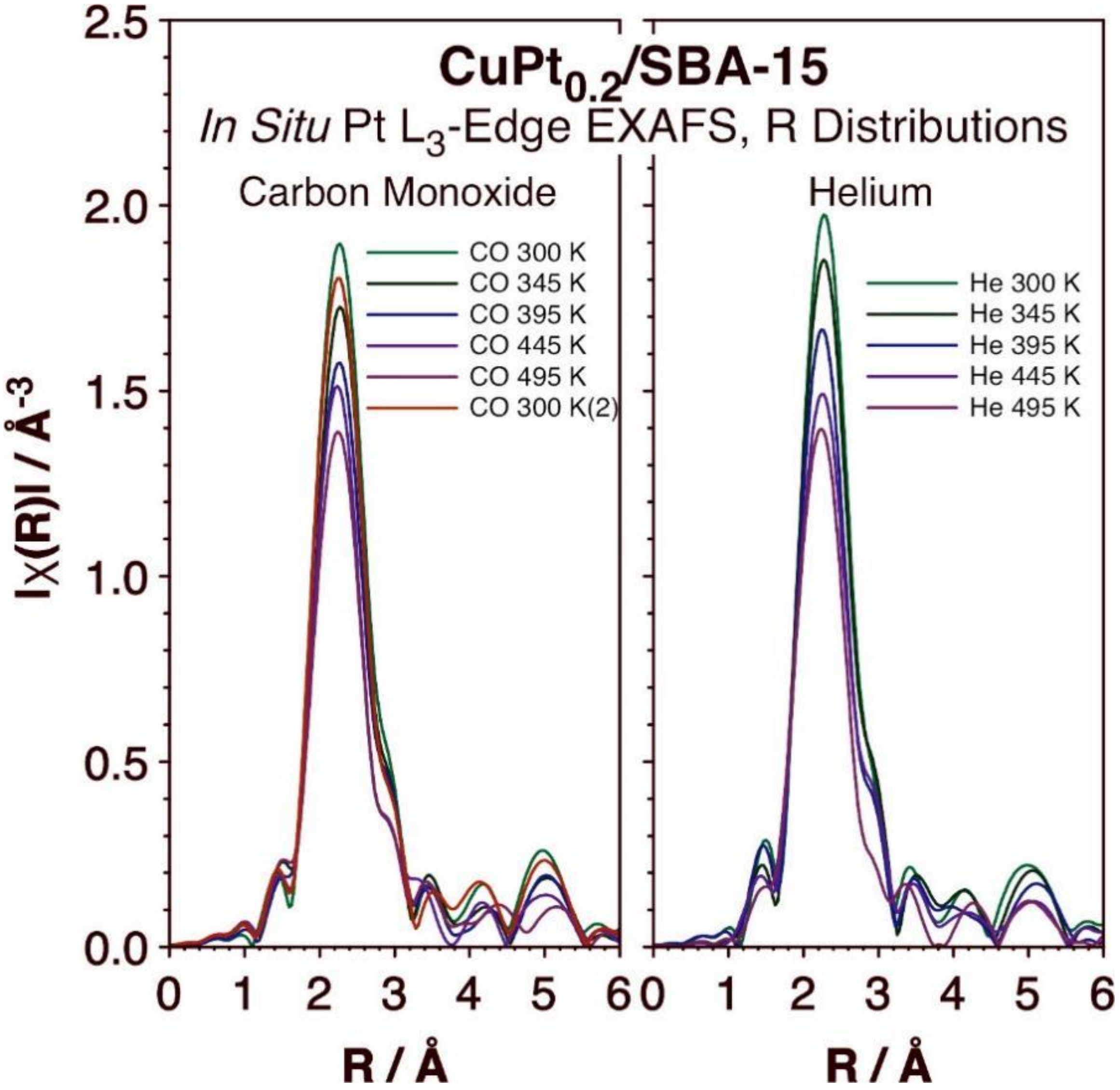

Figure 3-8. Pt L$_3$-edge EXAFS radial distributions obtained for our CuPt$_{0.2}$/SBA-15 catalyst *in situ* in CO (left) and He (right) atmospheres as a function of temperature, which was cycled between 300 and 495 K.

Figure 3-9 shows the results from processing of the EXAFS data to extract quantitative parameters on the coordination sphere around the Pt and Cu atoms, specifically on coordination numbers (left, CN) and bond distances (right, d) as a function of temperature under both CO and He atmospheres. Data are reported for data from both the Pt L_3 and Cu K edges (the raw data for the Cu K edge are not shown). The coordination number around the Cu atoms hovers around 10-11 in all cases, almost all to other Cu atoms (red lines and symbols). This number is just shy of the value of 12 expected in bulk Cu, a reflection of the small size of the NPs and to the resulting existence of a detectable fraction of Cu atoms in lower-coordination surface sites. Using a back-of-the-envelop calculation, since in 5 nm spherical NPs (the average size in our $CuPt_{0.2}$/SBA-15 sample)[18] the fraction of atoms on the surface is approximately 25%, an average CN of 6 for those (it is 9 in the (111) plane) results in an average total CN of 10.5, within the range measured here. There is a slight decrease in CN at 495 K, which we associate with the higher coordination of Cu atoms to Pt atoms highlighted by the changes in CNs for Pt discussed next. The Cu–Cu bond distances are also within the value measured for bulk Cu. (2.542 Å).

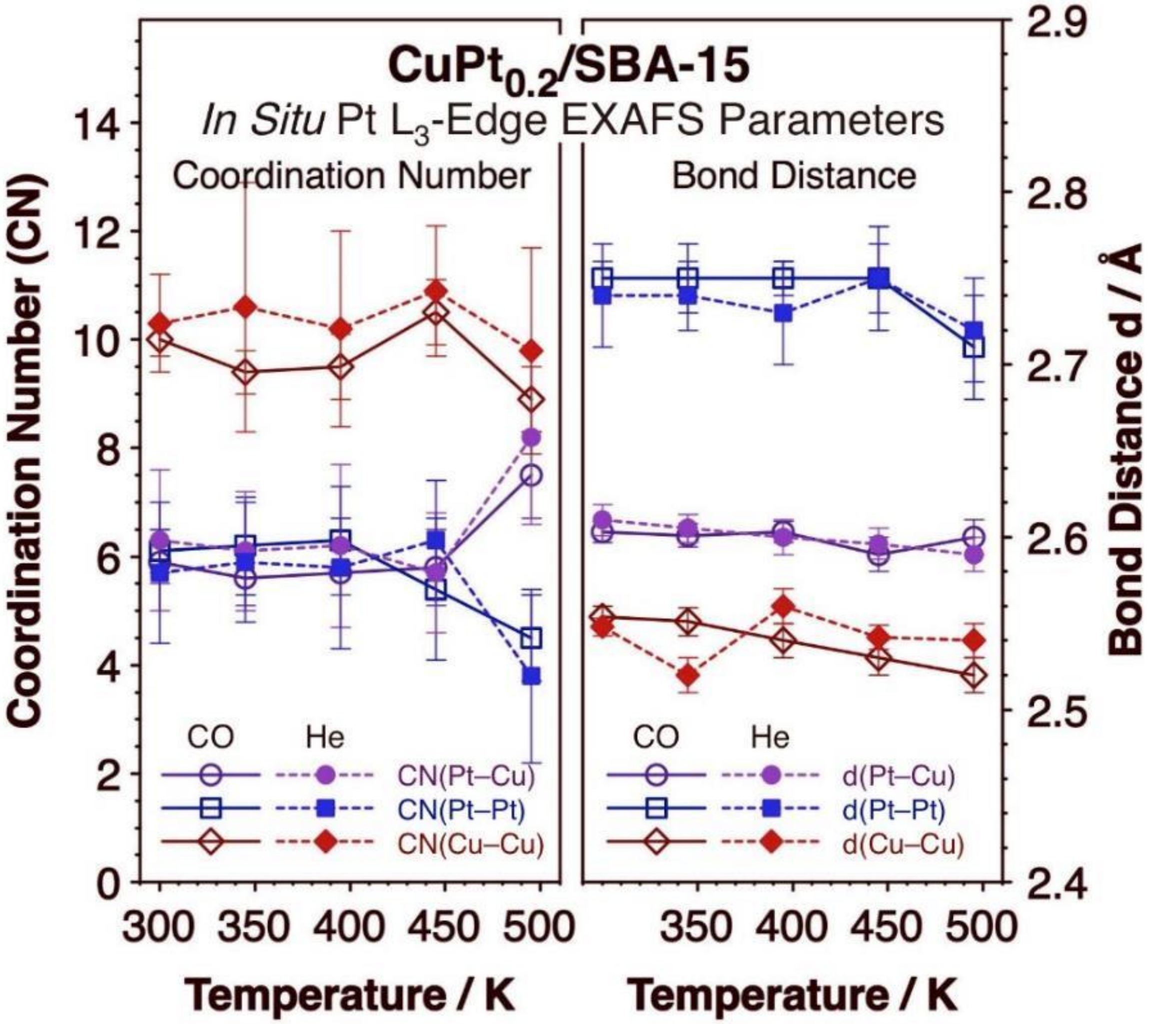

Figure 3-9. Coordination numbers (CN, left panel) and bond distances (d, right) extracted from analysis of the EXAFS data obtained at the Pt L_3 and Cu K edges (the latter not shown) for the $CuPt_{0.2}$/SBA-15 catalyst under either CO or He environments, all as a function of temperature.

More relevant to our discussion is the environment surrounding the Pt atoms. Again, the behavior seen for those atoms as a function of temperature are similar in the CO and He atmospheres. In both cases, the coordination around individual Pt atoms is split about evenly, ~ 6:6, between Cu and Pt neighbors for temperatures up to 445 K. At 495 K, however, the Pt atoms are surrounded by a significantly larger number of Cu neighbors, at the expense of Pt–Pt pairs (Cu:Pt ~ 8:4). At the very least, this indicates some mobility of the Pt atoms within the bimetallic NPs induced by heating in a gaseous atmosphere. The changes also point to better Cu-Pt mixing at high temperatures, consistent with the CO IR data, and can be explained by segregation of Pt to the surface. The total CN around the Pt atoms adds up to approximately 12 in all cases, as expected for atoms in the bulk, but the lower values expected from having a fraction of the Pt atoms on the surface are within the experimental errors of the EXAFS data. There are still some Pt–Pt bonds in all cases, with bond distances slightly lower than that seen in the Pt foil reference (2.764 Å), and there also seem to be a slight contraction of that bond at 495 K. Incidentally, all of these changes proved to be reversible, as the structural parameters return to the initial values upon cooling of the catalyst back to room temperature.

The main purpose of this research has been to characterize the behavior of $CuPt_x$/SBA-15 bimetallic catalysts *in situ* in the presence of atmospheric pressures of reactive and non-reactive gases. Because of their potential use in selective catalysis, in particular to promote selective hydrogenation conversions, the surface chemistry of the Cu-Pt bimetallic combination has been characterized extensively under controlled vacuum conditions (as mentioned in the Introduction). However, much less is known about its performance under realistic catalytic conditions. It is well known that both temperature and chemical environments can induce segregation of one or more components of metal alloys toward the surface, and if so, change the nature of the catalytic surface. In the case of single-atom alloy (SAA) catalysts in particular, the placement of the minority component, on the surface versus dissolved inside the bulk, is expected to determine the mechanism by which reactions occur on such catalysts. Here we have investigated the specific case of Cu-Pt bimetallics, but these issues are general. *In situ* characterization of SAA catalysts is required to develop a picture of the nature of the surface that promotes the catalytic reactions.

One of the clear conclusions of this work is that, indeed, the presence of a gaseous atmosphere leads to the thermally promoted diffusion of Pt within the Cu-Pt bimetallic NPs. In fact, even under vacuum a reactive gas such as CO can cause the segregation and/or desegregation of Pt atoms in those catalysts. Specifically, Figure 3-1 shows that, at least for high-content $CuPt_x$/SBA-15 catalysts ($x \geq 0.2$), binding of CO to Pt atoms cannot be detected at 125 K but it is seen to develop at temperatures as low as 225 K. This change indicates that the Pt atoms diffuse to the surface in between those two temperatures, likely aided by the presence of CO molecules on the surface. The binding of CO on the new sites is weaker than on pure Pt, but it is clearly stronger than on Cu/SBA-15. Another important observation regarding the changes of the $CuPt_x$/SBA-15 catalyst upon thermal cycling after exposure to CO is that the Pt segregation seen in

Figure 3-1 is reversible; cooling the catalysts back down to room temperature followed by CO re-dosing leads to the disappearance of the IR features associated with CO adsorption on Pt (Figure 3-2). By and large, this behavior is reproduced during multiple CO-dosing/heating cycles.

A similar behavior was observed *in situ* in the presence of CO atmospheres, as indicated by the IR data in Figure 3-3, Figure 3-4, and Figure 3-5: clear peaks are seen at 2137 and 2050 cm^{-1} at 295 and 495 K with $CuPt_{0.2}$/SBA-15 clearly originating from surface species and easily assignable to CO bonding to Cu and Pt sites, respectively. Additionally, the changes seen upon heating and cooling of the $CuPt_x$/SBA-15 catalysts are, again, reversible. It should be indicated that in the catalysts containing high Pt loadings ($x \geq 0.05$) CO adsorption on Pt was seen at all temperatures; it is only with the diluted SAA catalysts ($x \leq 0.01$) that no surface Pt is detected at low temperatures and reversible segregation of Pt to the surface is clearly observed at high temperatures, possibly driven by bonding to CO. This does not indicate that segregation does not occur with the high-Pt-content catalysts, only that in those cases the behavior is masked by the combined response of the bimetallic NPs to changes in both temperature and CO pressure.

Complementary information could be extracted from *in situ* XAS experiments. The XANES data reported in Figure 3-7 for $CuPt_{0.2}$/SBA-15 does not show much change in the electronic structure of Pt as a function of temperature or the nature of the gas surrounding the surface of the catalyst, consistent with the IR experiments. The main conclusion that can be driven there is that the features in the XANES traces with the bimetallic catalysts are much less defined than in pure Pt samples, suggesting good mixing with the Cu matrix and broadening of the Pt d band. On the other hand, analysis of the EXAFS data in Figure 3-8 and Figure 3-9 does highlight a critical structural transition in $CuPt_{0.2}$/SBA-15 upon heating to 495 K. Specifically, the coordination sphere around the Pt atoms exhibits approximately the same number of Pt and Cu neighbors at low temperatures, but a significant increase in Cu–Pt bonds, at the expense of Pt–Pt pairs, is seen after heating to 495 K. This transition was observed in both reactive (CO) and un-reactive (He) atmosphere, and was found to be reversible, with the atoms redistributing back to their original configuration upon cooling back down to room temperature.

The high coordination number of Pt bonding to other Pt atoms at low temperature indicates that Pt must form large ensembles within the bimetallic NPs. Two possible models can be conceived to explain the results: either Pt forms small clusters within the larger Cu-Pt NPs, or, more likely, it may form shells, in a layered distribution of the metals within the NPs. The detection of CO adsorption in the IR experiments indicates that some Pt atoms are present on the surface of the catalyst at all temperatures, but the majority of the Pt may still be located in the sub-surface at low temperatures, perhaps separated by an intermediate Cu layer. After heating to 495 K, on the other hand, the CN for Pt–Pt pairs is significantly reduced, pointing to a better intermixing of the two metals. In addition, the CO IR peak associated with bonding to Pt becomes somewhat larger and sharper (Figure 3-3), possibly because of a higher coverage of Pt on the surface but in a better dispersed fashion. Old reports on the structure of Cu-Pt bimetallic samples provide support for this interpretation of the data, in that: (1) Cu and Pt are completely miscible in both bulk and NP forms,[57] and (2) the superlattice of Cu-Pt alloys is characterized by successive alternating Cu-only and Pt-only layers.[58] More relevant to the understanding of our results, Cu-Pt alloys are known to transition from solid solutions at high temperatures to a number of ordered structures at low temperatures.[59-60] For a $x = 0.2$ composition (Pt molar fraction) this transition has been reported to take place at $T \geq 900$ K, but that is in bulk samples; the thermodynamics of NPs is expected to be different. In fact, several layered structures with surface Pt rows and/or subsurface Pt sheets have been shown to be stable in $CuPt_x$ NPs by density-functional theory (DFT) calculations.[61-62] In addition, we suggest that the interaction of the bimetallic NPs with gases may help lower the temperature of the transition. Importantly, the transitions reported here were seen with both CO and He atmospheres, which means that the strong binding of CO to Pt may not be the dominating force driving them.

Changes in surface chemistry due to the preferential segregation of one element in bimetallic NPs has been recognized in the past, as discussed in the Introduction, and some specific examples have already been reported for Cu-Pt and similar cases. For instance, high-temperature CO-induced segregation of Pt atoms in Pt-doped Cu(111) surfaces has been identified by NAP-XPS.[26] The same behavior was seen with Pd/Ag(111),[29] but not with Pt/Cu(111) when H_2 is used instead of CO.[30] It is also interesting to note that no isotope scrambling within H_2-D_2 mixtures was detected in experiments with $CuPd_x$ alloy films at any temperature below ~ 550 K until a ∼ 15 mol

% Pd content was reached, a result that implies than no Pd atoms are accessible on the surface of diluted alloys for this catalysis.[10] Even under UHV, CO oxidation on Pt-doped O-dosed Cu(111) surfaces has been shown to lead to the diffusion of the Pt atoms underneath the Cu–O layer,[63] a behavior consistent with our temperature-dependent IR observations reported in Figure 3-1 and Figure 3-2.

3.3 Conclusion

A synergy between Cu and Pt in Cu-Pt bimetallic catalysts was evidenced by their behavior both upon the uptake of CO under vacuum and their exposure to atmospheric pressures of either CO or He. CO adsorption on $CuPt_x$/SBA-15 catalysts only involve bonding to Cu sites at low (125 K) temperatures regardless of the Pt content (the x value), indicating the absence of Pt atoms on the surface (Figure 3-1, left). Pt segregation becomes evident after heating to 225 K for $x \geq 0.2$ by the growth of a new peak in the IR spectra around 2044 - 2050 cm^{-1} (Figure 3-1, second-from-left) but CO adsorption on those sites is still weaker than in pure Pt, desorbing at lower temperatures (Figure 3-1, two right panels). The low frequency of the peaks for the Pt–CO IR sites suggest atomic dispersion, as expected in single-atom alloy (SAA) catalysts, and the Pt segregation is partially reversible under the vacuum conditions of these experiments, as CO readsorption at room temperature leads to the disappearance of the IR feature for Pt–CO IR seen at the higher temperatures (Figure 3-2).

Pt surface segregation at high (495 K) temperatures is also observed under a CO atmosphere, evidenced by the growth of a new peak around 2050 cm^{-1} in the *in situ* IR data (Figure 3-3). The absence of CO adsorption at low temperatures and the reversibility of the Pt segregation to the surface at high temperatures are easy to see in diluted SAA $CuPt_x$/SBA-15 catalysts ($x \leq 0.01$; Figure 3-4). With bimetallic catalysts with higher Pt content some Pt–CO sites can be detected even at low temperatures (Figure 3-4), but some Pt diffusion in and out of the surface still occurs, only that it is highly dependent on the temperature and CO pressure used (Figure 3-5). The possible Pt atom mobility within Cu-Pt NPs in the presence of H_2 atmospheres was also probed indirectly with *in situ* IR by adding small amounts of CO added to the gas mixtures either during or after the thermal cycles (Figure 3-6): it would appear that Pt segregation is also aided by H_2, but this conclusion is not definitive because of the possible interference of the CO probe molecule.

Finally, the behavior of the $CuPt_{0.2}$/SBA-15 catalyst under CO and He atmospheres was also investigated *in situ* by XAS. The near-edge region (XANES) of the spectra attests to the metallic and dispersed nature of the Pt atoms, and an electronic structure not significantly affected by the presence of gases or temperature (Figure 3-7). On the other hand, analysis of the extended structure (EXAFS; Figure 3-8) highlights a significant change in the coordination sphere around the Pt atoms upon heating of the catalyst. Specifically, the coordination numbers for neighboring Cu and Pt atoms switch from approximately 6:6 at 445 K or below to 8:4 at 495 K (Figure 3-9), indicating better intermetallic mixing at high temperatures and possibly additional Pt segregation to the surface, consistent with the IR results. Interestingly, the same behavior was seen with both CO and He, suggesting that the strong binding of CO to Pt may not be the main driving force justifying the diffusion reported here. It should be indicated that the segregation of Pt atoms in between the bulk and surface of the bimetallic NPs with high-Pt-content catalysts is not easy to isolate because of the presence of some Pt atoms on the surface even at low temperatures. For that, work with more diluted SAAs is desirable. We are in the process of performing *in situ* IR and XAS experiments like those reported here with more diluted alloys.

3.4 Reference

1. Sarfraz, S.; Garcia-Esparza, A. T.; Jedidi, A.; Cavallo, L.; Takanabe, K., Cu–Sn Bimetallic Catalyst for Selective Aqueous Electroreduction of CO_2 to CO. *ACS Catal.* **2016,** *6* (5), 2842-2851.

2. Duchesne, P. N.; Li, Z. Y.; Deming, C. P.; Fung, V.; Zhao, X.; Yuan, J.; Regier, T.; Aldalbahi, A.; Almarhoon, Z.; Chen, S.; Jiang, D.-e.; Zheng, N.; Zhang, P., Golden single-atomic-site platinum electrocatalysts. *Nat. Mater.* **2018,** *17* (11), 1033-1039.

3. Han, J.; Lu, J.; Wang, M.; Wang, Y.; Wang, F., Single Atom Alloy Preparation and Applications in Heterogeneous Catalysis. *Chin. J. Chem.* **2019,** *37* (9), 977-988.

4. Hannagan, R. T.; Giannakakis, G.; Flytzani-Stephanopoulos, M.; Sykes, E. C. H., Single-Atom Alloy Catalysis. *Chemical Reviews* **2020,** *120* (21), 12044-12088.

5. Zaera, F., Designing Sites in Heterogeneous Catalysis: Are We Reaching Selectivities Competitive With Those of Homogeneous Catalysts? *Chemical Reviews* **2022,** *122* (9), 8594-8757.

6. Johansson, M.; Lytken, O.; Chorkendorff, I., The sticking probability for H_2 on some transition metals at a hydrogen pressure of 1 bar. *J. Chem. Phys.* **2008,** *128* (3), 034706.

7. Álvarez-Falcón, L.; Viñes, F.; Notario-Estévez, A.; Illas, F., On the hydrogen adsorption and dissociation on Cu surfaces and nanorows. *Surf. Sci.* **2016,** *646*, 221-229.

8. Chen, B.; Zaera, F., Hydrogenation of Cinnamaldehyde on Cu(110) Single-Crystal Surfaces. *J. Phys. Chem. C* **2021,** *125* (27), 14709–14717.

9. O'Brien, C. P.; Miller, J. B.; Morreale, B. D.; Gellman, A. J., The Kinetics of H_2–D_2 Exchange over Pd, Cu, and PdCu Surfaces. *J. Phys. Chem. C* **2011,** *115* (49), 24221-24230.

10. Gumuslu, G.; Kondratyuk, P.; Boes, J. R.; Morreale, B.; Miller, J. B.; Kitchin, J. R.; Gellman, A. J., Correlation of Electronic Structure with Catalytic Activity: H_2–D_2 Exchange across Cu_xPd_{1-x} Composition Space. *ACS Catal.* **2015,** *5* (5), 3137-3147.

11. Luneau, M.; Lim, J. S.; Patel, D. A.; Sykes, E. C. H.; Friend, C. M.; Sautet, P., Guidelines to Achieving High Selectivity for the Hydrogenation of α,β-Unsaturated Aldehydes with Bimetallic and Dilute Alloy Catalysts: A Review. *Chem. Rev.* **2020,** *120* (23), 12834-12872.

12. Sykes, E. C. H.; Christopher, P., Recent advances in single-atom catalysts and single-atom alloys: opportunities for exploring the uncharted phase space in-between. *Current Opinion in Chemical Engineering* **2020,** *29*, 67-73.

13. Boucher, M. B.; Zugic, B.; Cladaras, G.; Kammert, J.; Marcinkowski, M. D.; Lawton, T. J.; Sykes, E. C. H.; Flytzani-Stephanopoulos, M., Single atom alloy surface analogs in Pd0.18Cu15 nanoparticles for selective hydrogenation reactions. *Physical Chemistry Chemical Physics* **2013,** *15* (29), 12187-12196.

14. Lucci, F. R.; Liu, J.; Marcinkowski, M. D.; Yang, M.; Allard, L. F.; Flytzani-Stephanopoulos, M.; Sykes, E. C. H., Selective hydrogenation of 1,3-butadiene on platinum–copper alloys at the single-atom limit. *Nature Communications* **2015,** *6*, 8550.

15. Pei, G. X.; Liu, X. Y.; Yang, X.; Zhang, L.; Wang, A.; Li, L.; Wang, H.; Wang, X.; Zhang, T., Performance of Cu-Alloyed Pd Single-Atom Catalyst for Semihydrogenation of Acetylene under Simulated Front-End Conditions. *ACS Catal.* **2017,** *7* (2), 1491-1500.

16. Luneau, M.; Shirman, T.; Foucher, A. C.; Duanmu, K.; Verbart, D. M. A.; Sautet, P.; Stach, E. A.; Aizenberg, J.; Madix, R. J.; Friend, C. M., Achieving High Selectivity for Alkyne Hydrogenation at High Conversions with Compositionally Optimized PdAu Nanoparticle Catalysts in Raspberry Colloid-Templated SiO_2. *ACS Catal.* **2019**, 441-450.

17. Cao, Y.; Chen, B.; Guerrero-Sánchez, J.; Lee, I.; Zhou, X.; Takeuchi, N.; Zaera, F., Controlling Selectivity in Unsaturated Aldehyde Hydrogenation Using Single-Site Alloy Catalysts. *ACS Catal.* **2019,** *9*, 9150-9157.

18. Cao, Y.; Guerrero-Sańchez, J.; Lee, I.; Zhou, X.; Takeuchi, N.; Zaera, F., Kinetic Study of the Hydrogenation of Unsaturated Aldehydes Promoted by CuPtx/SBA-15 Single-Atom Alloy (SAA) Catalysts. *ACS Catalysis* **2020,** *10* (5), 3431-3443.

19. Lucci, F. R.; Marcinkowski, M. D.; Lawton, T. J.; Sykes, E. C. H., H_2 Activation and Spillover on Catalytically Relevant Pt–Cu Single Atom Alloys. *J. Phys. Chem. C* **2015,** *119* (43), 24351-24357.

20. Darby, M. T.; Stamatakis, M.; Michaelides, A.; Sykes, E. C. H., Lonely Atoms with Special Gifts: Breaking Linear Scaling Relationships in Heterogeneous Catalysis with Single-Atom Alloys. *J. Phys. Chem. Lett.* **2018,** *9* (18), 5636-5646.

21. Giannakakis, G.; Flytzani-Stephanopoulos, M.; Sykes, E. C. H., Single-Atom Alloys as a Reductionist Approach to the Rational Design of Heterogeneous Catalysts. *Accounts of Chemical Research* **2019,** *52* (1), 237-247.

22. Darby, M. T.; Réocreux, R.; Sykes, E. C. H.; Michaelides, A.; Stamatakis, M., Elucidating the Stability and Reactivity of Surface Intermediates on Single-Atom Alloy Catalysts. *ACS Catalysis* **2018,** *8* (6), 5038-5050.

23. Thirumalai, H.; Kitchin, J. R., Investigating the Reactivity of Single Atom Alloys Using Density Functional Theory. *Top. Catal.* **2018,** *61* (5), 462-474.

24. Schumann, J.; Bao, Y.; Hannagan, R. T.; Sykes, E. C. H.; Stamatakis, M.; Michaelides, A., Periodic Trends in Adsorption Energies around Single-Atom Alloy Active Sites. *J. Phys. Chem. Lett.* **2021,** *12* (41), 10060-10067.

25. Zafeiratos, S.; Piccinin, S.; Teschner, D., Alloys in catalysis: phase separation and surface segregation phenomena in response to the reactive environment. *Catal. Sci. Technol.* **2012,** *2* (9), 1787-1801.

26. Simonovis, J. P.; Hunt, A.; Palomino, R. M.; Senanayake, S. D.; Waluyo, I., Enhanced Stability of Pt-Cu Single-Atom Alloy Catalysts: In Situ Characterization of the Pt/Cu(111) Surface in an Ambient Pressure of CO. *J. Phys. Chem. C* **2018,** *122* (8), 4488-4495.

27. Papanikolaou, K. G.; Darby, M. T.; Stamatakis, M., CO-Induced Aggregation and Segregation of Highly Dilute Alloys: A Density Functional Theory Study. *J. Phys. Chem. C* **2019,** *123* (14), 9128-9138.

28. Liu, S.; Zhao, Z.-J.; Yang, C.; Zha, S.; Neyman, K. M.; Studt, F.; Gong, J., Adsorption Preference Determines Segregation Direction: A Shortcut to More Realistic Surface Models of Alloy Catalysts. *ACS Catal.* **2019,** *9* (6), 5011-5018.

29. van Spronsen, M. A.; Daunmu, K.; O'Connor, C. R.; Egle, T.; Kersell, H.; Oliver-Meseguer, J.; Salmeron, M. B.; Madix, R. J.; Sautet, P.; Friend, C. M., Dynamics of Surface Alloys: Rearrangement of Pd/Ag(111) Induced by CO and O_2. *J. Phys. Chem. C* **2019,** *123* (13), 8312-8323.

30. Simonovis, J. P.; Hunt, A.; Senanayake, S. D.; Waluyo, I., Subtle and reversible interactions of ambient pressure H_2 with Pt/Cu(111) single-atom alloy surfaces. *Surf. Sci.* **2019,** *679*, 207-213.

31. Tao, F.; Grass, M. E.; Zhang, Y.; Butcher, D. R.; Renzas, J. R.; Liu, Z.; Chung, J. Y.; Mun, B. S.; Salmeron, M.; Somorjai, G. A., Reaction-Driven Restructuring of Rh-Pd and Pt-Pd Core-Shell Nanoparticles. *Science* **2008,** *322* (5903), 932-934.

32. Konuspayeva, Z.; Berhault, G.; Afanasiev, P.; Nguyen, T.-S.; Giorgio, S.; Piccolo, L., Monitoring in situ the colloidal synthesis of AuRh/TiO_2 selective-

hydrogenation nanocatalysts. *Journal of Materials Chemistry A* **2017,** *5* (33), 17360-17367.

33. Carino, E. V.; Crooks, R. M., Characterization of Pt@Cu Core@Shell Dendrimer-Encapsulated Nanoparticles Synthesized by Cu Underpotential Deposition. *Langmuir* **2011,** *27* (7), 4227-4235.

34. Kohler, M. A.; Cant, N. W.; Wainwright, M. S.; Trimm, D. L., Infrared spectroscopic studies of carbon monoxide adsorbed on a series of silica-supported copper catalysts in different oxidation states. *Journal of Catalysis* **1989,** *117* (1), 188-201.

35. Dandekar, A.; Vannice, M. A., Determination of the Dispersion and Surface Oxidation States of Supported Cu Catalysts. *Journal of Catalysis* **1998,** *178* (2), 621-639.

36. Hadjiivanov, K.; Knözinger, H., FTIR study of CO and NO adsorption and coadsorption on a Cu/SiO$_2$ catalyst: Probing the oxidation state of copper. *Phys. Chem. Chem. Phys.* **2001,** *3* (6), 1132-1137.

37. Stacchiola, D. J., Tuning the Properties of Copper-Based Catalysts Based on Molecular in Situ Studies of Model Systems. *Acc. Chem. Res.* **2015,** *48* (7), 2151-2158.

38. Nielsen, N. D.; Smitshuysen, T. E. L.; Damsgaard, C. D.; Jensen, A. D.; Christensen, J. M., Characterization of oxide-supported Cu by infrared measurements on adsorbed CO. *Surface Science* **2021,** *703*, 121725.

39. Han, T.; Lee, I.; Cao, Y.; Zhou, X.; Zaera, F., Thermodynamics of Carbon Monoxide Adsorption on Cu/SBA-15 Catalysts: Under Vacuum versus under Atmospheric Pressures. *The Journal of Physical Chemistry C* **2022,** *126* (6), 3078-3086.

40. Shigeishi, R. A.; King, D. A., Chemisorption of Carbon Monoxide on Platinum {111}: Reflection-Absorption Infrared Spectroscopy. *Surf. Sci.* **1976,** *58*, 379.

41. Martin, R.; Gardner, P.; Bradshaw, A. M., The adsorbate-induced removal of the Pt{100} surface reconstruction. Part II: CO. *Surf. Sci.* **1995,** *342* (1–3), 69-84.

42. Zaera, F.; Liu, J.; Xu, M., Isothermal study of the kinetics of carbon monoxide oxidation on Pt(111): Rate dependence on surface coverages. *J. Chem. Phys.* **1997,** *106* (10), 4204-4215.

43. Kappers, M. J.; van der Maas, J. H., Correlation between CO frequency and Pt coordination number. A DRIFT study on supported Pt catalysts. *Catal. Lett.* **1991,** *10* (5-6), 365-373.

44. Liu, J.; Lucci, F. R.; Yang, M.; Lee, S.; Marcinkowski, M. D.; Therrien, A. J.; Williams, C. T.; Sykes, E. C. H.; Flytzani-Stephanopoulos, M., Tackling CO Poisoning with Single-Atom Alloy Catalysts. *Journal of the American Chemical Society* **2016,** *138* (20), 6396-6399.

45. Finzel, J.; Christopher, P., Dynamic Pt Coordination in Dilute AgPt Alloy Nanoparticle Catalysts Under Reactive Environments. *Top. Catal.* **2022**, DOI: 10.1007/s11244-021-01545-7.

46. Campbell, C. T.; Ertl, G.; Kuipers, H.; Segner, J., A molecular beam investigation of the interactions of CO with a Pt(111) surface. *Surf. Sci.* **1981,** *107* (1), 207-219.

47. Gland, J. L.; Kollin, E. B., Carbon Monoxide Oxidation on the Pt(111) Surface: Temperature Programmed Reaction of Coadsorbed Atomic Oxygen and Carbon Monoxide. *J. Chem. Phys.* **1983,** *78,* 963-974.

48. Tränkenschuh, B.; Papp, C.; Fuhrmann, T.; Denecke, R.; Steinrück, H. P., The dissimilar twins - a comparative, site-selective in situ study of CO adsorption and desorption on Pt(322) and Pt(355). *Surf. Sci.* **2007,** *601* (4), 1108-1117.

49. Hayden, B. E.; Bradshaw, A. M., The adsorption of CO on Pt(111) studied by infrared reflection—Absortion spectroscopy. *Surf. Sci.* **1983,** *125* (3), 787-802.

50. Hayden, B. E.; Kretzschmar, K.; Bradshaw, A. M.; Greenler, R. G., An infrared study of the adsorption of CO on a stepped platinum surface. *Surf. Sci.* **1985,** *149* (2-3), 394-406.

51. Rodriguez, J. A.; Truong, C. M.; Goodman, D. W., Infrared vibrational studies of CO adsorption on Cu/Pt(111) and CuPt(111) surfaces. *J. Chem. Phys.* **1992,** *96* (10), 7814-7825.

52. Baró, A. M.; Ibach, H.; Bruchmann, H. D., Vibrational modes of hydrogen adsorbed on Pt(111): Adsorption site and excitation mechanism. *Surf. Sci.* **1979,** *88* (2–3), 384-398.

53. Bădescu, Ş. C.; Salo, P.; Ala-Nissila, T.; Ying, S. C.; Jacobi, K.; Wang, Y.; Bedürftig, K.; Ertl, G., Energetics and Vibrational States for Hydrogen on Pt(111). *Phys. Rev. Lett.* **2002,** *88* (13), 136101.

54. Asada, H.; Toya, T.; Motohashi, H.; Sakamoto, M.; Hamaguchi, Y., Study of hydrogen adsorbed on platinum by neutron inelastic scattering spectroscopy. *J. Chem. Phys.* **1975,** *63* (9), 4078-4079.

55. Renouprez, A. J.; Jobic, H., Neutron scattering study of hydrogen adsorption on platinum catalysts. *J. Catal.* **1988,** *113* (2), 509-516.

56. Parker, S. F.; Mukhopadhyay, S.; Jiménez-Ruiz, M.; Albers, P. W., Adsorbed States of Hydrogen on Platinum: A New Perspective. *Chem. Eur. J.* **2019,** *25* (26), 6496-6499.

57. Meitzner, G.; Via, G. H.; Lytle, F. W.; Sinfelt, J. H., Structure of bimetallic clusters. Extended x‐ray absorption fine structure (EXAFS) studies of Re–Cu, Ir–Cu, and Pt–Cu clusters. *J. Chem. Phys.* **1985,** *83* (1), 353-360.

58. Irani, R. S.; Cahn, R. W., A Classical Phase Transformation: Order—Disorder in CuPt. *Nature* **1970,** *226* (5250), 1045-1046.

59. Abe, T.; Sundman, B.; Onodera, H., Thermodynamic assessment of the Cu−Pt system. *Journal of Phase Equilibria and Diffusion* **2006,** *27* (1), 5-13.

60. Liu, Y.; Zhang, L.; Yu, D., Diffusion Mobilities in fcc Cu-Au and fcc Cu-Pt Alloys. *Journal of Phase Equilibria and Diffusion* **2009,** *30* (2), 136-145.

61. Tang, J.; Deng, L.; Xiao, S.; Deng, H.; Zhang, X.; Hu, W., Chemical Ordering and Surface Segregation in Cu–Pt Nanoalloys: The Synergetic Roles in the Formation of Multishell Structures. *J. Phys. Chem. C* **2015,** *119* (37), 21515-21527.

62. Vega, L.; Aleksandrov, H. A.; Farris, R.; Bruix, A.; Viñes, F.; Neyman, K. M., Chemical ordering in Pt–Au, Pt–Ag and Pt–Cu nanoparticles from density functional calculations using a topological approach. *Materials Advances* **2021,** *2* (20), 6589-6602.

63. Therrien, A. J.; Hensley, A. J. R.; Marcinkowski, M. D.; Zhang, R.; Lucci, F. R.; Coughlin, B.; Schilling, A. C.; McEwen, J.-S.; Sykes, E. C. H., An atomic-scale view of single-site Pt catalysis for low-temperature CO oxidation. *Nat. Catal.* **2018,** *1* (3), 192-198.

Chapter 4 Oxidation State of Copper in Cu-Pt Single-Atom Catalysts under Hydrogenation Conditions

In this chapter and Chapter 5, the oxidation state of copper in Cu-Pt single-atom alloy catalysts was analyzed. Copper catalysts are widely used in various applications, to promote the hydrogenation of carbon monoxide and the low-temperature water-shift reaction, among other processes. In combination with a second metal, in so-called single-atom alloy catalysis, it can also help in the selective hydrogenation of organic reactants with multiple double and triple bonds. In all these reducing processes, it is reasonable to expect the active catalyst to be metallic copper. However, data from *in situ* x-ray absorption in Section 4.2 and infrared spectroscopy experiments in Section 5.1108 have indicated that copper nanoparticles dispersed on silica supports sometimes develop a thin copper oxide film at low temperatures, below approximately 450 K, even in the presence of a hydrogen atmosphere. Full reduction to the metallic state does occur at higher temperatures, and the interconversion is reversible. On the other hand, more recent XAS results indicated that oxidation for Cu/SBA-15 and $CuPt_{0.05}$/SBA-15 under H_2 atmosphere may be avoided, in contrast with what had been seen before. In light of these findings, it may be concluded that copper oxidation may occur under some circumstances, even in reducing environments, even if those circumstances have not been fully identified yet. The important information derived from these studies is that, given that much hydrogenation catalysis is conducted under mild conditions, it is possible that such oxidation may take place on oxidized copper sites. Possible reasons for this metal nanoparticle oxidation under reducing conditions are discussed.

4.1 Introduction

Coinage metals (Cu, Ag, Au) are known for their general unreactivity, but over the years have been found multiple uses in heterogeneous catalysis. Gold, a metal that is practically inert in bulk form, has shown to promote a number of reactions in nanoparticle (NP) form, including selectives,[1-3] acetylene hydrochlorination,[4] and other organic transformations,[5-8] as well as processes related to environmental remediation.[9-10] Silver has long been used for the epoxidation of olefins.[11-14] Copper is perhaps the most versatile of the three, being the main element in catalysts for the low-temperature water-shift reaction,[15-17] and for CO hydrogenation[18-22] processes, among others. When investing coinage-base catalysts, the question often arises regarding the oxidation state of the active sites. Chemical intuition suggests that cationic species may be present, and perhaps participate, in oxidation reactions, whereas metallic sites are expected in catalytic reductions. However, *ex situ* X-ray photoelectron spectroscopy (XPS) data from studies on the selective hydrogenation of unsaturated aldehydes using $CuPt_x$-based single-atom alloy (SAA) catalysts recently indicated that, counterintuitively, the Cu NPs in that case may be partially oxidized.[23] Here, we report results from *in situ* spectroscopic studies confirming that, in some cases, such metal NPs are covered with a thin layer of copper oxide at the low temperatures used in most hydrogenation catalysis, even though the reaction environment consists mainly of H_2 gas. These results have not been fully reproduced, however, and more experiments will be needed to better understand the conditions under which the catalyst becomes oxidized.

4.2 Discussion of XAS Analysis of Cu-Pt Catalysts

The surface of solid Cu readily oxidizes when exposed to air, and the copper in Cu-based catalysts usually start as copper oxides. On the other hand, such catalysts are relatively easy to reduce to their metallic state through pretreatment with H_2 or other reducing agents.[24-27] The *ex situ* XPS data provided in Figure 4-1 clearly corroborate this conversion for the case of the 5 wt% $CuPt_x$/SBA-15 SAA samples previously shown by us to promote the selective hydrogenation of unsaturated aldehydes,[23, 28] the same catalysts used in this study. Data are shown for two catalysts, one with pure Cu nanoparticles (Cu/SBA-15) and the other containing a 0.05 molar fraction of Pt ($CuPt_{0.05}$/SBA-15). The left panel shows the Cu 2p XPS traces obtained before ("As Prepared", blue traces) and after ("After Reduction", red traces) pretreatment with hydrogen gas (500 Torr H_2 at 625 K for 3 h, after which the sample was immediately transferred to the XPS spectrometer with minimum –less than 1 min– exposure to air), whereas the right panel displays the corresponding Cu L_3VV Auger electron spectroscopy (AES) spectra. The fact that the Cu NPs in the original catalysts are oxidized to CuO (possibly mixed with some $CuSiO_3$) is clearly indicated by the high binding energies Cu 2p peaks seen at BE(Cu $2p_{3/2}$) = 933.2 and 935.5 eV with both the Cu/SBA-15 and the $CuPt_{0.05}$/SBA-15 catalysts (the reported BE for Cu_2O is 932.2 eV),[29] by the broad shakeup features observed at about $\Delta E \sim 10$ eV higher energies, and by the KE = 914.5 eV peak seen for the Cu L_3VV AES feature. On the other hand, the spectra recorded after catalyst reduction shows a sharp Cu $2p_{3/2}$ peak at BE = 932.4 eV characteristic of metallic Cu. This reduction of the initial NPs to metallic Cu upon H_2 exposure at high temperatures was seen with all the catalysts studied regardless of the amount of Pt incorporated in the SAA (although Pt seems to facilitate the reduction, allowing for the transition to occur at lower temperatures).[28]

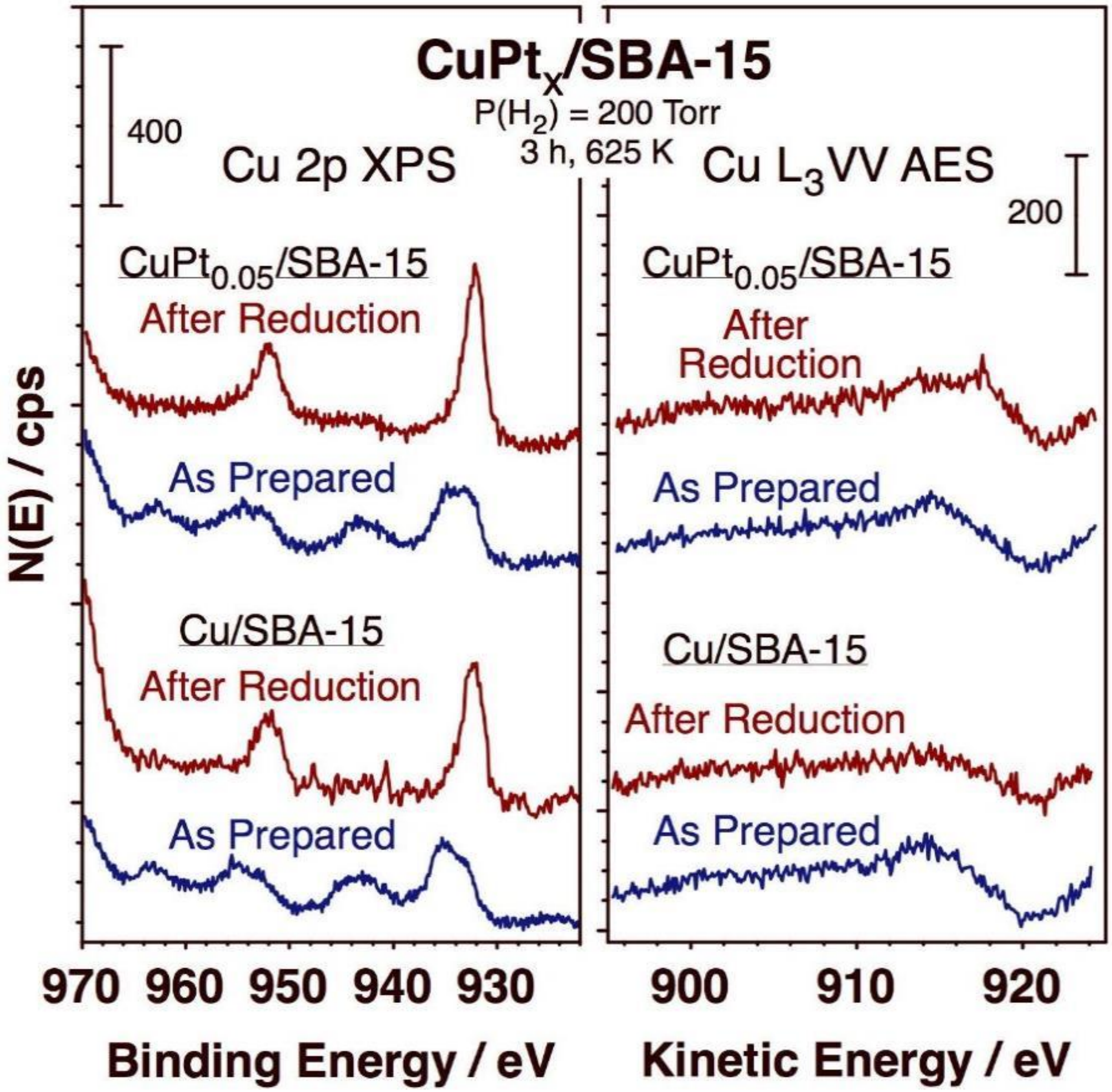

Figure 4-1. Ex situ Cu 2p XPS and Cu L$_3$VV AES data for pure Cu/SBA-15 and for CuPt$_{0.05}$/SBA-15 catalysts obtained before and after reduction pretreatments (exposure to 500 Torr of H$_2$ at 625 K for 3 h).

Although the activated catalysts (i.e., after H_2 pretreatment) contain copper in their metallic state, it is possible for their surfaces to be further affected by the gases present during catalysis; partial oxidation may occur at that stage, as previously suggested.[23] This possibility was probed here by using *in situ* X-ray absorption spectroscopy (XAS) at three different synchrotron facilities. An example of the data obtained near the Cu K-edge (using beamline 8-ID of the National Synchrotron Light Source-II –NSLS-II– at Brookhaven National Laboratory) is provided in Figure 4-5, for a 5 wt% $CuPt_{0.05}$/SBA-15 catalyst (which consists of Cu metal nanoparticles (NPs) of <d> = 4.3 nm average diameter alloyed with 5 atom% Pt and dispersed on a SBA-15 mesoporous silica support, Figure 4-2 and Figure 4-3 exposed to a flowing atmosphere of pure H_2: the left panel provides X-ray absorption near edge spectra (XANES) recorded as the catalyst was heated from room temperature (300 K) to 495 K and back, whereas the right panel displays data for reference solids (CuO, Cu_2O, and metallic Cu) as well as the best fits of the 300 and 495 K traces to linear combinations of those for metallic and oxidized copper (the results from fits to all of the spectra are provided in Figure 4-4.)

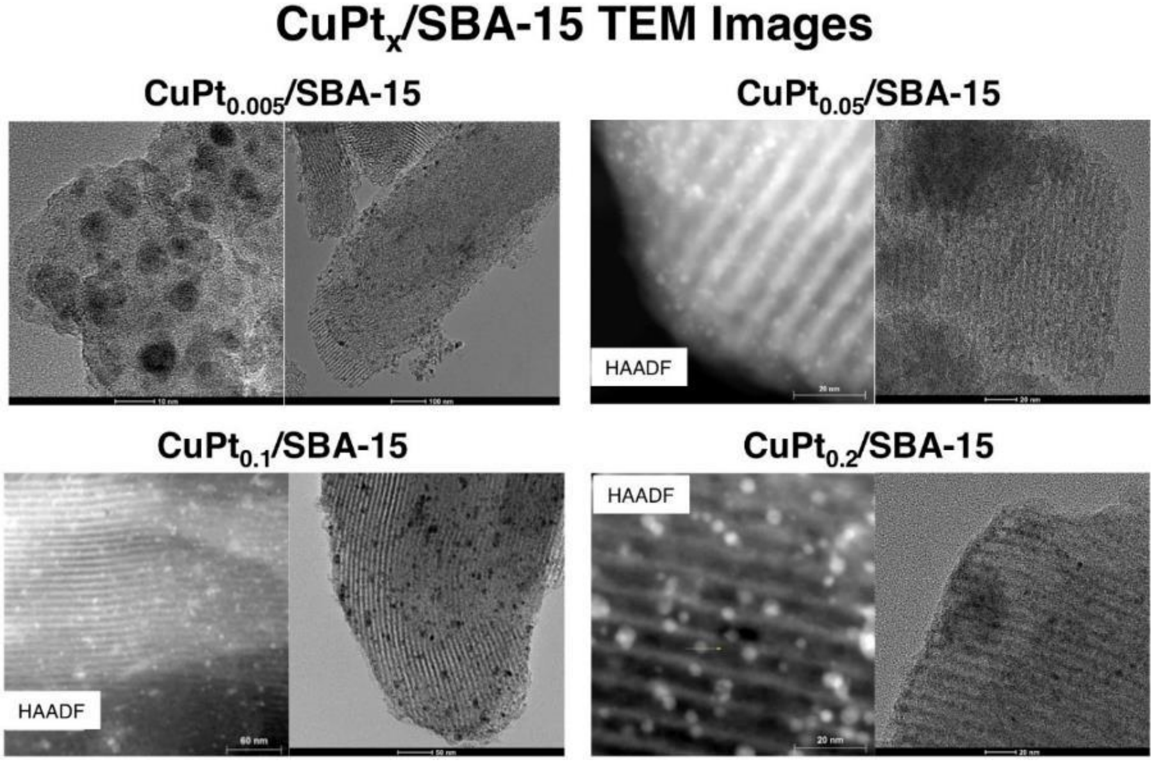

Figure 4-2. Regular and high-angle annular dark-field (HAADF) scanning transmission electron microscopy (STEM) images of the CuPt$_x$/SBA-15 catalysts used in this study, as a function of x (Pt molar fraction). The Cu metal load in all catalysts was 5 wt%.

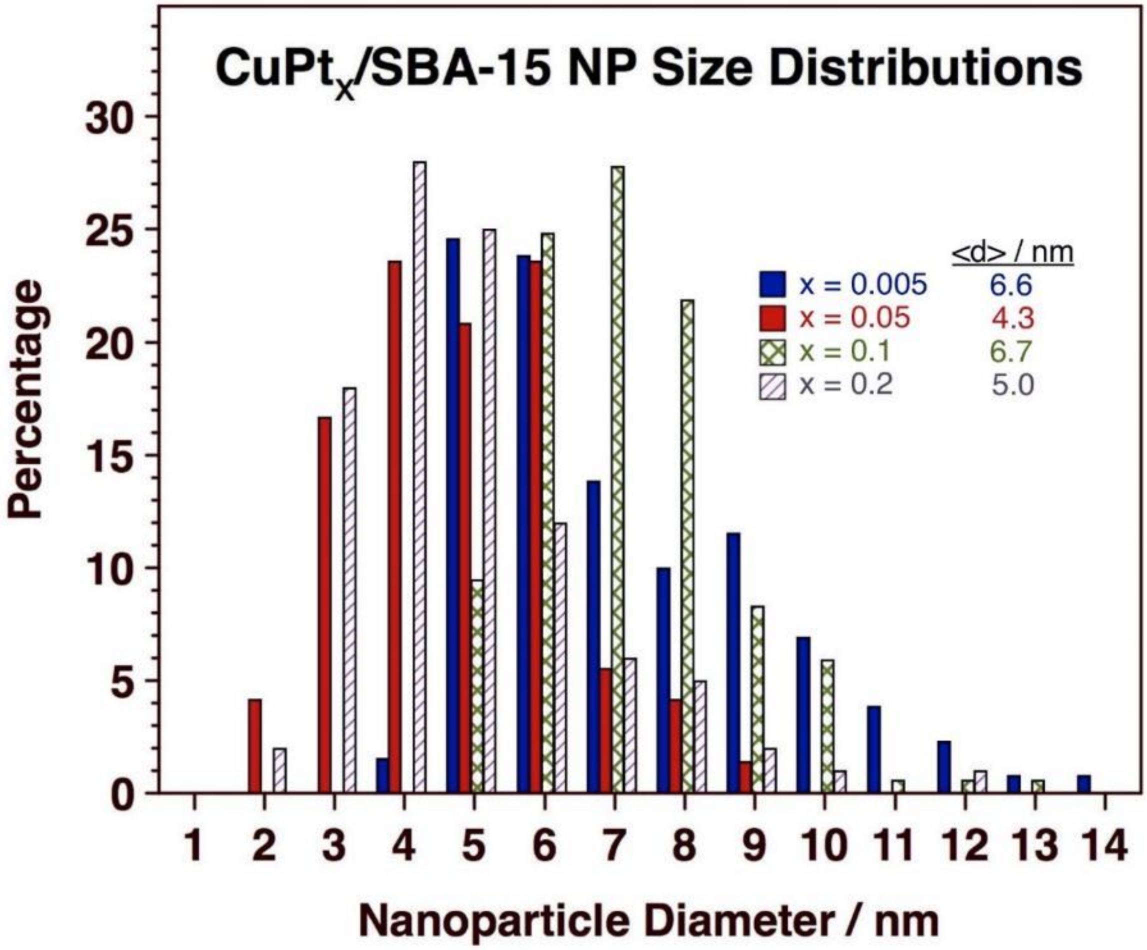

Figure 4-3. Nanoparticle (NP) size distributions and average NP sizes for the CuPt$_x$/SBA-15 catalysts used in this study, as a function of x (Pt molar fraction). The Cu metal load in all catalysts was 5 wt%.

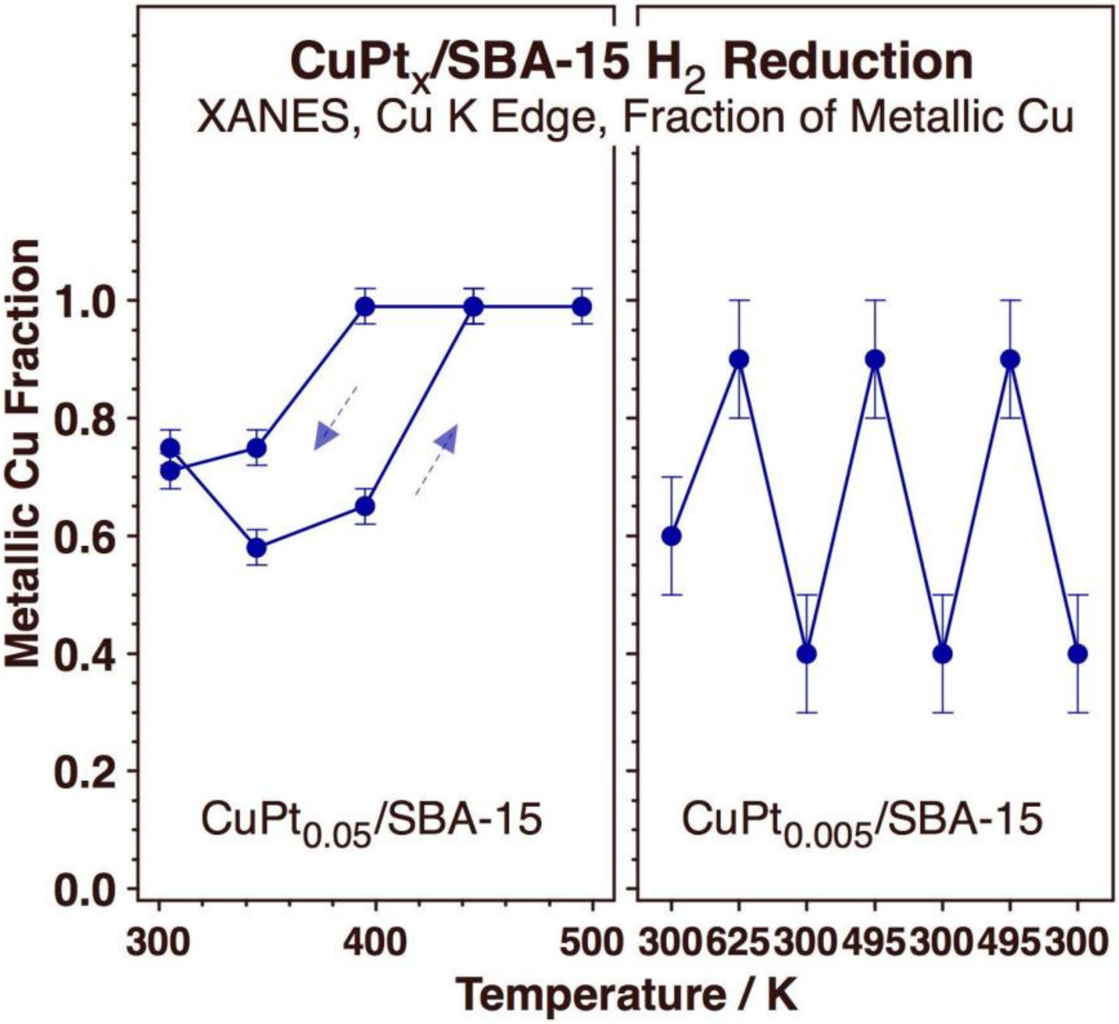

Figure 4-4. Fraction of metallic Cu in the CuPt$_x$ NPs of CuPt$_{0.05}$/SBA-15 (left panel) and CuPt$_{0.005}$/SBA-15 (right) as a function of temperature while exposed to a H_2 atmosphere, as estimated from best-linear-combination fits of the XANES data in Figure 4-5 and Figure 4-6 to the Cu metal and Cu_2O reference data.

The Cu in the initial sample, which was pre-reduced in a H_2 atmosphere at 625 K for 3 h, is mainly in metallic form, the same as in the *ex situ* experiments reported in Figure 4-1: compare the first (bottom) trace in Figure 4-5-left with the metallic Cu data in Figure 4-5-right. However, the Cu K-edge XANES spectra changes significantly after continuous exposure of the catalyst to a flowing H_2 gas environment, as manifested by the next trace shown in Figure 4-5-left, obtained at 345 K. Several changes are evident there, in particular the washing out of the features for photon energies above 9000 eV as well as a slight sharpening and blueshift of the peak at 8984 eV. A similar spectrum was acquired after heating to 395 K, but by 445 K the original features reappear. Those are preserved at 495 K, but reversibly disappear again upon cooling down under the same H_2 atmosphere. By comparison with the reference spectra in Figure 4-5-right, it was concluded that the low-temperature data exhibit a significant component from partially oxidized Cu, most likely from a surface Cu_2O film, which is reduced at higher temperatures. Fitting of the data suggests a reversible conversion in the Cu NPs from ~30-40% Cu_2O at room temperature to almost fully metallic Cu at 495 K (Figure 4-5-right, thick dotted lines, and Figure 4-4-left). These are approximate values: the fits do not account for all the spectral features, possibly because of the presence of additional Cu_2O-Cu, and even Cu/SiO_2, interfacial states in our catalysts. Nevertheless, the reduction of the metal nanoparticles at high temperatures is quite evident by simple observation of the spectra, as is the reversible nature of the conversion and the re-oxidation at low temperatures. Given that in our catalysts the average NP size is <d> ~ 4.3 nm, it is estimated that the Cu_2O surface layer in the low-temperature limit may be approximately 0.7 nm in thickness. It is important to highlight the fact that there is a kinetic limitation to these conversions, as manifested by the hysteresis seen in the data in Figure 4-4-left: given that the time interval between consecutive data points was approximately 40 minutes, it would appear that it may take on the order of an hour for the Cu to become oxidized or get reduced back to its metallic state at temperatures around 400 K.

The reversibility of this redox behavior was further corroborated by performing repeated heating and cooling cycles on$CuPt_{0.005}$/SBA-15. Figure 4-6 shows typical *in situ* Cu K-edge XANES data obtained from such experiments (at the Advanced Photon Source – APS– of Argonne National Laboratory), in this case for a $CuPt_{0.005}$/SBA-15 catalyst (Cu NPs containing 0.5 atom% Pt) cycled twice between 300 and 495 K after initial reduction at 625 K (the fresh catalyst, right after synthesis, displays a spectrum assignable to CuO, bottom trace in the $CuPt_{0.005}$/SBA-15 set in Figure 4-6). Similar transitions to those reported for $CuPt_{0.05}$/SBA-15 in Figure 4-5 are observed here, with a significant component due to Cu_2O (about 40%) seen at 300 K and mainly metallic Cu (> 90%) detected at 495 K. The results from linear-combination fits of these data to the reference spectra are summarized in Figure 4-4-right.

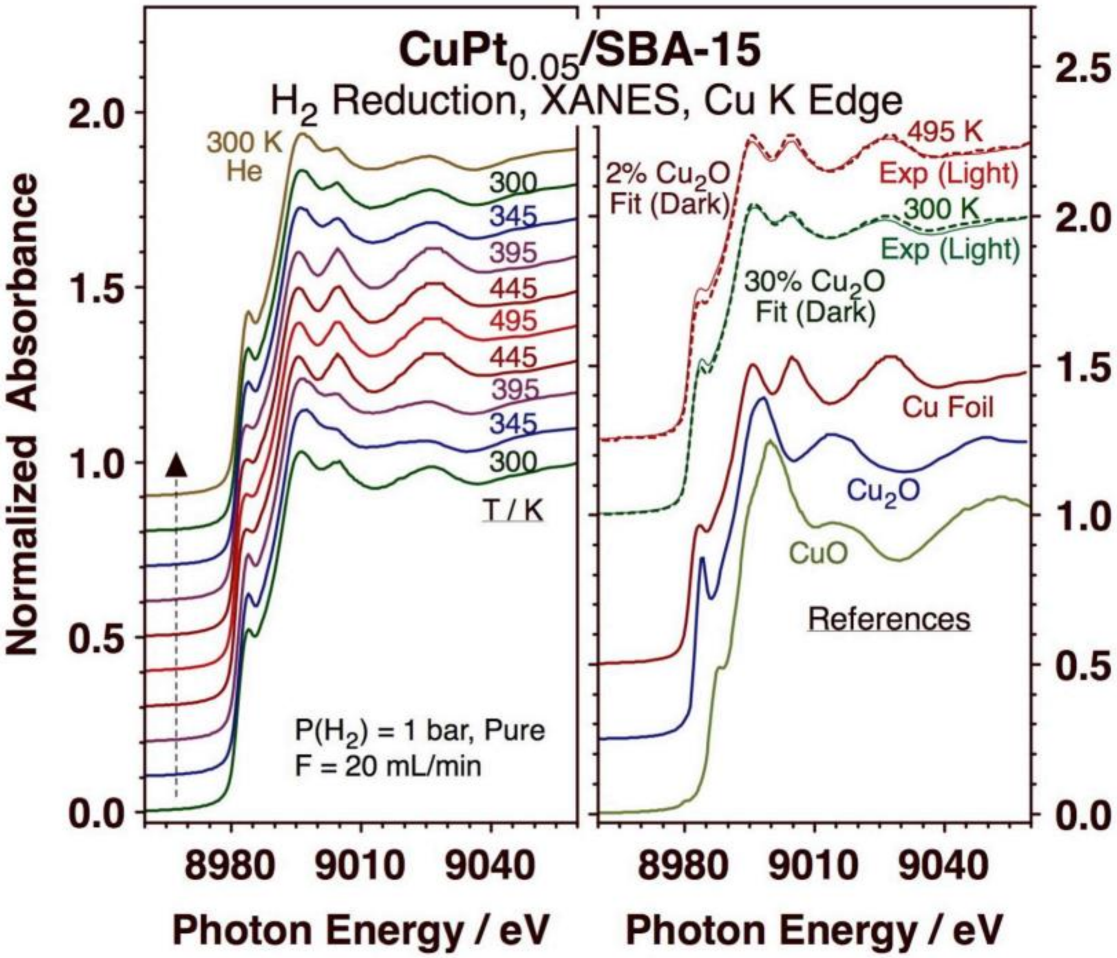

Figure 4-5. Left: in situ Cu K-edge XANES spectra for a $CuPt_{0.05}$/SBA-15 catalyst as a function of temperature while under 1 bar of flowing H_2 gas. The temperature was cycled between 300 and 495 K and back while recording spectra in 50 K intervals. Center: Reference data for CuO, Cu_2O, and a metallic Cu foil, together with data for the $CuPt_{0.05}$/SBA-15 catalyst at the extreme temperatures, 300 and 495 K. The experimental spectra (solid thin lines) are contrasted with fits based on linear combinations of the traces for Cu and Cu_2O (thick dotted lines); the total Cu_2O:Cu composition ratios were estimated to be 30:70 and 2:98 for the low- and high-temperatures, respectively. Right: Summary of the linear combination fitting of all the data in the left panel, in the form of the fraction of Cu in metallic form.

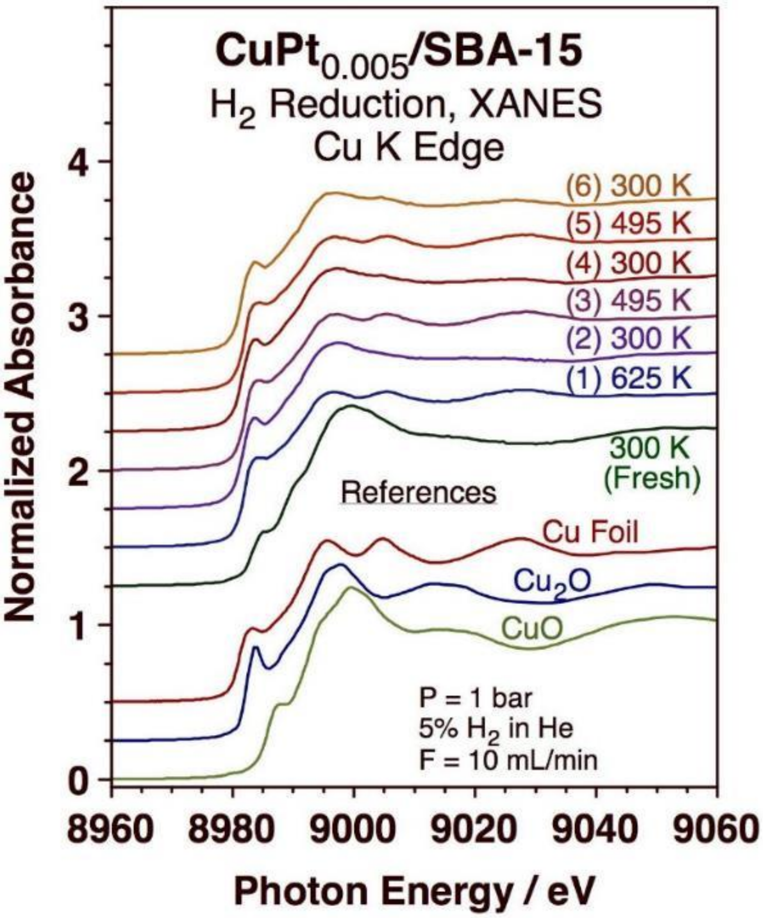

Figure 4-6. *In situ* Cu K-edge XANES spectra for a $CuPt_{0.005}$/SBA-15 catalyst, obtained as the temperature was cycled twice between 300 and 495 K, all in the presence of 1 bar of a flowing mixture of 5 vol% H_2 in He. Similar reference spectra as in Figure 4-5 are provided for comparison.

Additional corroborating evidence of the reversible redox chemistry reported above was obtained from analysis of the corresponding *in situ* Cu K-edge extended X-ray absorption fine structure (EXAFS) spectra. Figure 4-7 displays data from the temperature cycling experiments in H_2 with the $CuPt_{0.005}$/SBA-15 catalyst associated with the XANES in Figure 4-6. The spectral changes induced by the temperature cycling are already evident in k space (Figure 4-7-left panel): notice in particular the development of a new oscillation at k ~ 7.2 $Å^{-1}$ in the low-temperature traces, a feature that is significantly reduced in amplitude when the catalyst is heated up. The catalyst changes are better visualized in the radial distribution plots (Figure 4-7-right). For one, a detectable feature grows at R ~ 1.5 Å every time the catalyst is treated in H_2 at 300 K; this peak is associated with the Cu–O bond distance in the copper oxide component, which, on the basis of the IR data presented below, we ascribe to a surface film. Heating to higher (495 K) temperatures leads to the virtual elimination of that signal, and to the enhancement of new features around R = 3.4 and 4.1 Å as well as an increase in the intensity of the main Cu–Cu peak at R ~ 2.2 Å. All this suggests the reduction of the Cu_2O surface layer and an increase in the radius of the metallic Cu component of the catalyst NPs.

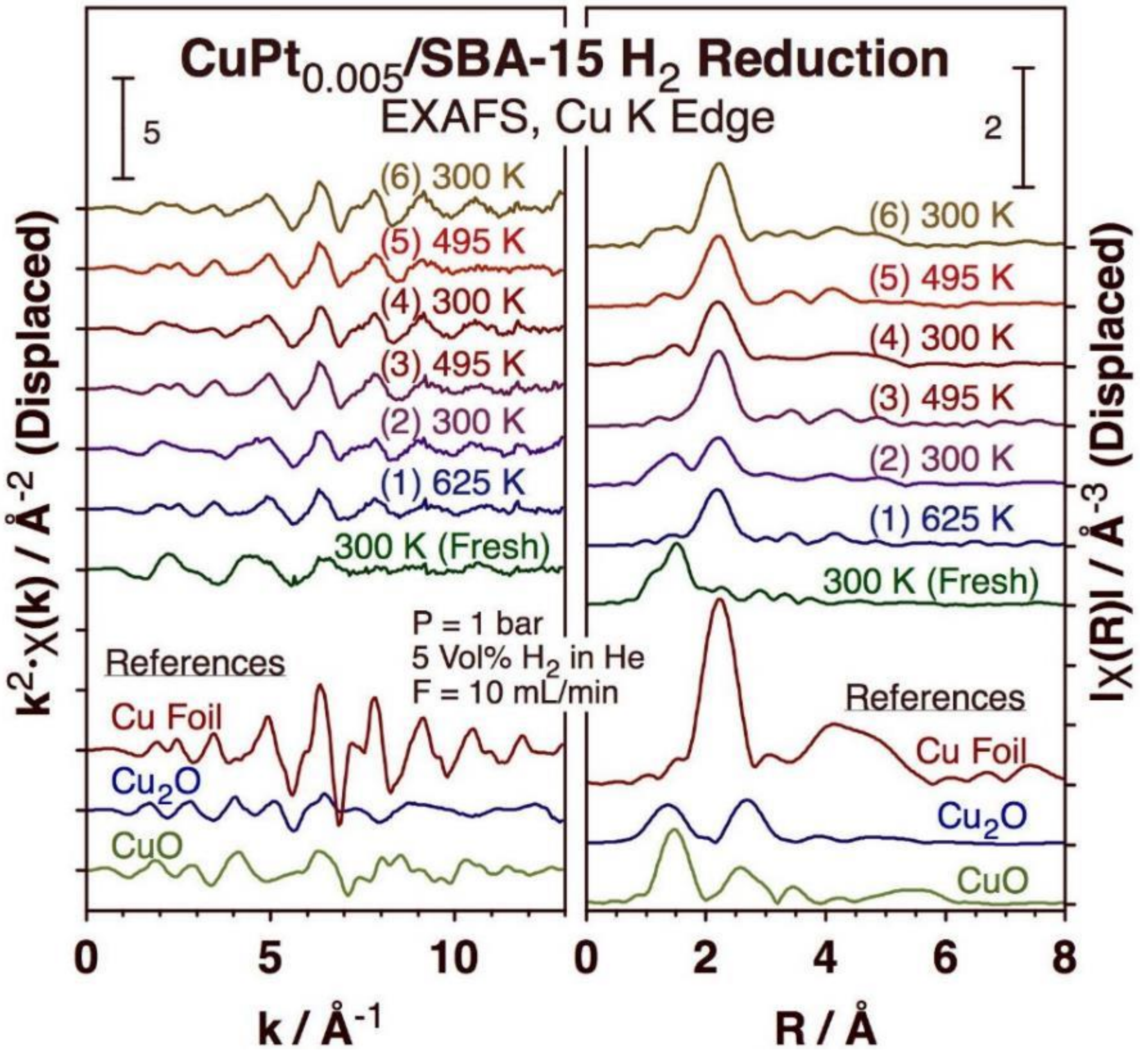

Figure 4-7. *In situ* Cu K-edge EXAFS spectra for a $CuPt_{0.005}$/SBA-15 catalyst acquired during a two-times temperature cycling experiment between 300 and 495 K, all in the presence of 1 bar of a flowing 5 vol% H_2: 95 vol% He mixture. The data are reported as a function of both k (left panel) and magnitude of the Fourier transform R (right).

Modelings of the Cu K-edge EXAFS data provided quantitative support for the qualitative interpretation discussed above. Figure 4-8 summarizes some of the key values obtained from fitting of the raw data in terms of coordination numbers (CNs) and bond distances. The left panel shows the evolution of the Cu–Cu and Cu–O CNs for the $CuPt_{0.05}$/SBA-15 catalyst under a 1 bar of H_2 as the temperature was cycled from 300 to 495 K and back in 50 K increments. The Cu NPs in the initial catalyst, at 300 K, have an average Cu CN of 6, in addition to approximately one O neighbor (on average; the actual number is below that one). However, upon raising the temperature to 445 K or above, the Cu–Cu CN increases to approximately 9, and no Cu–O bonding is detected. This process is reversible, albeit with a hysteresis (indicated when discussing the XANES data in Figure 4-5), an observation that points to slow kinetics around 400 K. The low CNs seen here are explained by the small dimensions of the metal NPs, as they are not corrected by the fraction of Cu in the oxide shell. Assuming a Cu@Cu_2O core-shell nanostructure, using published estimates of Cu–Cu average CNs truncated cuboctahedral particles,[30] and the NP average diameters measure by TEM from Figure 4-2, the CN numbers reported in Figure 4-8 (CN ~ 6 and 9.5 for the low and high temperatures, respectively) are estimated to correspond to Cu_2O shells of ~0.7 and <0.1 nm in thickness, respectively. The CNs trend for the $CuPt_{0.005}$/SBA-15 sample qualitatively mimics that of the $CuPt_{0.05}$/SBA-15 catalyst, but the actual values are systematically lower; this is explained by a self-absorption effect in the former sample, which was measured using fluorescence detection (the $CuPt_{0.05}$/SBA-15 catalyst was measured in transmission mode).

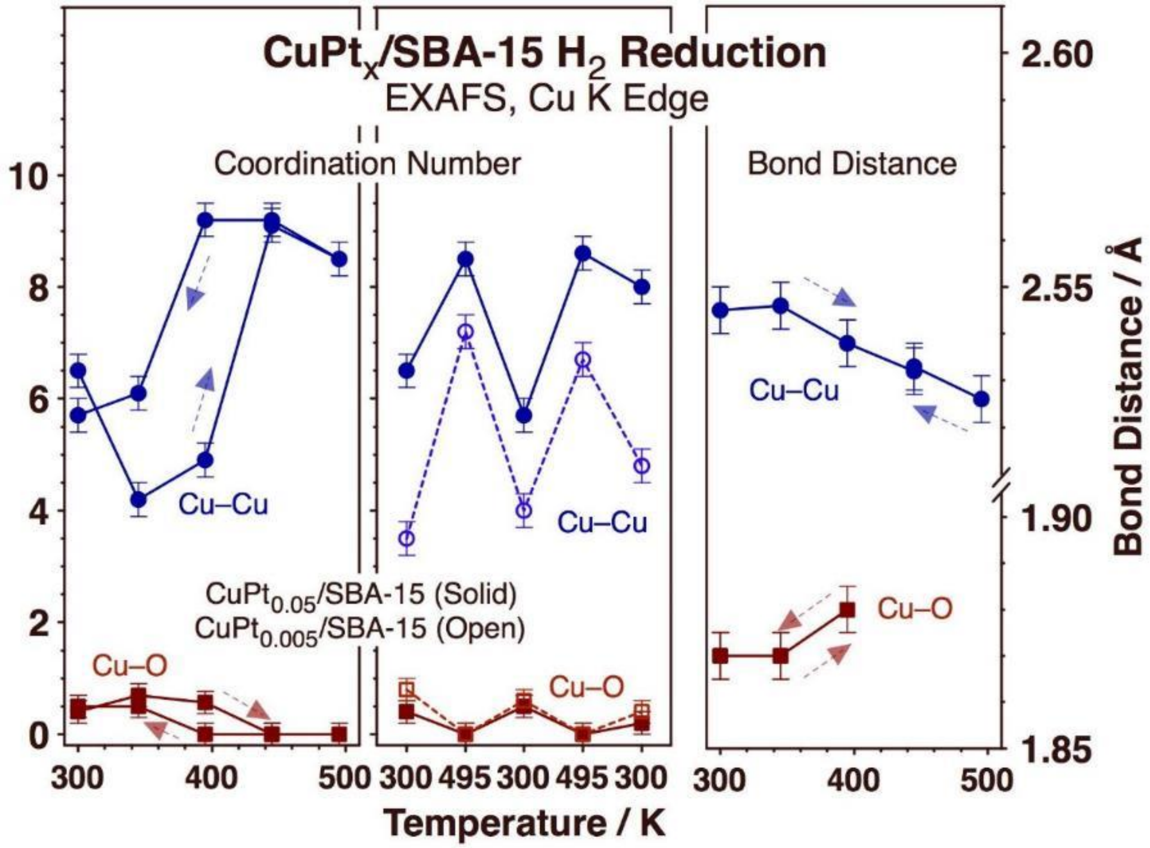

Figure 4-8. CNs and bond distances for the CuPt$_{0.005}$/SBA-15 (light colors and open symbols in middle panel) and CuPt$_{0.05}$/SBA-15 (dark colors and filled symbols in all three panels) catalysts estimated by fitting the *in situ* Cu K-edge EXAFS spectra acquired during temperature cycling between 300 and 495 K in the presence of a H_2 atmosphere. Left: Cu–Cu and Cu–O CN data for the CuPt$_{0.05}$/SBA-15 sample measured during a one-time temperature cycle from 300 K to 495 K and back in 50 K intervals. Center: Cu–Cu and Cu–O CN data for both catalysts acquired during two consecutive 300 - 495 - 300 K heating-cooling cycles. Right: Cu–Cu and Cu–O bond distances for the same experiments as those in the left panel.

The data in Figure 4-8-center, which correspond to the CNs determined from Cu K-edge EXAFS data for two catalysts with different Pt content ($CuPt_{0.005}$/SBA-15 and $CuPt_{0.05}$/SBA-15) and for two 300 - 495 - 300 K temperature cycles, attest to the reversibility of the redox changes. Similar qualitative behavior is seen with both catalysts, although lower CNs were estimated for the $CuPt_{0.005}$/SBA-15 catalysts, likely a reflection of small differences in average NP size. Finally, the data in Figure 4-8-right are the bond distances associated with the experiments reported in Figure 4-8-left. Interestingly, a contraction of the Cu–Cu bond (and a slight elongation of the Cu–O bond) is seen upon the reduction seen at high temperatures, by approximately 0.02 Å. This is explained again by the small size of the NPs: the Cu–Cu bond distances are well known to decrease with decreasing NP size.[31]

Cu surface oxidation was also seen during the catalytic hydrogenation of crotonaldehyde. Figure 4-9 shows *in situ* Cu K-edge XANES data for the $CuPt_{0.005}$/SBA-15 catalyst acquired during the hydrogenation of crotonaldehyde with gas-phase H_2 (at the Stanford Synchrotron Radiation Light source –SSRL– of the Stanford Linear Accelerator Center). As in the studies reported above, the initial catalyst, before pretreatment, was fully oxidized (in CuO form; Figure 4-9, bottom trace) but could be reduced following a high-temperature (625 K) H_2 treatment (Figure 4-9, second-from-bottom trace). Some partial re-oxidation takes place during the hydrogenation of the unsaturated aldehyde: the Cu K-edge XANES spectrum recorded under steady-state conditions, at both 375 K (Figure 4-9-third from top) and 345 K (Figure 4-9-top) resemble more closely those reported in

Figure 4-5 below 395 K, which we already established reflect the formation of a Cu_2O surface film on the Cu NPs. The catalyst could be fully reduced even at 375 K after reaction, in pure H_2 (Figure 4-9-second from top), and the oxidation is less extensive during catalysis at the lower temperature, suggesting that crotonaldehyde adsorption may inhibit the uptake of hydrogen on the surface and with that its reduction. Previous kinetic studies of this reaction with the same catalyst already suggested that this may be the case.[23, 28]

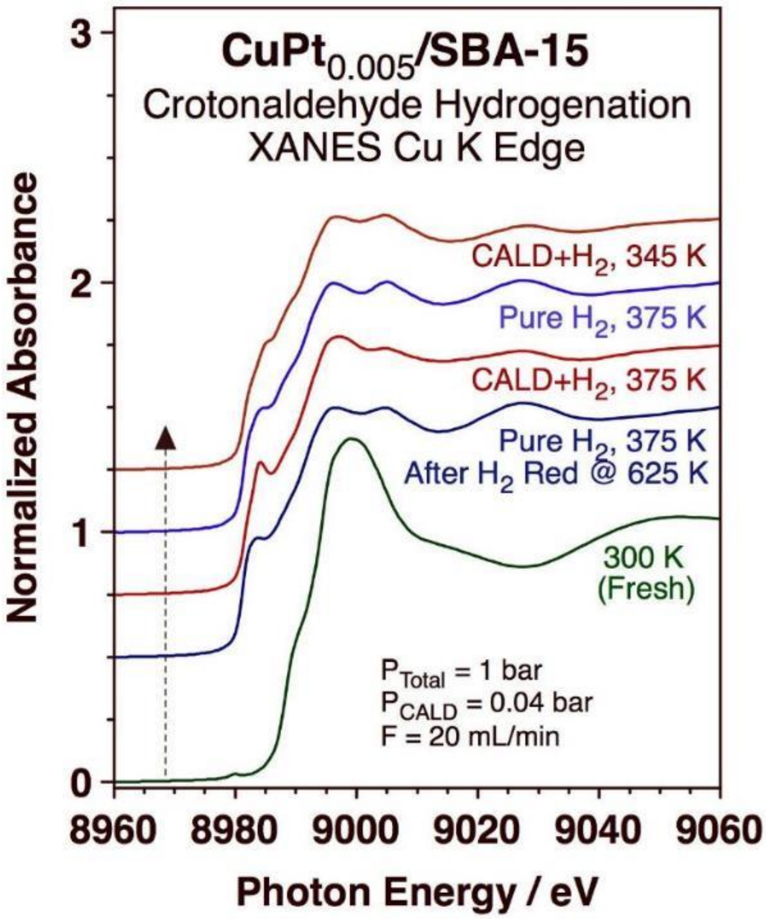

Figure 4-9. Cu K-edge XANES spectra for a $CuPt_{0.005}$/SBA-15 catalyst, obtained *in situ* during the catalytic hydrogenation of crotonaldehyde. Shown are the traces for, from bottom to top: (1) the fresh catalyst; (2) at 375 K under a flowing atmosphere of pure H_2, after 3 h reduction in H_2 at 625 K; (3) during the steady-state catalytic hydrogenation of crotonaldehyde (P_{CALD} = 0.04 bar) at 375 K; (4) after reaction, under pure H_2 at 375 K; and (5) during the steady-state catalytic hydrogenation of crotonaldehyde (P_{CALD} = 0.04 bar) at 345 K.

4.3 Further XAS Experiments on Cu/SBA-15 and $CuPt_{0.05}$/SBA-15

In order to further investigate the mechanism of the oxidation for Cu, in situ Cu K edge XANES was obtained at the Advanced Photon Source (APS). Several conclusions were made based on the analyzed data.

4.3.1 XAS Result of Cu/SBA-15

Firstly, an in situ XAS experiment was performed on Cu/SBA-15. During this part, the catalyst was pre-treated with H_2 flow and reduced. After that, experiment was performed as shown in Figure 4-10. In this figure, Cu K edge data of Cu/SBA-15 were obtained while the catalyst was exposed to H_2 under 623 K and 290 K shown in blue and red trace, respectively. However, the new results indicate that Cu was not oxidized after cooling down to RT under H_2 flow, which seems inconsistent with our conclusion from 4.2. To repeat the oxidation of Cu as we found previously, a small amount of O_2 was then introduced in the H_2 flow as the form of O_2/He on purpose, the results are shown in Figure 4-11. A sequence of treatments was tested, described in Figure 4-11 as steps. To start with, the trace of step 13 indicates that initially Cu was in metallic state. After adding 1 ml/min of O_2/He into the gas mixture, Cu seems to become oxidized in the 1st scan, indicated by the increase of the absorption edge, which is usually referred as the white line, but it was then quickly reduced with the aid of H_2, as we can see from the 2nd scan. Since it would appear that the addition of 1 ml/min of O_2/He to the gas stream was insufficient to sustain catalyst oxidation, that was increased to 5 ml/min in step 15. It should be noted that the absorption edge changed since additional O_2/He was introduced to the flow, which indicates the oxidation of Cu under RT. Later on, at step 17, Cu was again reduced to metallic state, which indicates that higher temperatures suppress the oxidation effect of O_2, which can be further supported by later results from step 19, in which Cu was oxidized again while the catalyst was cooled back down to RT. This might result from the reaction happening in between O_2 and H_2 at high temperature, leading to the consumption of O_2 before it could oxidize the catalyst. Unfortunately, such transient behavior does not match what was seen in the previous experiments, which means that the possible presence of traces of oxygen in the H_2 gas stream cannot account for the persistent copper oxidation reported above. More experiments will be needed to settle this issue and to identify the experimental factor that leads to the in situ oxidation of the Cu nanoparticles under H_2 atmospheres.

In Figure 4-12 we show the EXAFS results corresponding to the same experiments. The top panel reports the original signal, after background subtraction and conversion of the energy scale to k values, starting at the absorption edge. The bottom panel then shows the radial distribution function obtained from Fourier transformation of those data. It can be seen in that latter panel that there is a detectable feature at R ~ 1.5 Å that corresponds to the formation of Cu–O bonds in oxidized copper; the main peak at R ~ 2.2 Å represents the expected Cu–Cu bond. These observed features deviate from the actual Cu-O and Cu-Cu bond lengths due to phase-shift. These results are consistent with our XANES data.

As illustrated in the lower section of Figure 4-12, the complete reduction of Cu is evident at step 13. For 1st scan of step 14, an increased shoulder located at ~1.5 Å with the decline of feature at ~2.2 Å can be observed. This phenomenon signified the oxidation of Cu upon initial exposure to O_2 at ambient temperature. Nevertheless, during the second scan of step 14, both features exhibit inverse alterations. Rather than the continued growth of Cu-O and diminution of Cu-Cu, a reduction in the Cu-O feature and an enhancement in the Cu-Cu feature were observed. This observation implies that the catalyst is reduced under O_2/H_2 flow conditions, suggesting that Cu/SBA-15 remains unoxidized in the presence of H_2 flow with trace amounts of O_2.

In the two scans performed during step 15, evident oxidation is manifested through the increased feature at ~1.5 Å and the decreased feature at ~2.2 Å a result congruent with increased O_2 in the flow. Throughout the two scans in step 17, conducted at 350 °C, the absence of a feature at approximately ~1.5 Å is apparent, while the predominant feature resides at approximately ~2.2 Å. It is noteworthy that the feature at approximately ~2.2 Å exhibits a smaller magnitude compared to the scan in step 13, potentially attributable to the temperature effect. The final two scans in step 19 reveal the reoxidation of Cu under O_2/H_2 flow at room temperature, as evidenced by the presence of two features at approximately ~1.5 Å and ~2.2 Å.

In summary, the oxidation state of the Cu/SBA-15 catalyst was influenced by the gas atmosphere under various conditions. In the presence of H_2 flow with trace amounts of

O_2, the catalyst remained predominantly reduced. However, when the O_2 concentration in the flow increased, a clear oxidation trend was observed. Upon exposure to O_2/H_2 flow at elevated temperatures, the oxidation state was further impacted, and a reoxidation occurred under O_2/H_2 flow at room temperature.

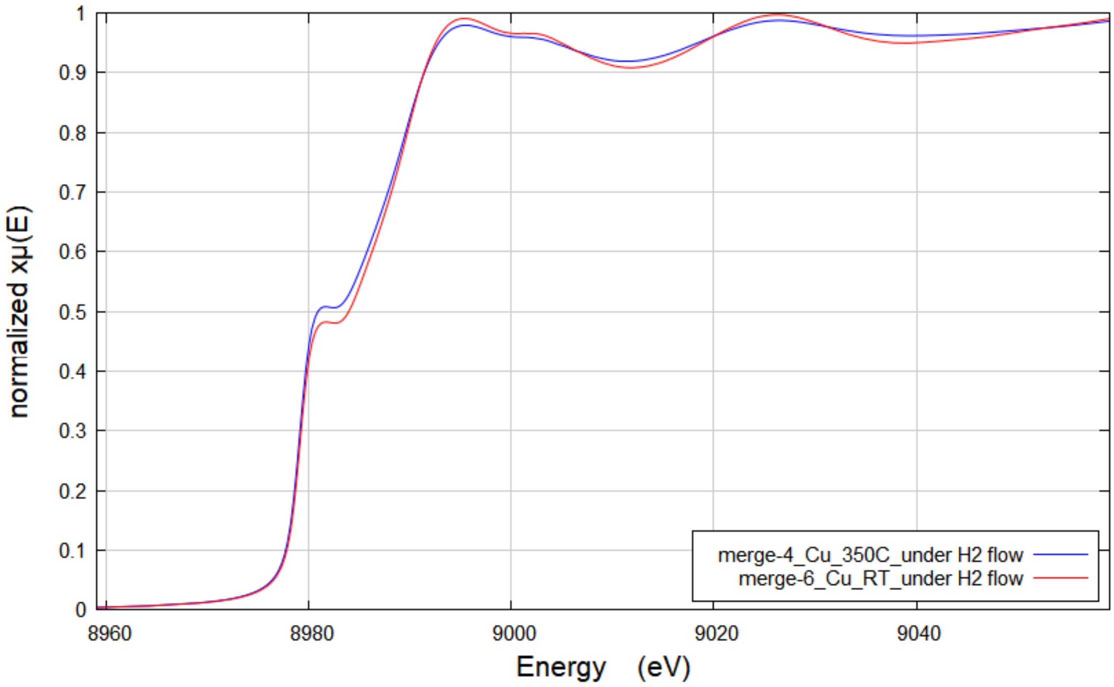

Figure 4-10. In situ Cu K-edge XANES spectra for Cu/SBA-15 catalyst , obtained under 300 ml/min of flowing H_2 gas. The blue trace represents data taken at 623 K while the other red trace represents data taken right after the sample was cooled down from 623 K to 290 K.

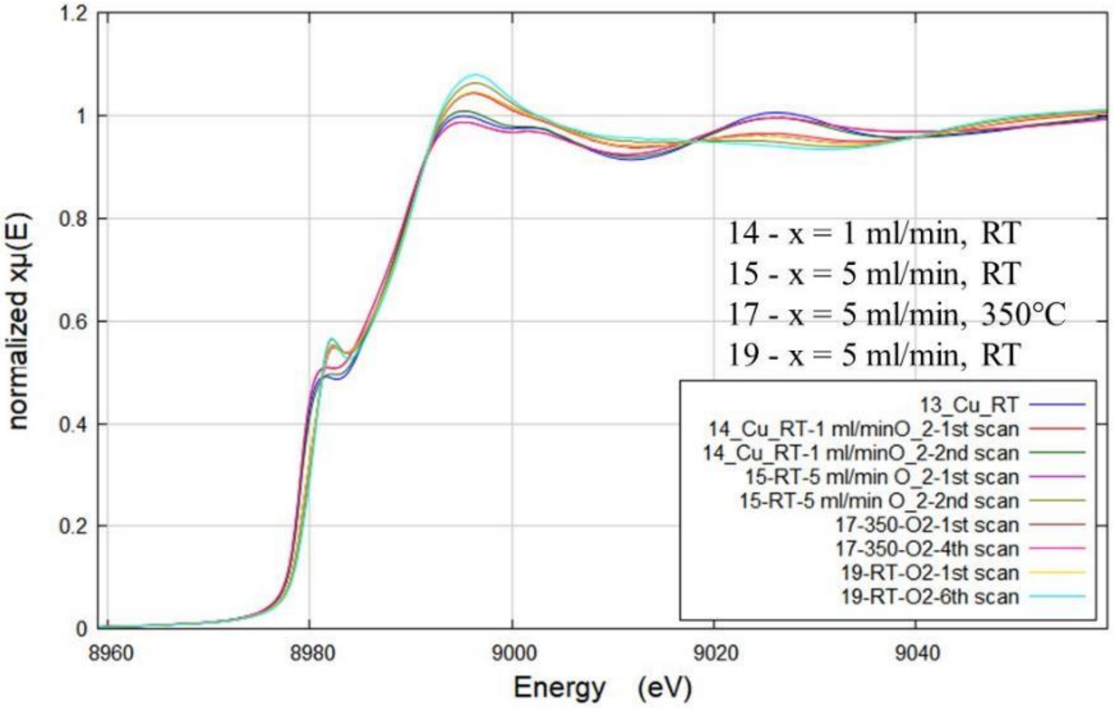

Figure 4-11. In situ Cu K-edge XANES spectra for Cu/SBA-15 catalyst. The Cu K edge spectra were obtained from several steps, numbers of steps are shown at the front of the name of each trace. Step 13 represents the data obtained after the reduced sample under H_2 flow under RT, step 14 are two scans of sample under the mixture of H_2 flow and 1 ml/min of O_2/He flow, step 15 is data acquired when O_2/He flow was increased to 5 ml/min, step 17 corresponds to data acquired under 623 K under the mixture of H_2 flow and O_2/He flow (5 ml/min), step 19 is collected after the sample was cool back down to RT under H_2 flow and O_2/He flow (5 ml/min).

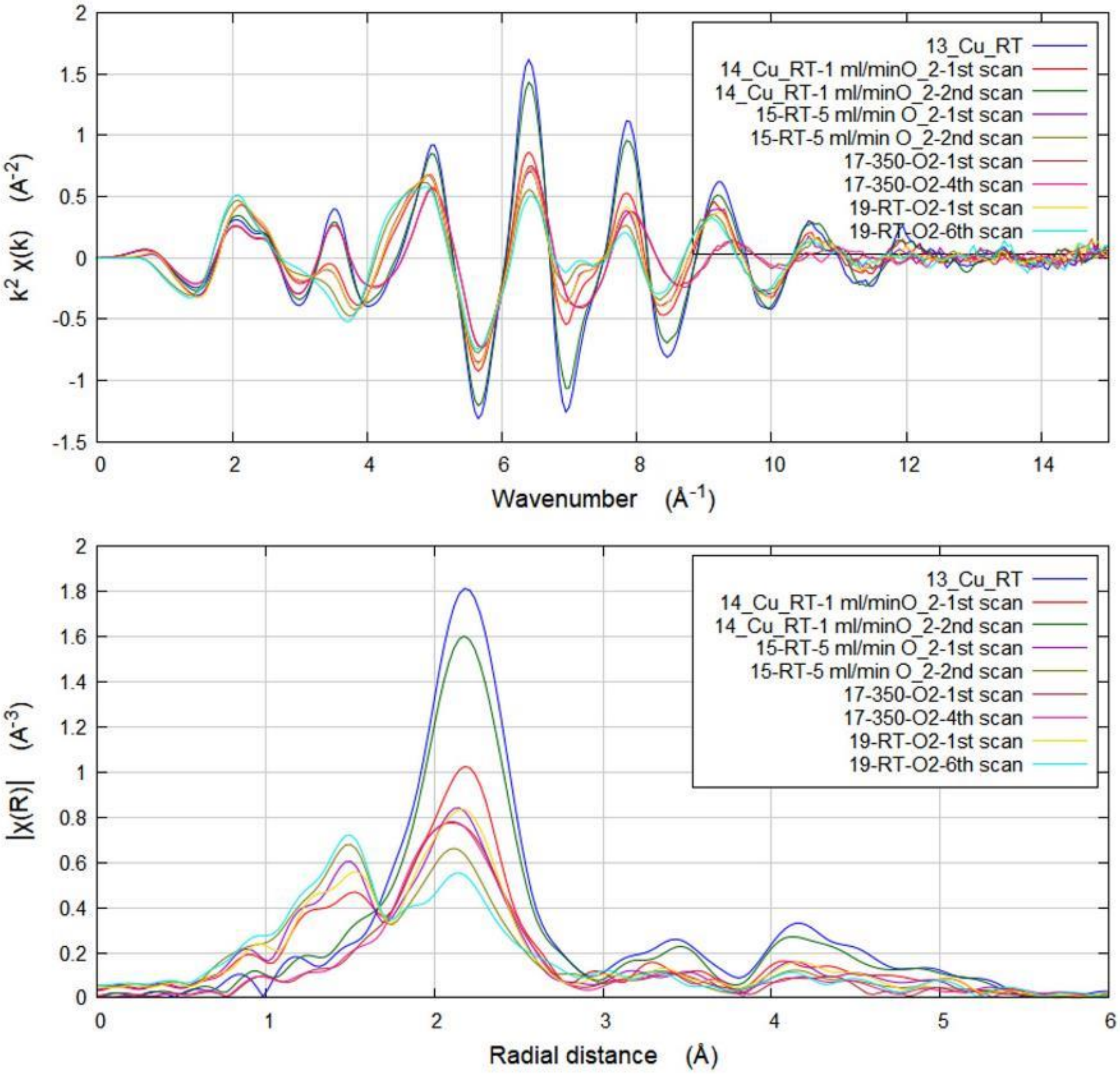

Figure 4-12. In situ Cu EXAFS spectra for Cu/SBA-15 catalyst. The Cu EXAFS spectra were obtained from Figure 4-11. The data are reported as a function of both k (top panel) and magnitude of the Fourier transform R (bottom).

4.3.2 XAS Results of $CuPt_{0.05}/SBA$-15

In this section, in situ XANES results are acquired for $CuPt_{0.05}/SBA$-15 under H_2, H_2 mixed with O_2/He, and H_2 mixed with H_2O vapor. The absorption edge of these traces in Figure 4-13 are all similar to the trace of step 20, which is Cu K edge after reduction. This indicates there was no oxidation happening when exposing $CuPt_{0.05}/SBA$-15 to H_2 with impurities like H_2O or O_2. Similar results can be obtained from the EXAFS results shown in Figure 4-14. In the bottom panel, a distinct observation can be made that, upon analyzing the data from step 20 and the four traces from step 21, there is a remarkable resemblance among them, primarily characterized by a predominant feature located at ~2.2 Å. For the rest two scans for step 22, little change can be observed other than slightly decreasing feather located at ~2.2 Å, suggesting negligible oxidation.

These results assist in excluding the possibility that trace quantities of O_2 or H_2O impurities contribute to the low-temperature oxidation of Cu. Like in the case of the pure Cu/SBA-15 catalyst, the oxidation of the surface observed in the earlier experiments still requires proper explanation.

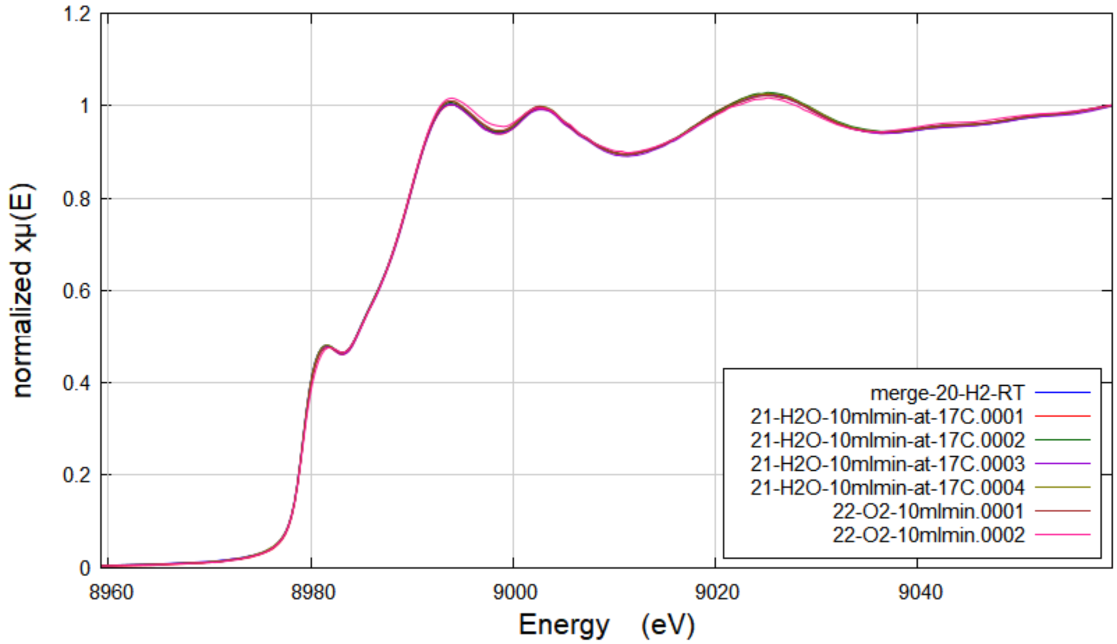

Figure 4-13. In situ Cu K-edge XANES spectra for $CuPt_{0.05}$/SBA-15. The Cu K edge spectra were obtained from several steps, number of steps are shown at the front of the name of each trace. Step 20 represents the data obtained with the catalyst been reduced at RT under H_2 flow, step 21 are four scans of sample under the mixture of H_2 with H_2O (H_2 bubble through water) at RT, step 22 are two scans of data acquired when O_2/He flow at RT (10 ml/min).

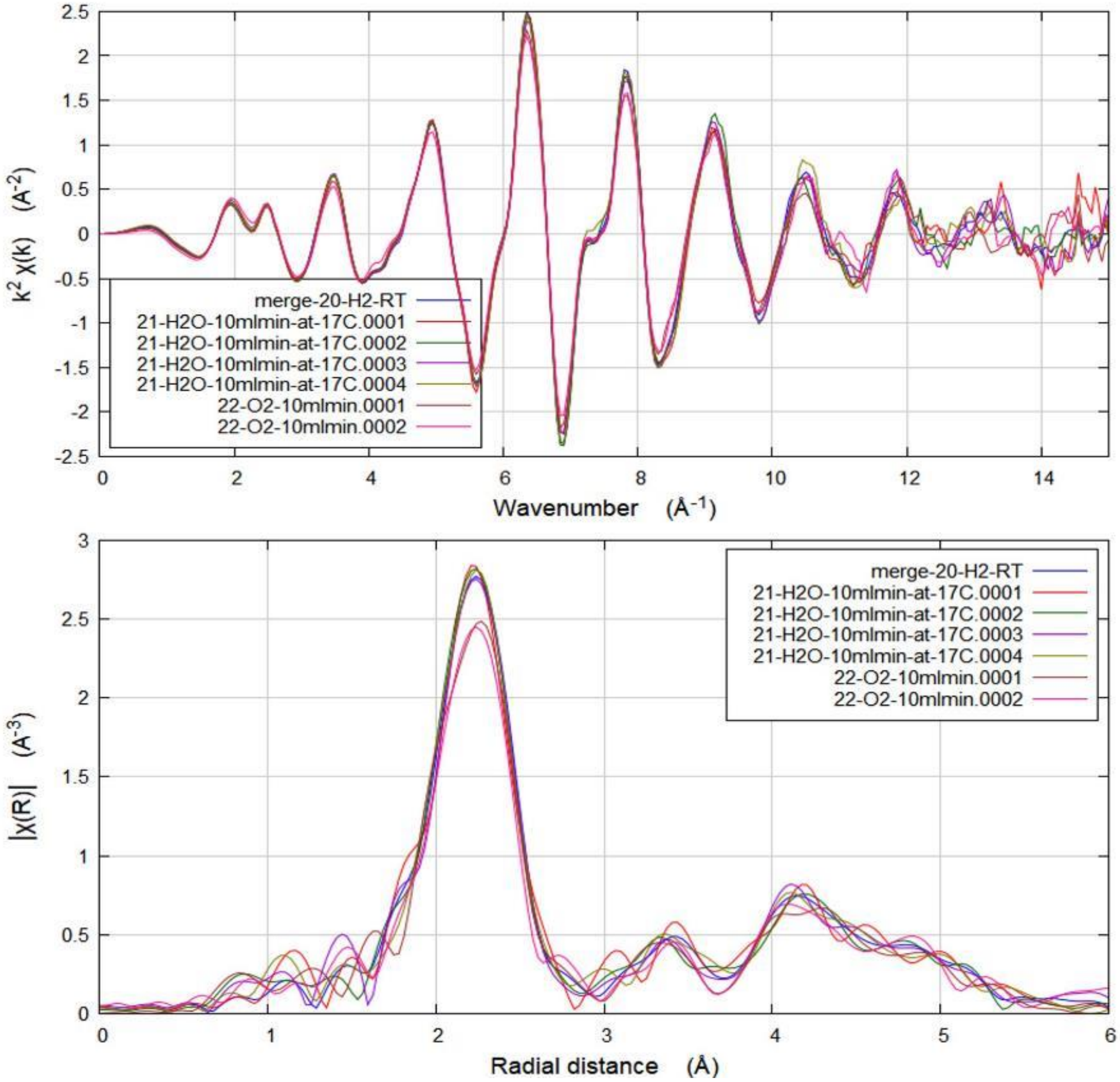

Figure 4-14. In situ Cu EXAFS spectra for $CuPt_{0.05}$/SBA-15 catalyst. The Cu EXAFS spectra were obtained from Figure 4-13. The data are reported as a function of both k (top panel) and magnitude of the Fourier transform R (bottom).

4.4 Conclusion

There appears to be anomalies in our results, since two experimental sections in this chapter appear to contradict each other. On the one hand, in section 4.2, oxidation of Cu was proved by our XAS experiments (also supported by part of our results in Chapter 5). On the other hand, our latest results with Cu/SBA-15 and $CuPt_{0.05}$/SBA-15 indicated that Cu oxidation appears not to occur in the presence of H_2 gas even if O_2 or H_2O impurities are added to the gas stream. Further experiments will be required to settle this issue.

In spite of the lack of reproducibility of the Cu oxidation results, an explanation for this behavior is required. For one, thermodynamic data clearly indicate the preference for bulk Cu to remain in metallic form under hydrogen atmospheres: as seen in the first two rows in Table 4-1, the standard enthalpies of reaction (ΔH°_r) for the reduction of CuO and Cu_2O are both highly negative, indicating that those reactions are highly exothermic. Moreover, the high stability of solid silica precludes the possibility of copper oxides being oxidized by the support (third and fourth row in Table 4-1). However, what we have observed in our catalysts is likely the formation of a thin surface oxide layer on small Cu-based NPs: the data in Figure 4-5 and Figure 4-8 provide an estimate for the thickness of the Cu_2O surface layer in the low-temperature regime of ~0.7 nm. Both the facts that the oxide forms on the surface, not the bulk, and that the metal is in the form of small NPs significantly affect the associated thermodynamics. In fact, the surface tension of metal oxides is significantly lower than that of metals, so, if metal oxides are mixed with zero-valent metal solids, the oxide is expected to segregate to the surface. In the case of Cu, its surface tension in liquid phase is reduced upon exposure to O_2, from $\gamma = 1.37$ J/m^2 for pure Cu to $\gamma = 0.53$ J/m^2 under 0.88 wt% O_2 (at 1370 K),[32] and the surface tension of a 80% Cu_2O + 20% CuO melt at 1573 K is $\gamma = 0.46$ J/m^2.[33] The values of the surface tension of solids are harder to come by, but for metals at least, are higher than for liquids:[34] values of $\gamma = 1.52$ and 1.70 J/m^2 have been reported for Cu bulk at 1253 K[35] and for 20 nm Cu NPs at 750 K,[36] respectively.

Table 4-1. Thermodynamic data for the reduction of bulk copper oxides with hydrogen gas and solid silica.[37-39]

Reaction	$\Delta H°_r$	$\Delta S°_r$	$\Delta G°_{300\ K}$	$\Delta G°_{495\ K}$
$CuO (s) + H_2 (g) \rightarrow Cu (s) + H_2O (g)$	–85.77	48.74	–100.39	–109.90
$Cu_2O (s) + H_2 (g) \rightarrow 2 Cu (s) + H_2O (g)$	–73.21	31.36	–82.62	–88.73
$2 CuO (s) + Si (s) \rightarrow 2 Cu (s) + SiO_2 (s)$	–593.37	7.35	–595.58	–597.01
$4 Cu_2O (s) + Si (s) \rightarrow 4 Cu (s) + SiO_2 (s)$	–568.25	–93.75	–540.13	–521.84

There are multiple possible scenarios that could account for the observed low-temperature oxidation of the metal. It is possible that the H_2 feed contains trace amounts of oxidizing impurities. In addition to that, based on our further analysis in 4.3, it is less likely that oxidation of Cu took place with a relatively small amount of H_2O or O_2.

It may be tempting to dismiss the results on this basis, concluding that we may not have been careful enough to avoid this interference. However, we did work hard to prevent the introduction of such contamination into our gas streams and observed the same reversible redox chemistry in four entirely different experimental setups (in three different flow reactors at three different synchrotron facilities –NSLS II, APS, and SSRL– as well as in the batch reactor used for the IR data acquisition). We are still in the process of exploring the possible reasons for the oxidation. Moreover, it is important to realize that the catalysts are always reduced after high-temperature H_2 treatments (even with impurities like O_2 at 623 K as shown in Figure 4-11 in step 17); it is only when the temperature was lowered below approximately 350 K that (reversible) oxidation takes place. It is also worth mentioning that this temperature dependence can be justified on the basis of entropic arguments, as the entropies of CuO_x reduction with H_2 are all positive (Table 4-1-third column); the magnitude of the Gibbs free energy for the reduction decreases with decreasing temperature (Table 4-1-fourth versus fifth columns), and could eventually flip to favor the oxide.

Given that the catalytic hydrogenation of most organic reactants is typically carried out at low temperatures and high probability of impurities entering the hydrogenation catalysis process, the formation of thin oxide layers on Cu-based catalysts reported here may be of high relevance to their performance. At the very least, it is an issue that needs to be kept in mind when designing Cu-based hydrogenation catalytic systems. Fortunately, in the particular case of the selective hydrogenation of unsaturated aldehydes using $CuPt_x$ single-atom alloys, thermal desorption experiments with model single-crystal Cu surfaces showed that oxygen-modified surfaces hydrogenate the unsaturated aldehydes with similar energetics and high selectivities as those seen on metallic substrates.[40-41] Also, the addition of Pt does not seem to affect this reversible Cu redox chemistry, at least not in the limit of low Pt content as is the case in SAAs.[42]

4.5 Reference

1. Sharma, A. S.; Kaur, H.; Shah, D., Selective oxidation of alcohols by supported gold nanoparticles: recent advances. *RSC Adv.* **2016,** *6* (34), 28688-28727.

2. Zaera, F., Gold-Titania Catalysts for Low-Temperature Oxidation and Water Splitting. *Top. Catal.* **2018,** *61* (5), 336-347.

3. Carabineiro, S. A. C., Supported Gold Nanoparticles as Catalysts for the Oxidation of Alcohols and Alkanes. *Front. Chem.* **2019,** *7* (702).

4. Hutchings, G. J., Heterogeneous Gold Catalysis. *ACS Cent. Sci.* **2018,** *4* (9), 1095-1101.

5. Corma, A.; Leyva-Pérez, A.; Sabater, M. J., Gold-Catalyzed Carbon–Heteroatom Bond-Forming Reactions. *Chem. Rev.* **2011,** *111* (3), 1657-1712.

6. Takei, T.; Akita, T.; Nakamura, I.; Fujitani, T.; Okumura, M.; Okazaki, K.; Huang, J.; Ishida, T.; Haruta, M., Heterogeneous Catalysis by Gold. *Adv. Catal.* **2012,** *55*, 1-126.

7. Stratakis, M.; Garcia, H., Catalysis by Supported Gold Nanoparticles: Beyond Aerobic Oxidative Processes. *Chem. Rev.* **2012,** *112* (8), 4469-4506.

8. Ishida, T.; Koga, H.; Okumura, M.; Haruta, M., Advances in Gold Catalysis and Understanding the Catalytic Mechanism. *Chem. Rec.* **2016,** *16* (5), 2278-2293.

9. Barakat, T.; Rooke, J. C.; Genty, E.; Cousin, R.; Siffert, S.; Su, B.-L., Gold catalysts in environmental remediation and water-gas shift technologies. *Energy Environ. Sci.* **2013,** *6* (2), 371-391.

10. Qian, H.; Pretzer, L. A.; Velazquez, J. C.; Zhao, Z.; Wong, M. S., Gold nanoparticles for cleaning contaminated water. *J. Chem. Technol. Biotechnol.* **2013,** *88* (5), 735-741.

11. Serafin, J. G.; Liu, A. C.; Seyedmonir, S. R., Surface science and the silver-catalyzed epoxidation of ethylene: an industrial perspective. *J. Mol. Catal. A: Chem.* **1998,** *131* (1), 157-168.

12. Monnier, J. R., The direct epoxidation of higher olefins using molecular oxygen. *Appl. Catal. A* **2001,** *221* (1-2), 73.

13. Lei, Y.; Mehmood, F.; Lee, S.; Greeley, J.; Lee, B.; Seifert, S.; Winans, R. E.; Elam, J. W.; Meyer, R. J.; Redfern, P. C.; Teschner, D.; Schlögl, R.; Pellin, M. J.;

Curtiss, L. A.; Vajda, S., Increased Silver Activity for Direct Propylene Epoxidation via Subnanometer Size Effects. *Science* **2010,** *328* (5975), 224-228.

14. Khatib, S. J.; Oyama, S. T., Direct Oxidation of Propylene to Propylene Oxide with Molecular Oxygen: A Review. *Catal. Rev.* **2015,** *57* (3), 306-344.

15. Li, Y.; Fu, Q.; Flytzani-Stephanopoulos, M., Low-temperature water-gas shift reaction over Cu- and Ni-loaded cerium oxide catalysts. *Applied Catalysis B: Environmental* **2000,** *27* (3), 179-191.

16. Gawande, M. B.; Goswami, A.; Felpin, F.-X.; Asefa, T.; Huang, X.; Silva, R.; Zou, X.; Zboril, R.; Varma, R. S., Cu and Cu-Based Nanoparticles: Synthesis and Applications in Catalysis. *Chemical Reviews* **2016,** *116* (6), 3722-3811.

17. Chen, A.; Yu, X.; Zhou, Y.; Miao, S.; Li, Y.; Kuld, S.; Sehested, J.; Liu, J.; Aoki, T.; Hong, S.; Camellone, M. F.; Fabris, S.; Ning, J.; Jin, C.; Yang, C.; Nefedov, A.; Wöll, C.; Wang, Y.; Shen, W., Structure of the catalytically active copper–ceria interfacial perimeter. *Nature Catalysis* **2019,** *2* (4), 334-341.

18. Nix, R. M.; Rayment, T.; Lambert, R. M.; Jennings, J. R.; Owen, G., An in situ X-ray diffraction study of the activation and performance of methanol synthesis catalysts derived from rare earth-copper alloys. *Journal of Catalysis* **1987,** *106* (1), 216-234.

19. Nerlov, J.; Sckerl, S.; Wambach, J.; Chorkendorff, I., Methanol synthesis from CO2, CO and H2 over Cu(100) and Cu(100) modified by Ni and Co. *Applied Catalysis A: General* **2000,** *191* (1), 97-109.

20. Yang, R. Q.; Gai, X. K.; Xing, C.; Mao, J. W.; Lv, C. X., Performance of Cu-Based Catalysts in Low-Temperature Methanol Synthesis. *Advanced Materials Research* **2014,** *1004-1005*, 1623-1626.

21. van de Water, L. G. A.; Wilkinson, S. K.; Smith, R. A. P.; Watson, M. J., Understanding methanol synthesis from CO/H2 feeds over Cu/CeO2 catalysts. *Journal of Catalysis* **2018,** *364*, 57-68.

22. Zhu, J.; Su, Y.; Chai, J.; Muravev, V.; Kosinov, N.; Hensen, E. J. M., Mechanism and Nature of Active Sites for Methanol Synthesis from CO/CO2 on Cu/CeO2. *ACS Catalysis* **2020,** *10* (19), 11532-11544.

23. Cao, Y.; Chen, B.; Guerrero-Sánchez, J.; Lee, I.; Zhou, X.; Takeuchi, N.; Zaera, F., Controlling Selectivity in Unsaturated Aldehyde Hydrogenation Using Single-Site Alloy Catalysts. *ACS Catal.* **2019,** *9*, 9150-9157.

24. Robertson, S. D.; McNicol, B. D.; De Baas, J. H.; Kloet, S. C.; Jenkins, J. W., Determination of reducibility and identification of alloying in copper-nickel-on-silica catalysts by temperature-programmed reduction. *J. Catal.* **1975,** *37* (3), 424-431.

25. Kohler, M. A.; Cant, N. W.; Wainwright, M. S.; Trimm, D. L., Infrared spectroscopic studies of carbon monoxide adsorbed on a series of silica-supported copper catalysts in different oxidation states. *Journal of Catalysis* **1989,** *117* (1), 188-201.

26. Huang, Z.; Cui, F.; Kang, H.; Chen, J.; Zhang, X.; Xia, C., Highly Dispersed Silica-Supported Copper Nanoparticles Prepared by Precipitation−Gel Method: A Simple but Efficient and Stable Catalyst for Glycerol Hydrogenolysis. *Chem. Mater.* **2008,** *20* (15), 5090-5099.

27. Han, T.; Lee, I.; Cao, Y.; Zhou, X.; Zaera, F., Thermodynamics of Carbon Monoxide Adsorption on Cu/SBA-15 Catalysts: Under Vacuum versus under Atmospheric Pressures. *J. Phys. Chem. C* **2022**, DOI: 10.1021/acs.jpcc.1c10722.

28. Cao, Y.; Guerrero-Sańchez, J.; Lee, I.; Zhou, X.; Takeuchi, N.; Zaera, F., Kinetic Study of the Hydrogenation of Unsaturated Aldehydes Promoted by CuPtx/SBA-15 Single-Atom Alloy (SAA) Catalysts. *ACS Catalysis* **2020,** *10* (5), 3431-3443.

29. Wagner, C. D.; Riggs, W. M.; Davis, L. E.; Moulder, J. F.; Muilenberg, G. E., *Handbook of X-Ray Photoelectron Spectroscopy*. Perkin-Elmer Corporation: Eden Prairie, MN, 1978.

30. Frenkel, A. I.; Hills, C. W.; Nuzzo, R. G., A View from the Inside: Complexity in the Atomic Scale Ordering of Supported Metal Nanoparticles. *J. Phys. Chem. B* **2001,** *105* (51), 12689-12703.

31. Jaque, P.; Toro-Labbé, A., Characterization of copper clusters through the use of density functional theory reactivity descriptors. *J. Chem. Phys.* **2002,** *117* (7), 3208-3218.

32. Overbury, S. H.; Bertrand, P. A.; Somorjai, G. A., Surface composition of binary systems. Prediction of surface phase diagrams of solid solutions. *Chem. Rev.* **1975,** *75* (5), 547-560.

33. Takasu, T.; Itou, H.; Nakamura, T., Density and Surface Tension of Cu_xO Bearing Slags. *High Temp. Mater. Processes (Berlin, Ger.)* **2003,** *22* (3-4), 203-210.

34. Jia, M.; Lai, Y.; Tian, Z.; Liu, Y., Calculation of the surface free energy of fcc copper nanoparticles. *Modell. Simul. Mater. Sci. Eng.* **2009,** *17* (1), 015006.

35. Kumykov, V. K.; Sergeev, I. N.; Sozaev, V. A.; Gedgagova, M. V., Surface tension of copper in solid phase. *Bull. Russ. Acad. Sci.: Phys.* **2017,** *81* (3), 357-359.

36. Gozzi, D.; Tomellini, M.; Lazzarini, L.; Latini, A., High-Temperature Determination of Surface Free Energy of Copper Nanoparticles. *J. Phys. Chem. C* **2010,** *114* (28), 12117-12124.

37. Cox, J. D.; Wagman, D. D.; Medvedev, V. A., *CODATA Key Values for Thermodynamics*. Hemisphere Publishing Corp.: New York, 1989.

38. Chase, M. W., Jr., NIST-JANAF Themochemical Tables. *J. Phys. Chem. Ref. Data* **1998,** *Monograph 9*, 1-1951.

39. Piccione, P. M.; Woodfield, B. F.; Boerio-Goates, J.; Navrotsky, A.; Davis, M. E., Entropy of Pure-Silica Molecular Sieves. *J. Phys. Chem. B* **2001,** *105* (25), 6025-6030.

40. Chen, B.; Zaera, F., Hydrogenation of Cinnamaldehyde on Cu(110) Single-Crystal Surfaces. *J. Phys. Chem. C* **2021,** *125* (27), 14709–14717.

41. Chen, B.; Ponce, R.; Guerrero-Sánchez, J.; Takeuchi, N.; Zaera, F., Cinnamaldehyde adsorption and thermal decomposition on copper surfaces. *J. Vac. Sci. Technol., A* **2021,** *39* (5), 053205.

42. Han, T.; Lee, I.; Cao, Y.; Zhou, X.; Zaera, F., Thermodynamics of Carbon Monoxide Adsorption on Cu/SBA-15 Catalysts: Under Vacuum versus under Atmospheric Pressures. *The Journal of Physical Chemistry C* **2022,** *126* (6), 3078-3086.

43. Zaera, F., Infrared Absorption Spectroscopy of Adsorbed CO: New Applications in Nanocatalysis for an Old Approach. *ChemCatChem* **2012,** *4* (10), 1525-1533.

44. Zaera, F., New advances in the use of infrared absorption spectroscopy for the characterization of heterogeneous catalytic reactions. *Chemical Society Reviews* **2014,** *43* (22), 7624-7663.

45. Han, T.; Li, Y.; Cao, Y.; Lee, I.; Zhou, X.; Frenkel, A. I.; Zaera, F., In situ identification of surface sites in Cu–Pt bimetallic catalysts: Gas-induced metal segregation. *The Journal of Chemical Physics* **2022,** *157* (23), 234706.

46. Kappers, M. J.; van der Maas, J. H., Correlation between CO frequency and Pt coordination number. A DRIFT study on supported Pt catalysts. *Catal. Lett.* **1991,** *10* (5-6), 365-373.

47. Albiter, M. A.; Zaera, F., Adsorption Properties of Supported Platinum Catalysts Prepared using Dendrimers. *Langmuir* **2010,** *26* (21), 16204–16210.

48. Asokan, C.; DeRita, L.; Christopher, P., Using probe molecule FTIR spectroscopy to identify and characterize Pt-group metal based single atom catalysts. *Chin. J. Catal.* **2017,** *38* (9), 1473-1480.

49. Dandekar, A.; Vannice, M. A., Determination of the Dispersion and Surface Oxidation States of Supported Cu Catalysts. *Journal of Catalysis* **1998,** *178* (2), 621-639.

Chapter 5 In Situ IR Study of Oxidation State of Copper in Cu-Pt Single-Atom Catalysts

Oxidation state of Cu-Pt single-atom catalysts was discussed in Chapter 4 in regard to the XAS results. In this chapter, in situ IR results of $CuPt_x$/SBA-15 are discussed.

5.1 Discussion of In Situ Infrared data

5.1.1 Reducibility of the $CuPt_x$/SBA-15

The reducibility of the $CuPt_x$/SBA-15 catalysts was also tested in an indirect way by using *in situ* infrared absorption spectroscopy (IR), together with carbon monoxide as a probe molecule.[43-44] Representative data obtained from these experiments are presented in Figure 5-1 in our previous work[45]. Two types of experiments were carried out. In the first, the catalyst ($CuPt_{0.1}$/SBA-15 in this case) was first reduced in a H_2 atmosphere (200 Torr at 495 K) and then probed by adding a small amount of CO to the gas at room temperature (300 K, Figure 5-1-left panel): after an initial addition of 0.2 Torr CO, no adsorption could be detected, but upon adding another 0.2 Torr CO, two peaks were clearly seen at 2029 and 2127 cm^{-1} corresponding to the C–O stretching mode of CO adsorbed on atop sites of metallic Pt[46-48] and Cu[25, 27, 49] surfaces, respectively. The interesting observation is that the intensity of both features increases after each of the two cycles of heating the sample from 300 K to 495 K and cooling it back to 300 K. This is explained by the reduction of the Cu_2O surface layer that presumably was not fully removed by the H_2 treatment, and to the resulting creation of additional metallic Cu sites available for CO uptake; further confirmation of this interpretation is given by the growth of the peaks in the 2300 - 2400 cm^{-1} range due to CO_2, the product of CO oxidation. The second set of experiments were done with H_2 + CO gas mixtures, 100 Torr H_2 + 0.2 Torr CO in the example shown in the right panel of Figure 5-1 (which corresponds to a $CuPt_{0.2}$/SBA-15 catalyst). The peak at 2132 cm^{-1} for CO adsorption on metallic Cu is again seen to grow upon cycling to 495 K and back, a procedure that was carried out three times in this case. The same explanation applies here, namely, that the small amount of CO added to the H_2 gas helps complete the reduction of the metal NPs, removing the residual Cu_2O layer present on the surface under H_2 atmospheres at low temperatures.

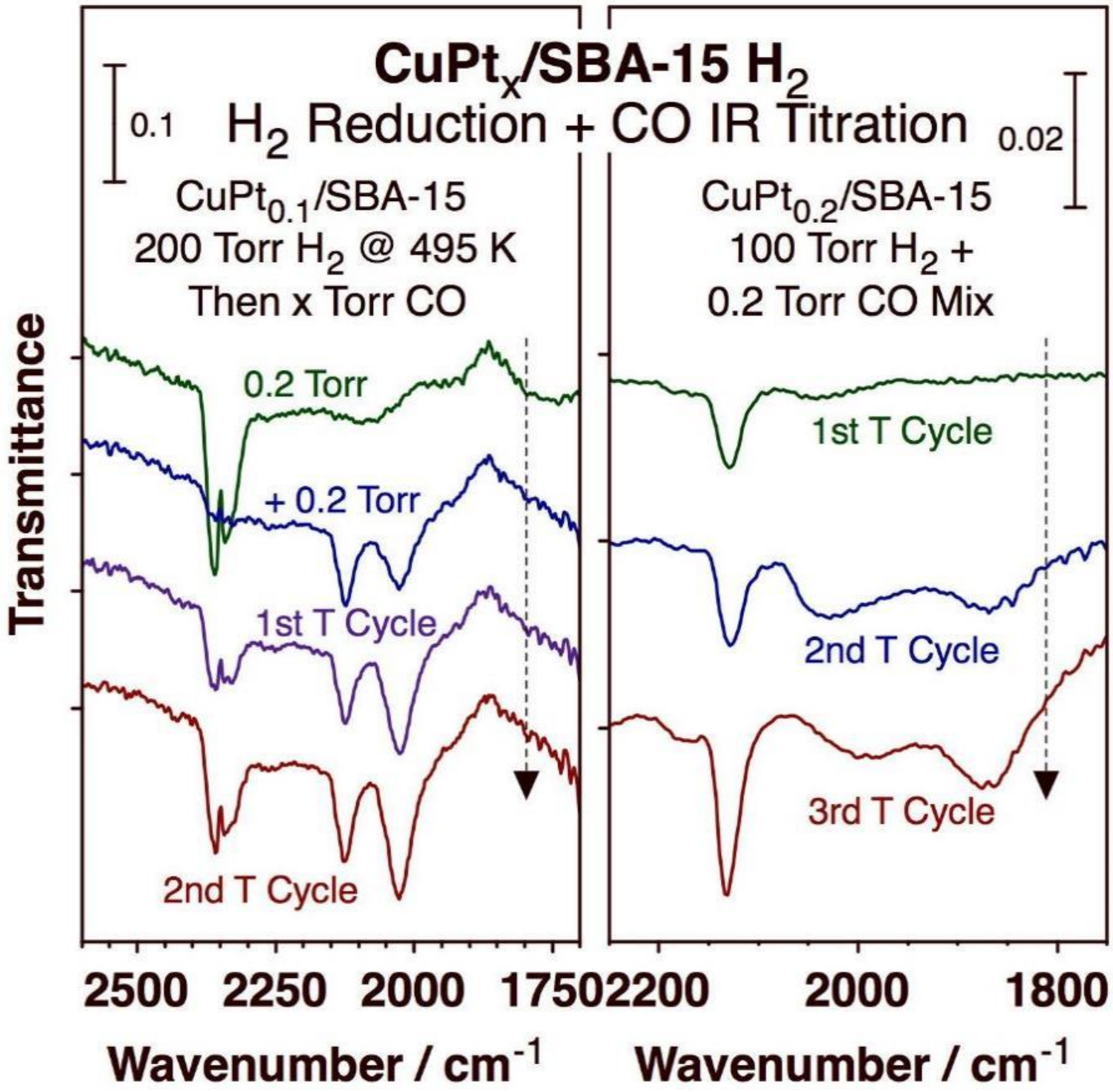

Figure 5-1. IR spectra of CO adsorbed on CuPt$_x$/SBA-15 catalysts after different H_2 reduction treatments. Left: Spectra for CuPt$_{0.1}$/SBA-15, first reduced in a 200 Torr H_2 atmosphere, after adding a small amount of CO and cycling the temperature to 495 K and back to 300 K. Right: Data for CuPt$_{0.2}$/SBA-15 exposed to a 100 Torr H_2 + 0.2 Torr CO mixture; the spectra were obtained after each of three consecutive heating cycles to 495 K and cooling back down to 300 K. Adapted with Permission of AIP Publishing from [In situ identification of surface sites in Cu–Pt bimetallic catalysts: Gas-induced metal segregation].

5.1.2 Results of In Situ IR Studies Dependent on Temperature and Pressure

In addition to Figure 5-1, other work has been performed regarding the IR experiments as a function of temperature for several CO pressures on several catalysts. Peaks for Cu-CO and Pt-CO can be seen for all $CuPt_x$ catalysts, but their peak area and their shapes change in different conditions. Consistent with our previous work, the signals from Cu-CO species were enhanced in intensity with the pressure of CO and attenuated with the increasing temperature. However, the trend is the opposite for CO adsorbed on atop sites on the surface of metallic platinum NPs. This can be seen in Figure 5-2, where CO IR spectra are shown for a family of $CuPt_x$ as a function of temperature for 10 Torr CO. Typically, due to the reduction of CuO_x by introducing CO, it is expected that the intensity of peak locates at 2124 cm^{-1} increased after one cycle of heating and cooling, corresponding to the increasing CO bonded on atop sites on the surface of the metallic Cu NPs of the catalyst. It should be noted that the peak area increased for most of the catalysts after heating up to 495 K and then cooling back to 295 K in the following Figure 5-2, except for sample $CuPt_{0.05}$/SBA-15 and under 20 Torr CO. This could result from the consumption of CO by CuO_x or other impurities inside the transmission cell.

Table 5-1 and Figure 5-3 correspond to the peak area of Cu-CO in Figure 5-2, and thus provide a straightforward way for us to understand how the peak intensity changed as a function of temperature.

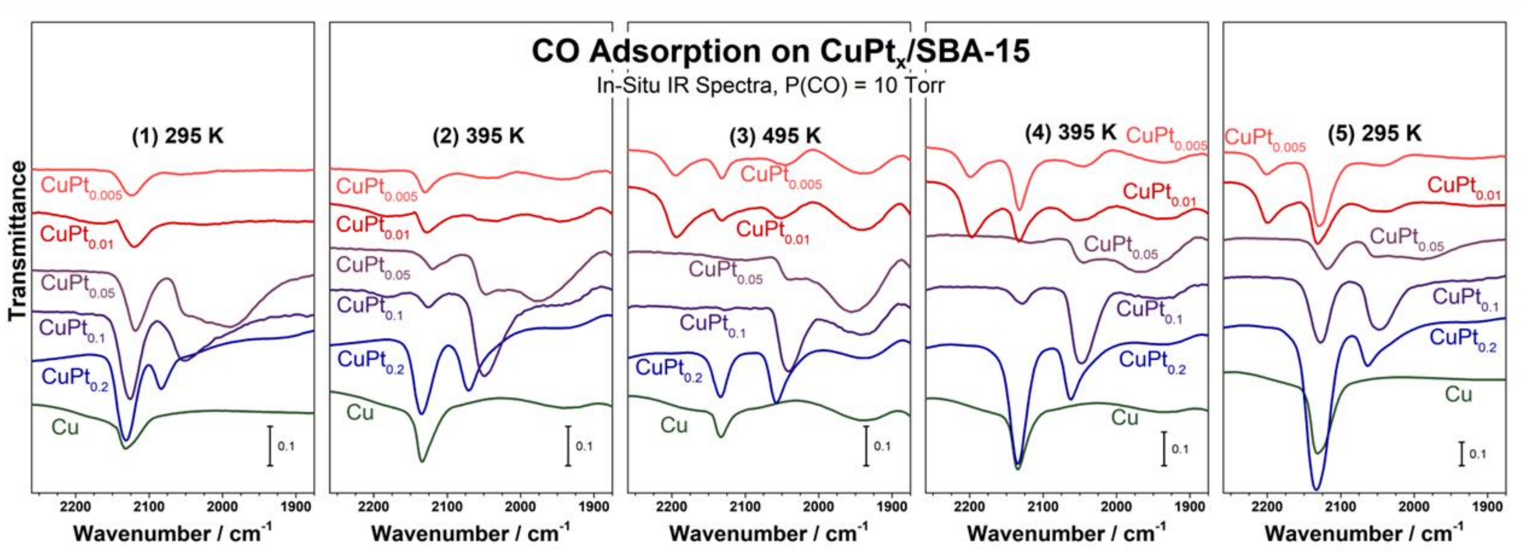

Figure 5-2. In situ IR spectra of CO adsorbed on a family of CuPt$_x$/SBA-15 catalyst as a function of Pt content (x), in the presence of 10 Torr of CO in the gas phase (after subtraction of the gas-phase contribution). Five panels are provided, showing the traces recorded at 295 K (left), after heating to 395 K (second to left), after heating to 495 K (center), upon cooling back to 395 K (second to right), and upon cooling back down to 295 K again (right).

Table 5-1 Peak area on CO/Cu from In-Situ CO Adsorption on $CuPt_x$/SBA-15, P(CO) = 10 Torr.

Temperature (K)	Cu	$CuPt_{0.2}$	$CuPt_{0.1}$	$CuPt_{0.05}$	$CuPt_{0.01}$	$CuPt_{0.005}$
295	3.42	7.81	6.87	5.43	1.27	1.51
395	4.82	6.37	1.00	1.92	0.98	1.35
495	2.35	2.84	0.00	1.09	0.49	0.91
395	5.34	10.73	1.28	1.08	2.12	3.14
295	11.38	26.50	8.69	4.51	4.29	6.75

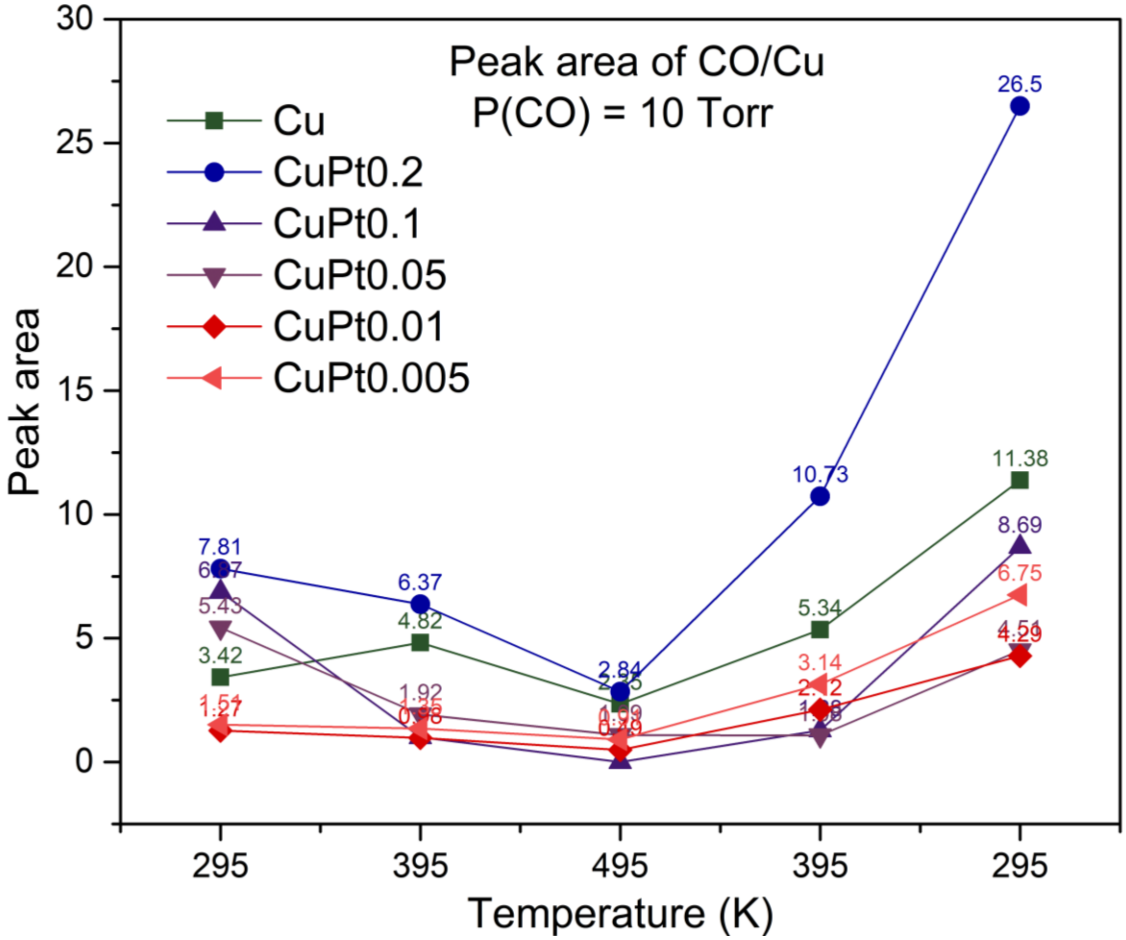

Figure 5-3. Peak area of CO/Cu from In-Situ CO Adsorption on $CuPt_x$/SBA-15 as a function of temperature, P(CO) = 10 Torr.

To better understand the surface of Cu atoms on the same catalysts under different CO pressure, Figure 5-3, Figure 5-4, Figure 5-5, Figure 5-6, Figure 5-7, and Figure 5-8, are shown below. They are In-Situ IR Spectra as a function of the temperature of CO adsorbed on Cu/SBA-15, $CuPt_{0.2}$/SBA-15, $CuPt_{0.1}$/SBA-15, and $CuPt_{0.05}$/SBA-15, $CuPt_{0.01}$/SBA-15, and $CuPt_{0.005}$/SBA-15, respectively. Similar conclusions can be drawn from them. After one cycle of heating and cooling, the peak intensity of Cu-CO goes up due to the reduction of the CO atmosphere, which is consistent with our previous work[1-2]. In addition to the conclusions above, one thing that seems anomalous is that the peak located at around 2200 cm^{-1}, which can be assigned to CO on CuO_x, are slightly increasing for $CuPt_{0.01}$/SBA-15 while exposed to CO when heated from room temperature (300 K) to 495 K and back. However, such a phenomenon should be considered an error since the peak area of CO on CuO_x only oscillates within a certain range.

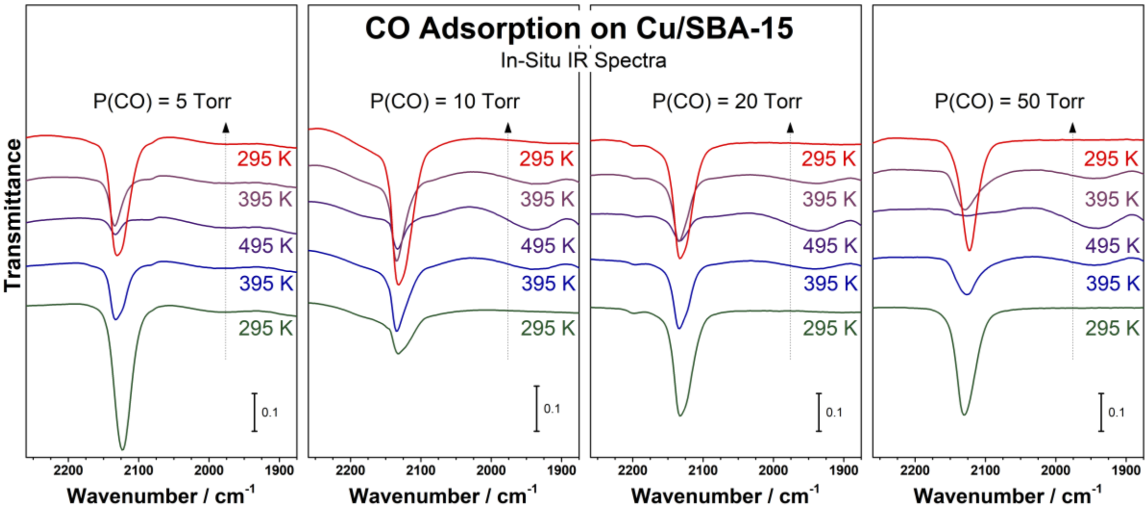

Figure 5-4. *In situ* IR spectra of CO adsorbed on Cu/SBA-15 catalyst as a function of temperature in the presence of x Torr of CO in the gas phase (after subtraction of the gas-phase contribution). Four panels are provided, showing the traces recorded at 5 Torr (left), 10 Torr (second to left), 20 Torr (second to right), and 50 Torr (right).

Table 5-2. Peak area of CO/Cu from CO Adsorption on Cu/SBA-15 for one cycle of heating and cooling, In-Situ IR Spectra vs. P(CO)

Temperature (K)	Pressure of CO (Torr)			
	5	10	20	50
295	12.25	3.42	9.13	4.73
395	4.54	4.82	5.09	3.53
495	1.1	2.35	1.86	0.75
395	3.34	5.34	4.73	4.57
295	10.68	11.38	9.84	9.66

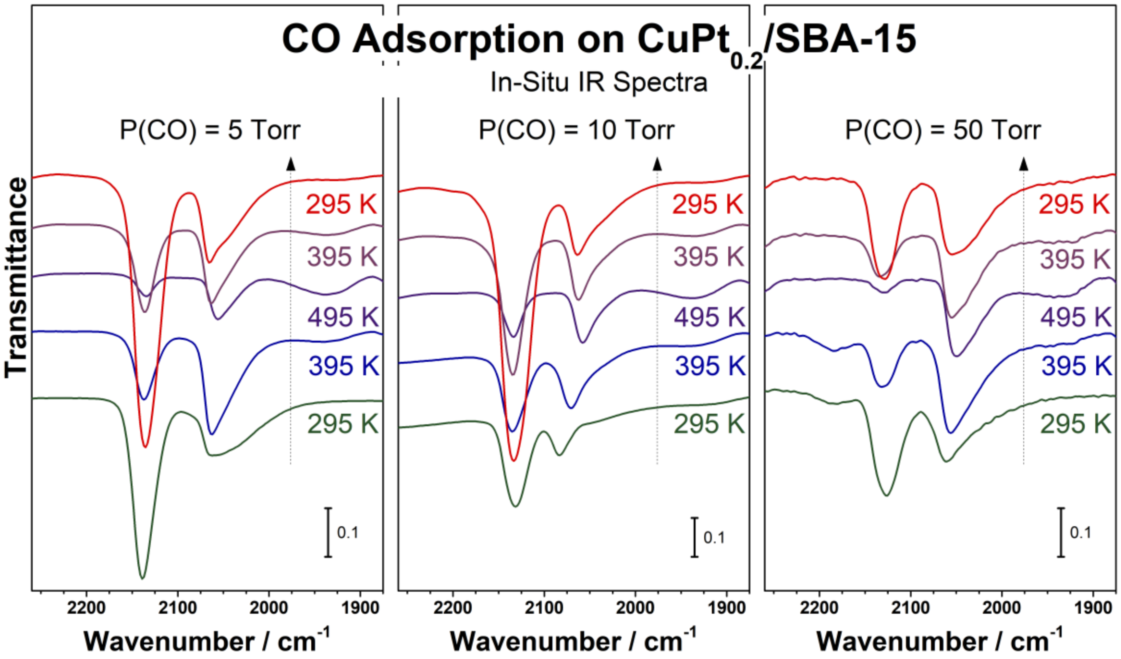

Figure 5-5. *In situ* IR spectra of CO adsorbed on $CuPt_{0.2}$/SBA-15 catalyst as a function of temperature in the presence of x Torr of CO in the gas phase (after subtraction of the gas-phase contribution). Four panels are provided, showing the traces recorded at 5 Torr (left), 10 Torr (center), and 50 Torr (right).

Table 5-3. Peak area of CO/Cu from CO Adsorption on $CuPt_{0.2}$/SBA-15 for one cycle of heating and cooling, In-Situ IR Spectra vs. P(CO)

Temperature (K)	Pressure of CO (Torr)		
	5	10	50
295	11.78	7.81	6.8
395	4.48	6.37	2.8
495	1.49	2.84	0.7
395	5.41	10.73	2.5
295	19.43	26.5	6.3

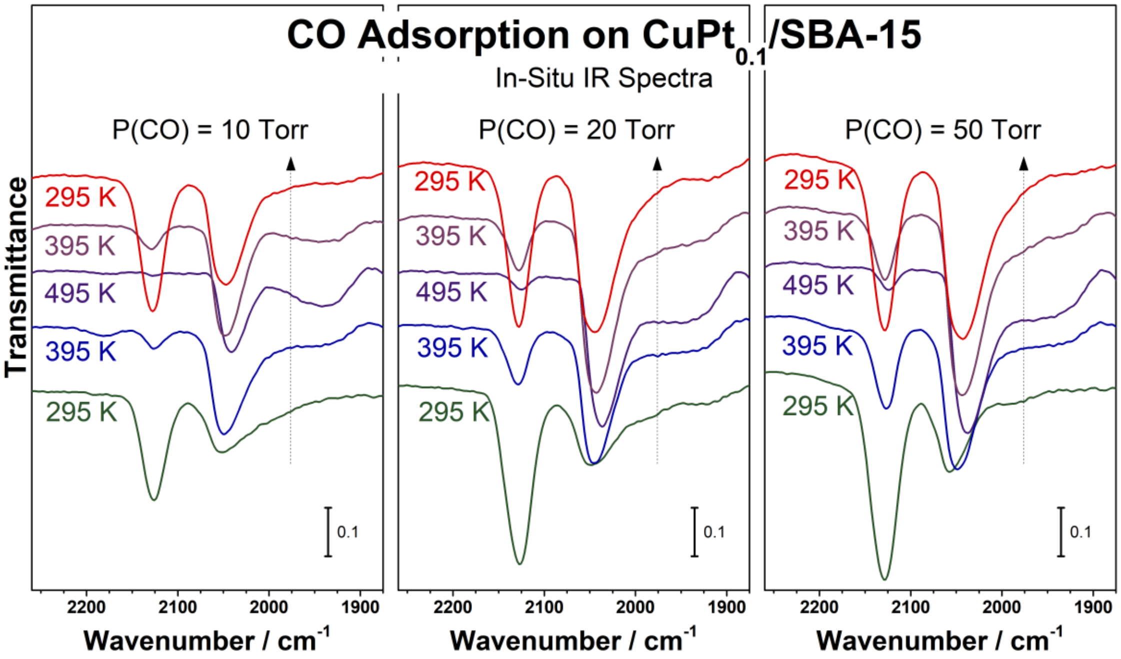

Figure 5-6. *In situ* IR spectra of CO adsorbed on CuPt$_{0.1}$/SBA-15 catalyst as a function of temperature in the presence of x Torr of CO in the gas phase (after subtraction of the gas-phase contribution). Four panels are provided, showing the traces recorded at 10 Torr (left), 20 Torr (center), and 50 Torr (right).

Table 5-4. Peak area of CO/Cu from CO Adsorption on CuPt$_{0.1}$/SBA-15 for one cycle of heating and cooling, In-Situ IR Spectra vs. P(CO)

Temperature (K)	Pressure of CO (Torr)		
	10	20	50
295	6.87	12.54	14.23
395	1	3.4	4.55
495	0	0.96	1.19
395	1.28	2.98	3.81
295	8.69	10.18	11

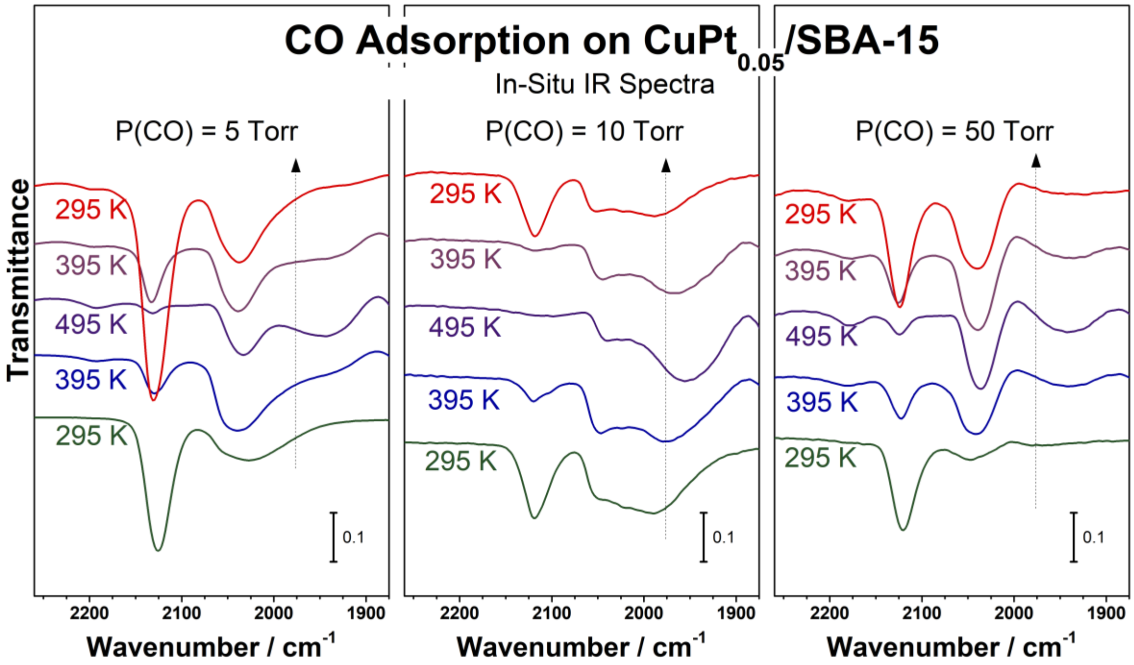

Figure 5-7. *In situ* IR spectra of CO adsorbed on $CuPt_{0.05}$/SBA-15 catalyst as a function of temperature in the presence of x Torr of CO in the gas phase (after subtraction of the gas-phase contribution). Four panels are provided, showing the traces recorded at 5 Torr (left), 10 Torr (center), and 50 Torr (right).

Table 5-5. Peak area of CO/Cu from CO Adsorption on $CuPt_{0.05}$/SBA-15 for one cycle of heating and cooling, In-Situ IR Spectra vs. P(CO)

Temperature (K)	Pressure of CO (Torr)		
	5	10	50
295	8.01	5.43	5.3
395	1.72	1.92	1.8
495	0.44	1.09	0.8
395	2.84	1.08	2.3
295	13.75	4.51	6.1

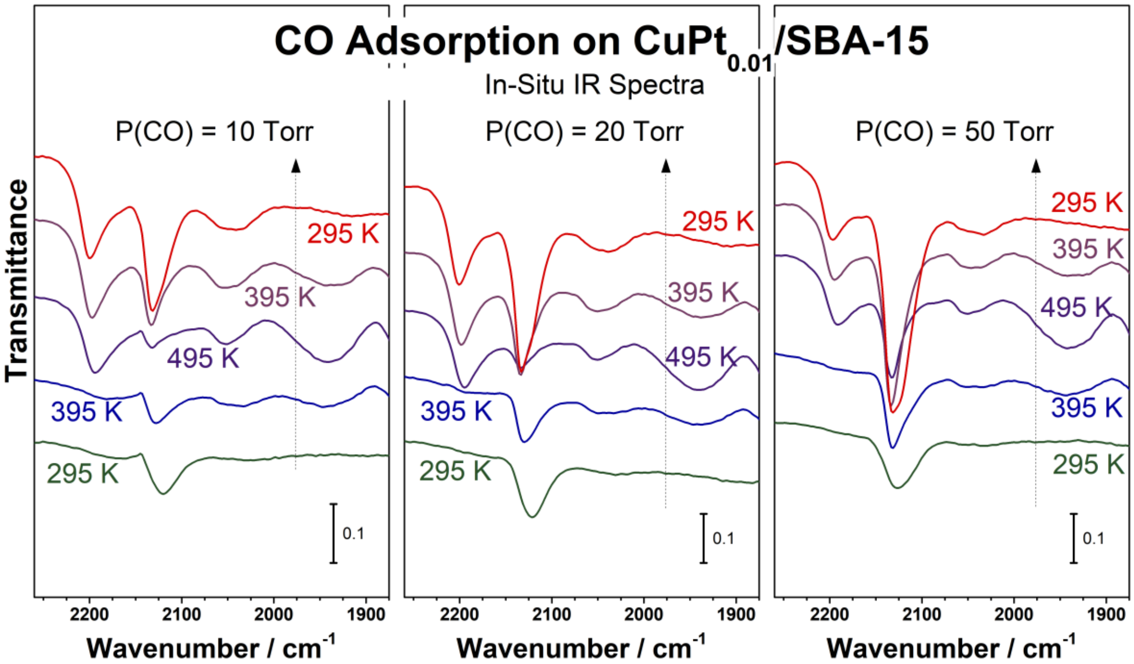

Figure 5-8. *In situ* IR spectra of CO adsorbed on CuPt$_{0.01}$/SBA-15 catalyst as a function of temperature in the presence of x Torr of CO in the gas phase (after subtraction of the gas-phase contribution). Four panels are provided, showing the traces recorded at 10 Torr (left), 20 Torr (center), and 50 Torr (right).

Table 5-6. Peak area of CO/Cu from CO Adsorption on CuPt$_{0.01}$/SBA-15 for one cycle of heating and cooling, In-Situ IR Spectra vs. P(CO)

Temperature (K)	Pressure of CO (Torr)		
	10	20	50
295	1.27	2.47	2.49
395	0.98	2.1	3.3
495	0.49	0.93	3.22
395	2.12	3.62	6.87
295	4.29	6.95	10.32

5.1.3 Results and Discussion on Thermodynamics

In this section, we only reported thermodynamics results for $CuPt_{0.1}$/SBA-15 and $CuPt_{0.005}$/SBA-15, since results from experiments with other samples appear to be unreliable and require further exploration. CO surface coverages were estimated by integration of the areas of the IR peaks, and reported in monolayers (ML) relative to the estimated saturation coverage (set to $\theta_{CO,sat}$ = 1 ML).

In detail, to start with, normalized peak areas were estimated in the following steps. For sample $CuPt_{0.1}$/SBA-15, a nonlinear curve fitting was performed with the peak area of CO/Cu as a function of pressure (under 295 K) as shown in Table 5-7. The function used for the fitting, developed on the basis of the need to first convert transmission into absorbance in the spectra, was $A = A_1 * \exp(-P/t_1) + y_0$, where A = Peak area of CO/Cu and P = pressure (bar). The resulting fitting parameters obtained were y_0 = 14.92716 ± 1.10323, A_1 = -15.12418 ± 1.34445, and t_1 = 0.01788 ± 0.00379. With all the information given above, the maximum A (Peak area of CO/Cu) was found to be 14.92716 ± 1.4435 when P = 4.0771 ± 0.4125 bar. Therefore, the maximum peak area was set to be 14.92, and the minimum peak area was set to be 0 for normalization, respectively. The coverage of CO (θ_{CO}) was then set using the normalized peak area (the same procedure was used for $CuPt_{0.005}$/SBA-15 in this section), and reported in Table 5-8. These CO coverage data were analyzed to develop isothermal curves of CO surface coverage of the $CuPt_{0.1}$/SBA-15 and $CuPt_{0.005}$/SBA-15 catalysts as a function of CO pressure (P_{CO}). The results are shown in Figure 5-9 and Figure 5-11: those symbols represent experimental values, whereas the solid lines are the best fits to Langmuir isotherm equation. The data are plotted in two modes: in the original θ_{CO} versus P_{CO} form (left panel), and in a linearized form to help extract the corresponding adsorption equilibrium constants (K_{ads}). The latter were then plotted in van't Hoff mode, that is, as $\ln(K°_{ads}) = \ln(K_{ads}P°_{CO})$ versus 1/T, to extract the appropriate thermodynamic parameters. In these calculations, the thermodynamics standard states were taken as $P°_{CO} = 1$ bar, $\theta°_{CO} = 0.5$ ML, and $\theta°_{empty} = 1 - \theta°_{CO} = 0.5$ ML, as typically used in cases where the adsorbates are presumed to be immobile.

Table 5-7. Peak area of CO/Cu from CO Adsorption on $CuPt_{0.1}$/SBA-15 at 295, 345, 395, 445, 495 K, In-Situ IR Spectra vs. P(CO).

	Pressure	295 K	345 K	395 K	445 K	495 K
Peak area	10 CO	6.87	3.44	1	0.42	0
	20 CO	12.54	7.38	3.4	1.61	0.96
	50 CO	14.23	9.73	4.55	2.09	1.19

Table 5-8. CO coverage (Normalized peak area obtained from Table 5-7) of CO/Cu from CO Adsorption on $CuPt_{0.1}$/SBA-15 at 295, 345, 395, 445, 495 K.

	Pressure (bar)	295 K	345 K	395 K	445 K	495 K
Peak area	1.33E-02	0.46	0.23	0.07	0.03	0.00
	2.67E-02	0.84	0.49	0.23	0.11	0.06
	6.67E-02	0.95	0.65	0.30	0.14	0.08

As indicated in Figure 5-10, $\Delta H^\circ_{ads,CO\text{-}atm} = -30.23$ kJ/mol and $\Delta S^\circ_{ads,CO\text{-}atm} = -60.15$ J/(mol K) were estimated from this analysis for CuPt$_{0.1}$/SBA-15.

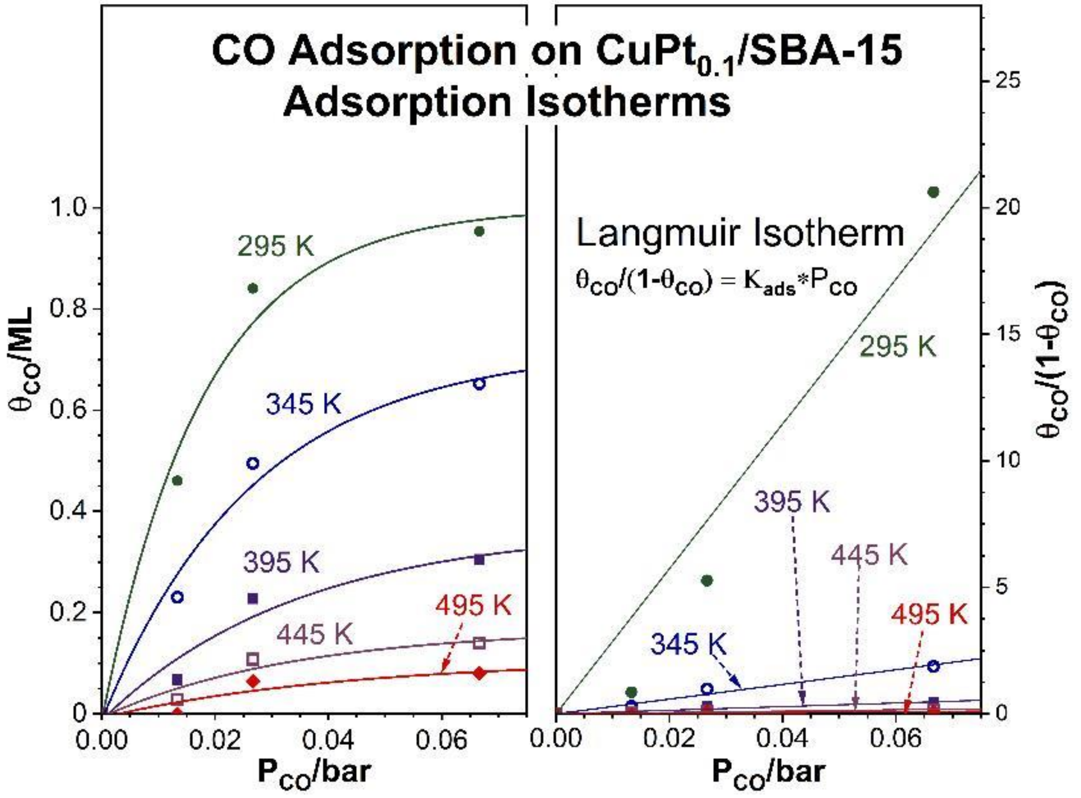

Figure 5-9. CO adsorption isotherms on 5 wt% CuPt$_{0.1}$/SBA-15 estimated from the area of the IR peaks of CO/Cu in data such as those shown in

Figure 5-6. The data are displayed both in their basic form, as CO coverage versus CO pressure (left), and in linearized form, using the Langmuir isotherm formulation (right).

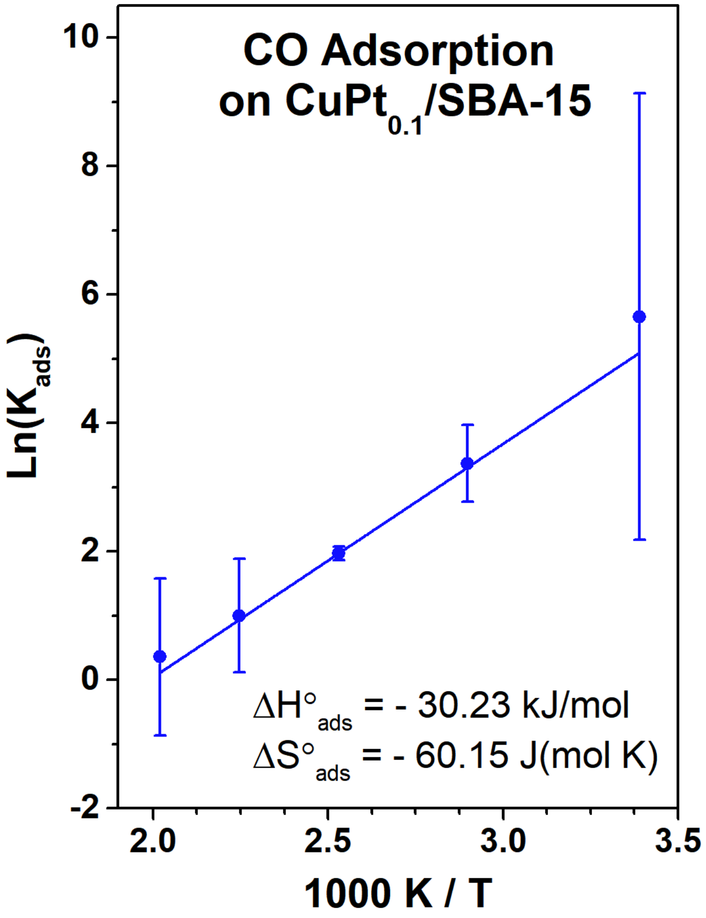

Figure 5-10. Van't Hoff plot of the equilibrium constants for the adsorption of CO on 5 wt% $CuPt_{0.1}$/SBA-15 (K_{ads}, the slope in the traces in the right panel of Figure 5-9) as a function of temperature, from which the values for the standard enthalpy and the standard entropy of adsorption were extracted.

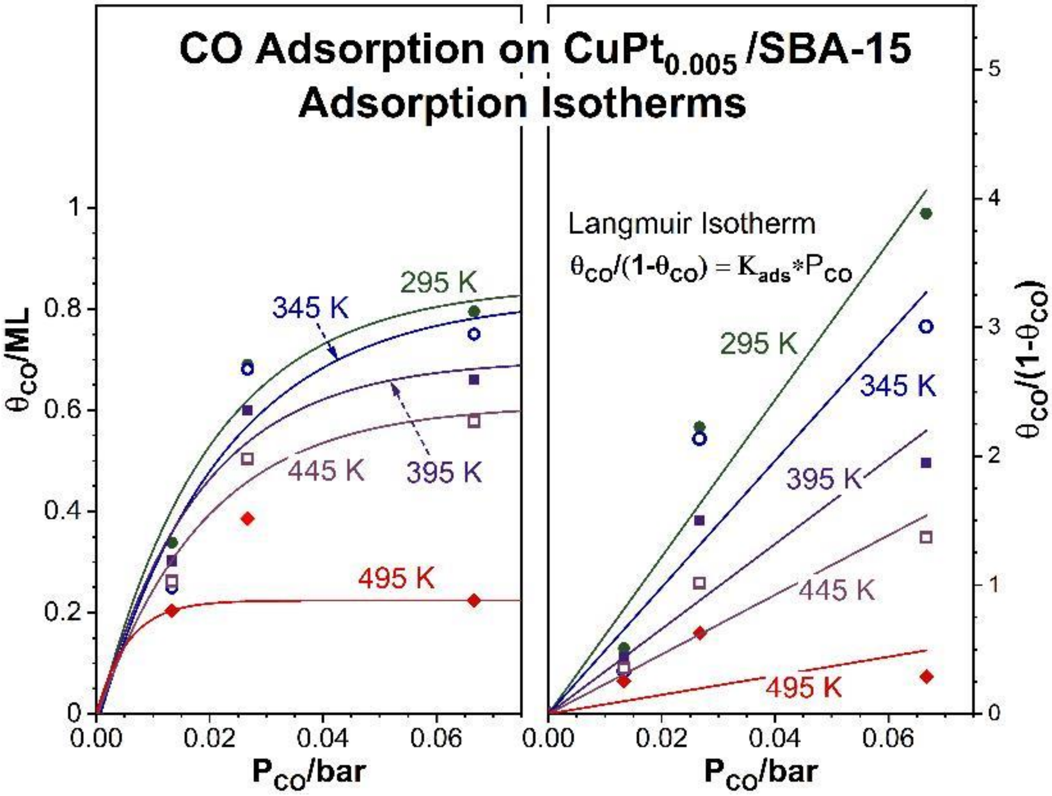

Figure 5-11. CO adsorption isotherms on 5 wt% $CuPt_{0.005}/SBA-15$ estimated from the area of the IR peaks of CO/Cu. The data are displayed both in their basic form, as CO coverage versus CO pressure (left), and in linearized form, using the Langmuir isotherm formulation (right).

As shown below in Figure 5-12, $\Delta H^\circ_{ads,CO\text{-}atm} = -15.80$ kJ/mol and $\Delta S^\circ_{ads,CO\text{-}atm} = -15.65$ J/(mol K) were estimated from this analysis for $CuPt_{0.005}/SBA-15$.

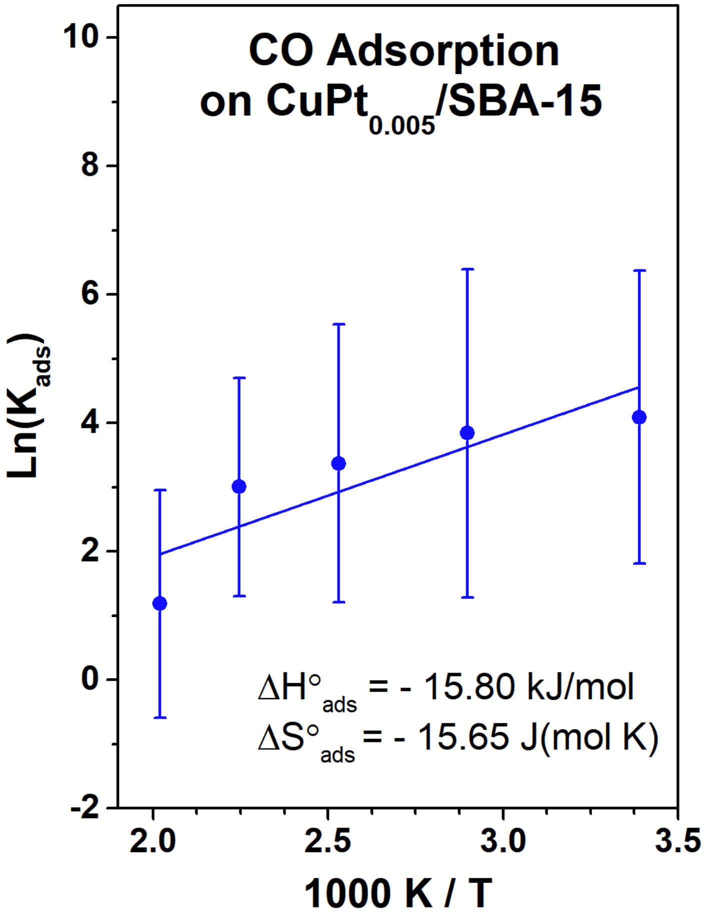

Figure 5-12. Van't Hoff plot of the equilibrium constants for the adsorption of CO on 5 wt% $CuPt_{0.005}$/SBA-15 (K_{ads}, the slope in the traces in the right panel of Figure 5-11) as a function of temperature, from which the values for the standard enthalpy and the standard entropy of adsorption were extracted.

With all that has been mentioned in this section, it should be noted that thermodynamic values reported here are approximate, as there are large errors due to the fact that they do not include coverage effects or the potential of the existence of different adsorption sites within the Cu NPs of the catalysts. Additionally, the subtraction of the gas phase contribution of CO could also have led to experiment errors.

5.2 Conclusion

In the first part of this chapter, due to the reduction of Cu_2O surface layer and the creation of additional metallic Cu sites available for CO uptake, it should be noted that the catalysts were not fully reduced under H_2. The growth of the peaks in the 2300 - 2400 cm^{-1} range due to CO_2, which is the product of CO oxidation, further supported this conclusion. In the second part of this chapter, a set of in situ IR results of $CuPt_x$/SBA-15 further confirm our conclusion that pre-treatment with H_2 did not fully reduce the catalyst by removing the Cu_2O layer present on the surface.

5.3 References

1. Han, T.; Lee, I.; Cao, Y.; Zhou, X.; Zaera, F., Thermodynamics of Carbon Monoxide Adsorption on Cu/SBA-15 Catalysts: Under Vacuum versus under Atmospheric Pressures. *The Journal of Physical Chemistry C* **2022,** *126* (6), 3078-3086.

2. Han, T.; Li, Y.; Cao, Y.; Lee, I.; Zhou, X.; Frenkel, A. I.; Zaera, F., In situ identification of surface sites in Cu–Pt bimetallic catalysts: Gas-induced metal segregation. *The Journal of Chemical Physics* **2022,** *157* (23), 234706.

Chapter 6 Thermodynamics of Carbon Monoxide Adsorption on Cu/SBA-15 Catalysts: In Vacuum versus Under Atmospheric Pressures

In this chapter, we studied the data from in situ infrared absorption spectroscopy experiments and estimated the thermodynamics properties of the adsorption of carbon monoxide on a copper-based catalyst. After comparing the energetics under a vacuum environment to in the presence of CO atmosphere, it has been found that the magnitude of enthalpy of adsorption is reduced by almost a factor of four in going from the first case to the second, from $\Delta H^\circ_{ads,vacuum}$ = -82 kJ/mol to $\Delta H^\circ_{ads,CO\text{-}atm}$ = -21 kJ/mol. In addition, isosteric analysis of the data demonstrated that the magnitude of the latter decreases in the low-coverage limit, to values below $\Delta H^\circ_{ads,CO\text{-}atm}$ = -18 kJ/mol, a trend on the contrary to what has been reported in other systems. These finding can be understood in terms of associated standard entropy of adsorption, which in the presence of gas phase CO was estimated at approximately $\Delta S^\circ_{ads,CO\text{-}atm} \sim -24$ J/(mol K), a value much smaller in magnitude than the standard entropy of CO condensation. The excess entropy of CO adsorption compared to that of CO condensation is attributed to additional phenomena induced by the gas-phase molecules, such as adsorbate displacement and adsorbate-assisted adsorption steps, which contribute to the excess entropy in the adsorbed state.

6.1 Introduction

Adsorption of reactants on the surface of the catalytic phase and desorption of products are crucial steps in nearly all chemical reactions promoted by solids. In numerous instances, these steps can determine the kinetics of the overall process. However, to date, limited information is available regarding the thermodynamics and kinetics of these steps under realistic conditions. Modern surface-science techniques, particularly temperature-programmed desorption (TPD), and more recently, the aid of quantum mechanics calculations, have provided general insight into the energetics of adsorbate bonding to surfaces in recent decades. The information obtained through these methods has proven to be invaluable, though it typically refers to the adsorption of molecules onto surfaces under vacuum conditions, often at low coverage levels. It is well-known that increasing coverages, as expected when in the presence of gases or a liquid phase[1], usually leads to a drastic reduction in adsorption energy. Additional effects on the adsorption−desorption process are also expected to be introduced by the gas or liquid phase itself, although this has not been discussed in the literature in much detail; in general, in situ studies of the kinetics and thermodynamics of adsorption in the presence of reactants are scarce[2-3]. Here in, we estimate the enthalpy and the entropy of the adsorption of carbon monoxide on copper catalysts, with emphasis on contrasting the behavior of this system under vacuum versus in the presence of the adsorbing gas. Carbon monoxide is a reactant in many major catalytic processes and a commonly used prototypical adsorbate, and copper catalysts are used for the hydrogenation of CO to methanol[4-8], and the low-temperature promotion of the water-shift reaction[9-11], among other processes. When a second transition metal is added in small amounts, to form so-called single-atom alloys (SAA)[12], copper can also be used as a selective catalyst for other reactions, for the hydrogenation of organic reactants with multiple unsaturations, for instance[13-18]. This latter application has been the motivation behind this study[19-20].

Our findings indicate that the thermodynamics of carbon monoxide (CO) adsorption on copper catalysts exhibit significant differences between the conditions of vacuum and in the presence of the gas phase. In particular, the magnitude of both the enthalpy and the entropy of adsorption are reduced drastically upon the addition of gas-phase CO. We interpret this change as the result of the incorporation of new steps by the free molecules, including adsorbate displacement and adsorbate-assisted adsorption steps. We propose that the changes seen here and the explanation provided may be quite general and apply to many reversible adsorption processes.

6.2 Results and Discussion

The *in situ* infrared absorption spectroscopy (IR) studies reported below were carried out in a transmission IR cell reported in previous publications,[21-24] a standard setup similar to that seen in many other laboratories.[25-30] The catalyst, a 5 wt% Cu/SBA-15 solid, was prepared by incipient wetness impregnation (using copper nitrate),[19] and made into a pellet that was placed in the center of the IR cell and pretreated before use by exposing it to a H_2 atmosphere (200 Torr) at 625 K for 3 h. For the experiments involving an equilibrium with gas-phase CO, the IR cell was filled with the desired pressure of carbon monoxide, and the IR spectra recorded *in situ* in the presence of the gas as the sample was heated and cooled to evaluate the temperature dependence of the adsorption equilibrium; three cycles were carried out to corroborate that the CO surface coverages measured by the IR peaks correspond to equilibrium states. In the case of the low temperature adsorption measurements under vacuum, the catalyst was exposed to 50 Torr of CO for 0.5 h, after which the cell was evacuated for 10 min and the IR spectra recorded from 125 to 475 K at 20 K intervals as the sample and cell were warmed up. All spectra were acquired with a resolution of 2 cm^{-1} by average the data from 16 scans and corrected using background spectra obtained under the same condition before adsorption.

The desorption of adsorbed carbon monoxide on the Cu/SBA-15 catalyst was first probed as a function of temperature under vacuum. The corresponding infrared absorption spectroscopy data are shown in Figure 6-1. The main peak seen at 2124 cm^{-1}, visible from 125 K to approximately 350 K, is assigned to CO adsorption on metallic Cu atop site on the basis of previous reports[31-35]; a brief discussion of this assignment is provided later. At low temperatures, below 150 K, an additional feature is detected on the high-frequency side at approximately 2160 cm^{-1}, most likely from adsorption of CO on oxidized copper sites, and a weaker broad double feature is also seen in the 1950 to 2050 cm^{-1} range at intermediate temperatures (205 - 325 K), the origin of which we do not understand at the present time. Focusing on the CO bonded to metallic copper, the intensity of the peak was followed versus annealing temperature to extract information about the energetics of the adsorption (Figure 6-1, right panel). It was determined that the desorption rate peaks at approximately 245 K, a result roughly consistent with that seen in temperature programmed desorption (TPD) experiments on Cu single crystals once the differences in heating rate are considered. Using Redhead's analysis[36], an estimated value of $A = 1 \times 10^{15}$ s^{-1} for the pre-exponential factor, and a heating rate of 20 K in 10 min, the activation energy for CO desorption from this Cu/SBA-15 catalyst, which can also be associated with the enthalpy of adsorption, is estimated to be $E_a = -\Delta H°_{ads,vacuum} = 82$ kJ/mol, a value in the range of what has been reported in the past for stepped Cu single crystals[37].

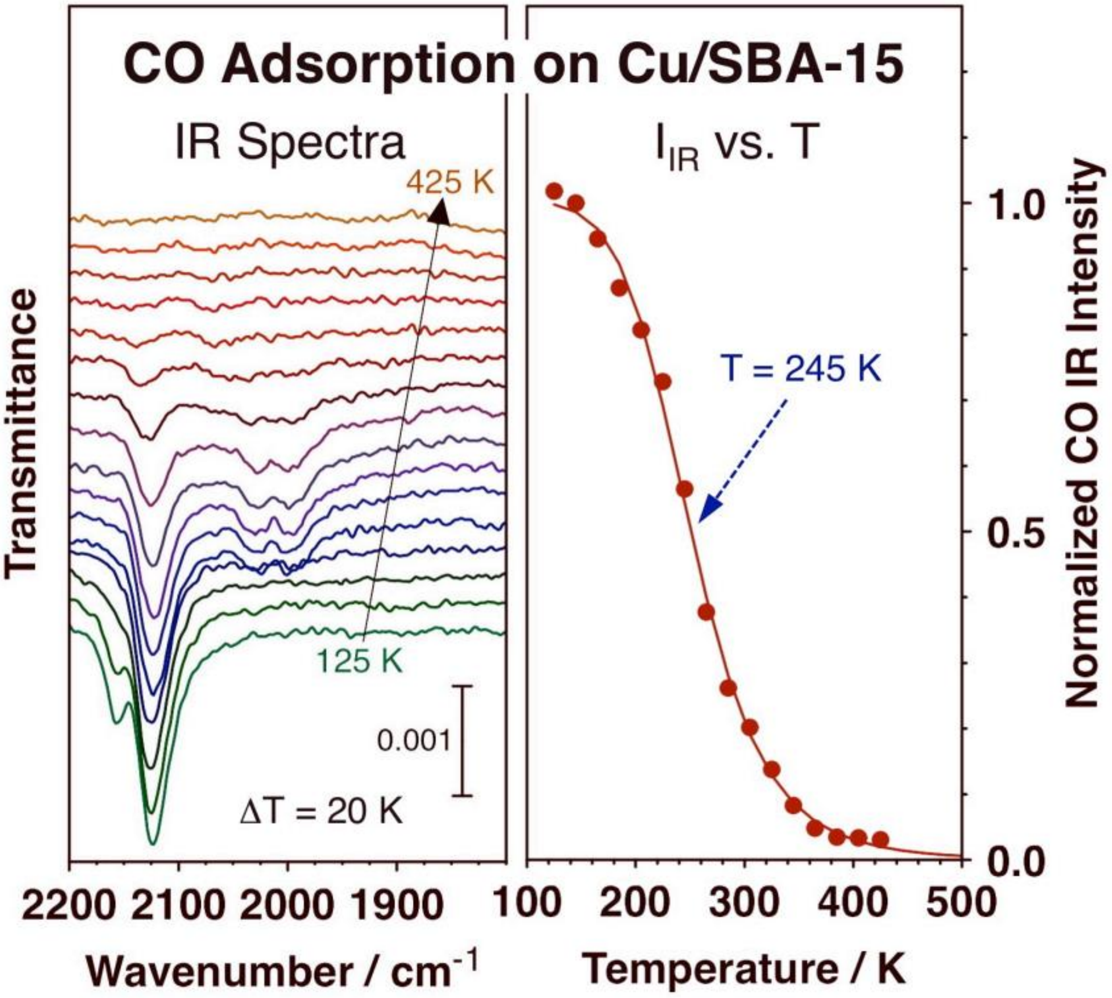

Figure 6-1. Left: Transmission infrared absorption (IR) spectra in the C–O stretching region for CO adsorbed on a 5 wt% Cu/SBA-15 catalyst as a function of temperature during heating under vacuum, after initial adsorption at 125 K in 50 Torr CO. Right: Normalized peak intensity for the main Cu–CO feature in the spectra at 2124 cm^{-1} as a function of temperature, together with a fit to a sigmoidal curve.

Next, CO adsorption was probed in situ in the presence of a CO atmosphere. Typical IR data recorded in those experiments are shown in Figure 6-2: the left panel shows the C–O stretching region for both the catalyst in the presence of the gas (dark traces, 50 Torr in this case) and the blank experiments with CO gas only, with the catalyst pellet removed (light traces). The gas-phase molecules are clearly detected, seen as the expected two broad features between 2000 and 2250 cm^{-1} due to the different rotational levels within the main C–O stretching vibrational mode. Nevertheless, additional signal, in the form of a sharper peak at about 2124 cm^{-1}, is visible in these spectra assignable to CO adsorbed on Cu. The right panel of Figure 6-1 displays the same spectra after subtracting the gas-phase contribution: a clear peak remains at 2124 cm^{-1} corresponding to CO bonded on atop sites on the surface of the metallic Cu nanoparticles of the catalyst. The peaks in the 2300 - 2400 cm^{-1} region correspond to gas-phase CO_2, from both incomplete purging of the IR beam path (ambient air contains some level of CO_2) and oxidation of CO (see below).

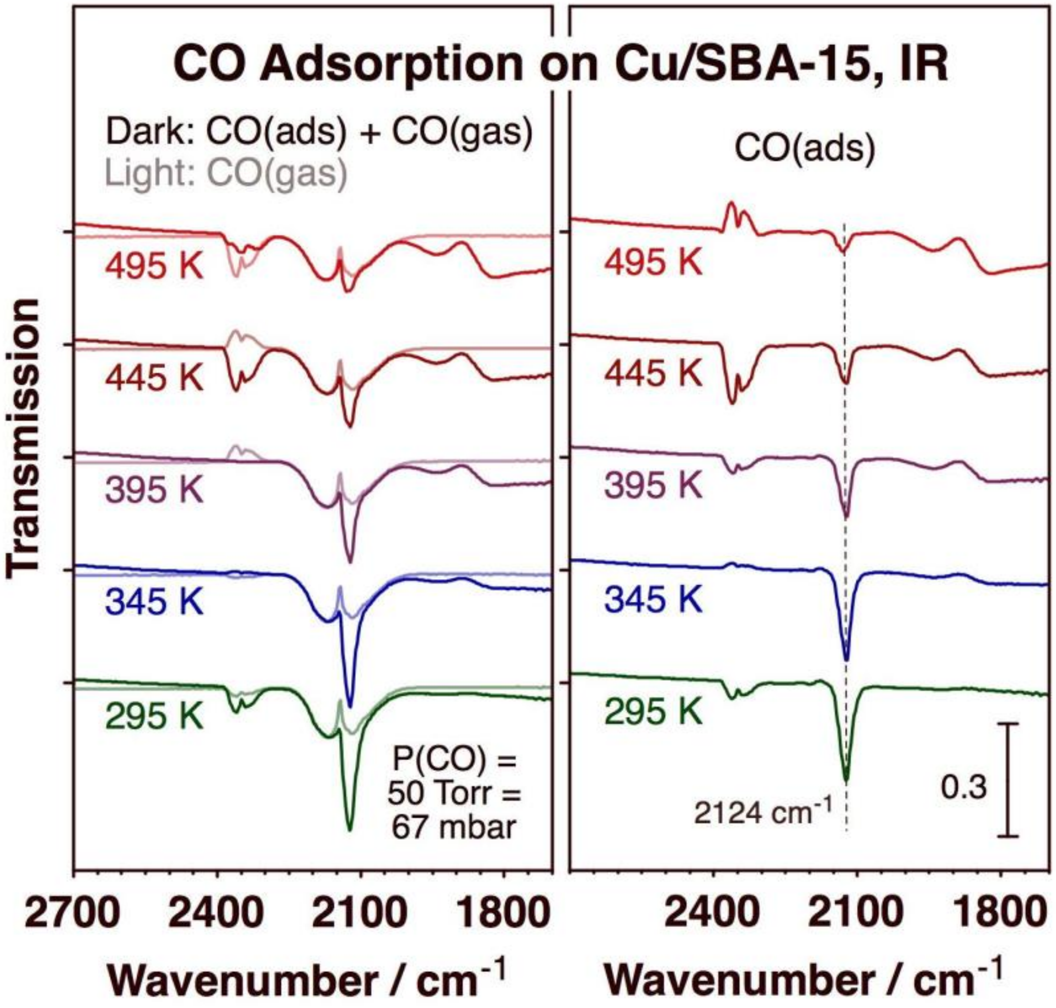

Figure 6-2. *In situ* IR spectra in the C–O stretching region for a 5 wt% Cu/SBA-15 catalyst exposed to 50 Torr (67 mbar) of carbon monoxide as a function of catalyst temperature. Left: raw data recorded in the presence of the gas-phase CO (dark traces), together with reference spectra obtained in the absence of the catalyst, for the gas alone (light traces). Right: Spectra for the adsorbed CO, obtained via subtraction of the corresponding traces shown in the right panel. The peak highlighted at 2124 cm^{-1} corresponds to CO adsorbed on atop sites on the surface of the copper nanoparticles.

The adsorption of CO reported in Figure 6-2 is reversible. In order to confirm this, repeated heating and cooling cycles were performed *in situ* the presence of the same CO gas atmosphere. The resulting data are exemplified by the plots reported in Figure 6-3, with 100 Torr of CO in that case. It should be noted that initial CO adsorption at room temperature was minimal (bottom trace in left panel of Figure 6-3); in spite of the *in situ* H_2 pretreatment performed before the use of the catalyst, it appears that the Cu nanoparticles retain an oxide layer that prevents binding of the adsorbate. Luckily, CO is itself a strong reducing agent that helps remove such oxide layer: a significant increase in CO uptake is seen in the first heating cycle as a temperature of 495 K is reached, in conjunction with the generation of CO_2 gas product of CO oxidation with the oxygen atoms of the oxidized Cu surface (Figure 6-1, left panel). After that sequence of events, it can be seen from Figure 6-3 that the IR peak associated with CO bonded to metallic Cu increases and decreases in size reversibly as subsequent cooling and heating cycles are followed. The peak intensities measured at any of the given temperatures are quite similar in all cases, evidencing the reversibility of the process.

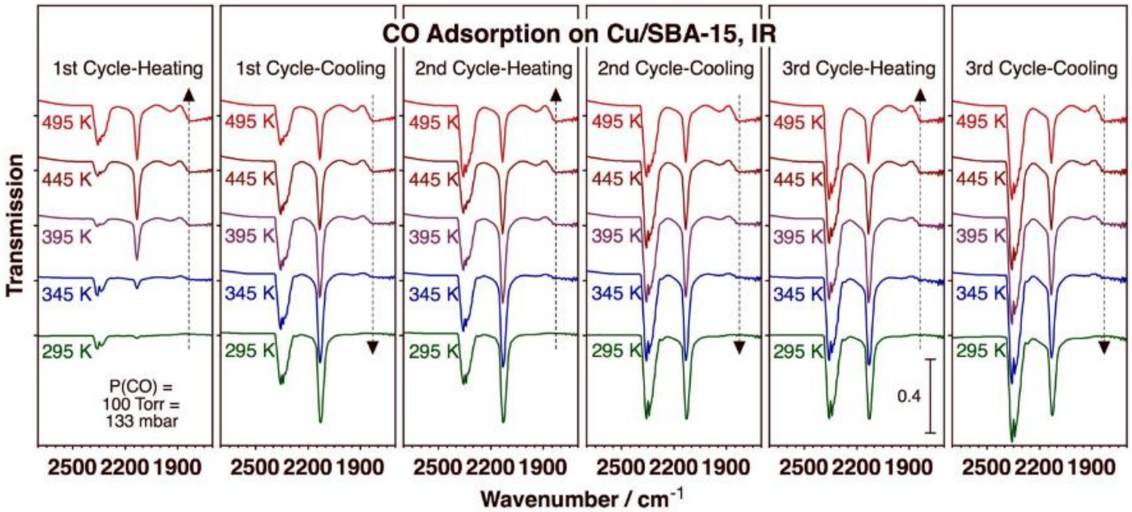

Figure 6-3. *In situ* IR spectra in the C–O stretching region for a 5 wt% Cu/SBA-15 catalyst exposed to 100 Torr (133 mbar) of carbon monoxide as a function of catalyst temperature. Shown are the data for three consecutive heating and cooling cycles to highlight the reversibility of the adsorption.

Data such as those reported in Figure 6-2 and Figure 6-3 were analyzed to develop isothermal curves of CO surface coverage (θ_{CO}) on the Cu/SBA-15 catalyst as a function of CO pressure (P_{CO}). The results are shown in Figure 6-4: the symbols correspond to the experimental values, whereas the solid lines originate from the best fits to the Langmuir isotherm equation. The data are plotted in two modes, in the original θ_{CO} versus P_{CO} form (left panel, with CO coverages reported in monolayers, ML: 1 ML corresponds to surface saturation), and also in a linearized form to help extract the corresponding adsorption equilibrium constants (K_{ads}). The latter were then plotted in van't Hoff mode, that is, as Ln(K_{ads}) versus 1/T, to extract the appropriate thermodynamic parameters. As indicated in Figure 6-5, values of $\Delta H^{\circ}_{ads,CO\text{-}atm} = -21.3$ kJ/mol and $\Delta S^{\circ}_{ads,CO\text{-}atm} = -23.7$ J/(mol K) were estimated from this analysis.

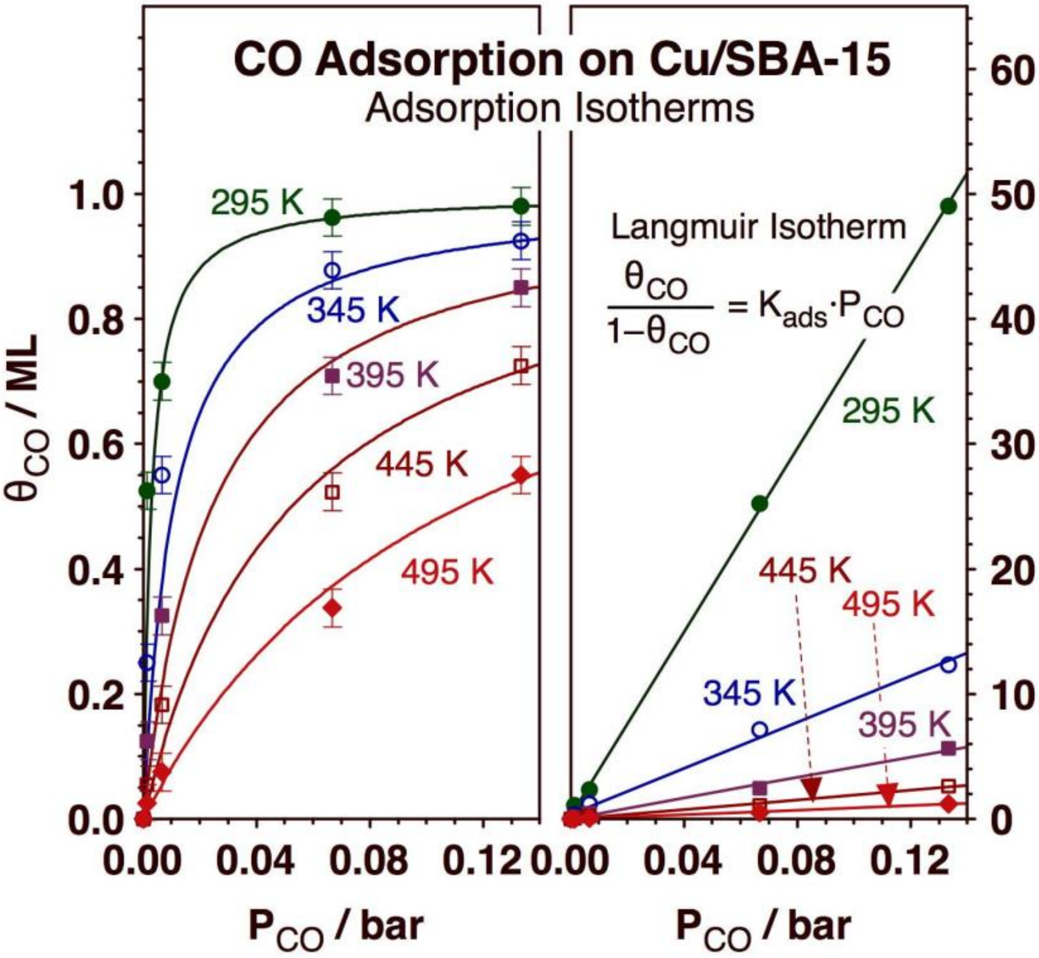

Figure 6-4. CO adsorption isotherms on 5 wt% Cu/SBA-15 estimated from the intensity of the IR peaks in data such as those shown in Figure 6-2 and Figure 6-3. The data are displayed both in their basic form, as CO coverage versus CO pressure (left), and in linearized form, using the Langmuir isotherm formulation (right).

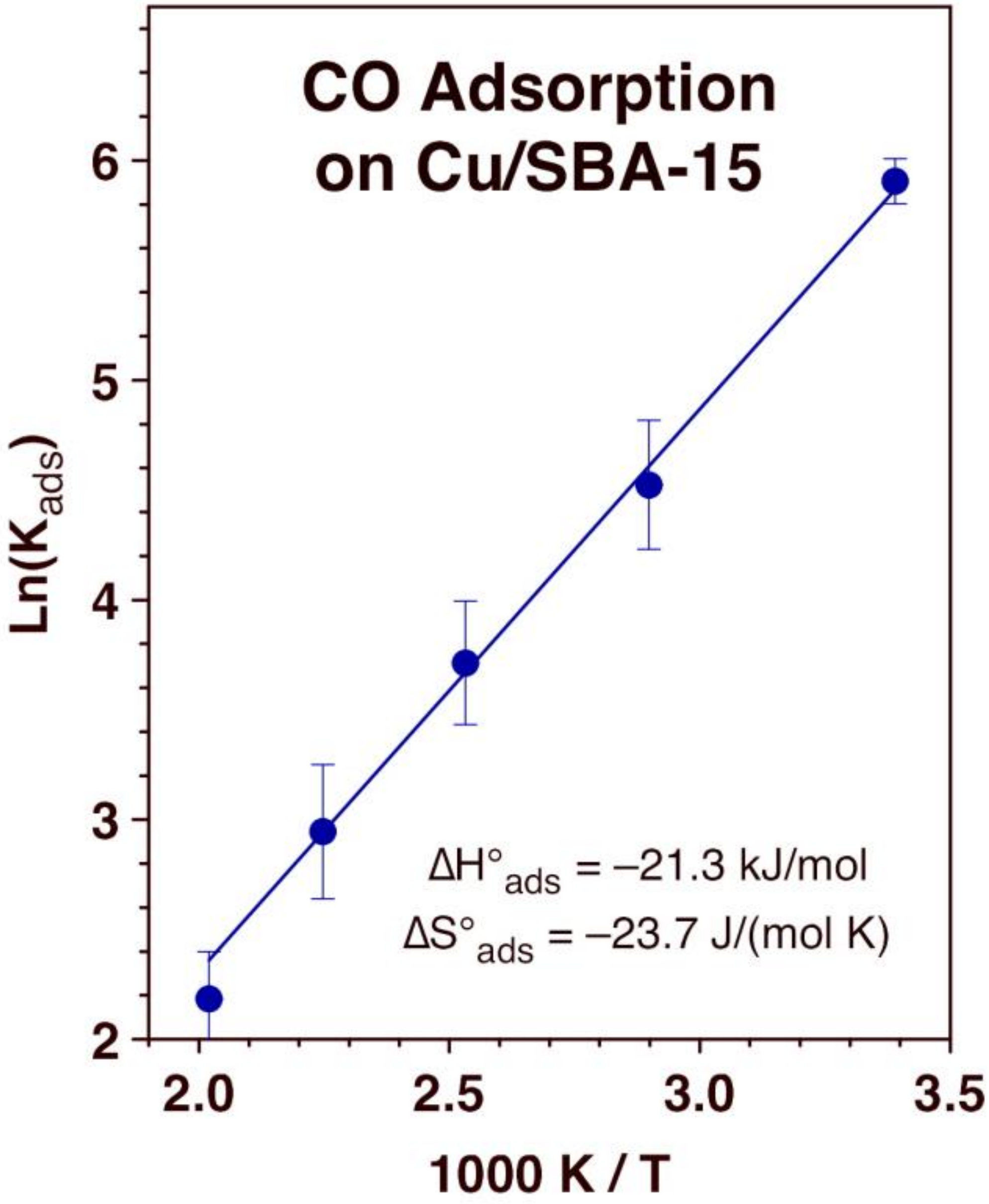

Figure 6-5. Van't Hoff plot of the equilibrium constants for the adsorption of CO on 5 wt% Cu/SBA-15 (K_{ads}, the slope in the traces in the right panel of Figure 6-4) as a function of temperature, from which the values for the standard enthalpy and the standard entropy of adsorption were extracted.

Two issues need to be considered when interpreting the thermodynamic data reported above. First, the intensity of the IR peak due to the adsorbed CO is in many cases not linearly dependent on the surface coverage of the adsorbate, as it has implicitly been assumed here. Instead, that intensity tends to grow at a lesser rate in the high coverage range because of intermolecular dipole-dipole and other interactions[38-40], although the effect is less pronounced with supported metal nanoparticles because of the higher degree of disorder involved. Second, because of those inter-adsorbate interactions, the adsorption energy of CO on metals tends to change with surface coverage, typically dropping considerably close to monolayer saturation. In order to check on these potential dependences of adsorption energy on coverage, an alternative isosteric analysis of the data was performed in the limit of low coverages. For that, the pressures of CO required to reach a certain pre-established coverage were estimated via linear interpolation of the experimental data (a linear dependence is expected in the low-coverage limit on the basis of the Langmuir isotherm equation), and plotted versus temperature in linearized form (as $\mathrm{Ln}(P_{CO})$ versus 1/T). The left panel of Figure 6-6 shows the resulting isosters for θ_{CO} = 0.05, 0.1, and 0.2, and 0.5 ML, and the right panel the thermodynamic parameters calculated from that analysis. For θ_{CO} = 0.5 ML, the enthalpy of adsorption is estimated at $\Delta H_{ads,CO\text{-}atm}(\theta_{CO} = 0.5\ \mathrm{ML}) \sim -28$ kJ/mol, much smaller in magnitude than that reported above for the same coverage under vacuum, $\Delta H_{ads,vacuum}(\theta_{CO} = 0.5\ \mathrm{ML}) \sim -82$ kJ/mol. Interestingly, it was found that the magnitudes of both the enthalpy and the entropy of the adsorption are lower, not higher as usually reported, at low coverages (Figure 6-6, right). A third possible approach to analyze the CO adsorption data is in isobaric form. The corresponding plots of Ln[θ_{CO}/(1- θ_{CO})] vs. 1/T are displayed in Figure 6-7. Values of $H°_{ads,CO\text{-}atm}$ = –21.9 ± 2.0 kJ/mol and $\Delta S°_{ads,CO\text{-}atm}$ = –22.8 ± 6.0 J/(mol K) were estimated from the slopes of that figure.

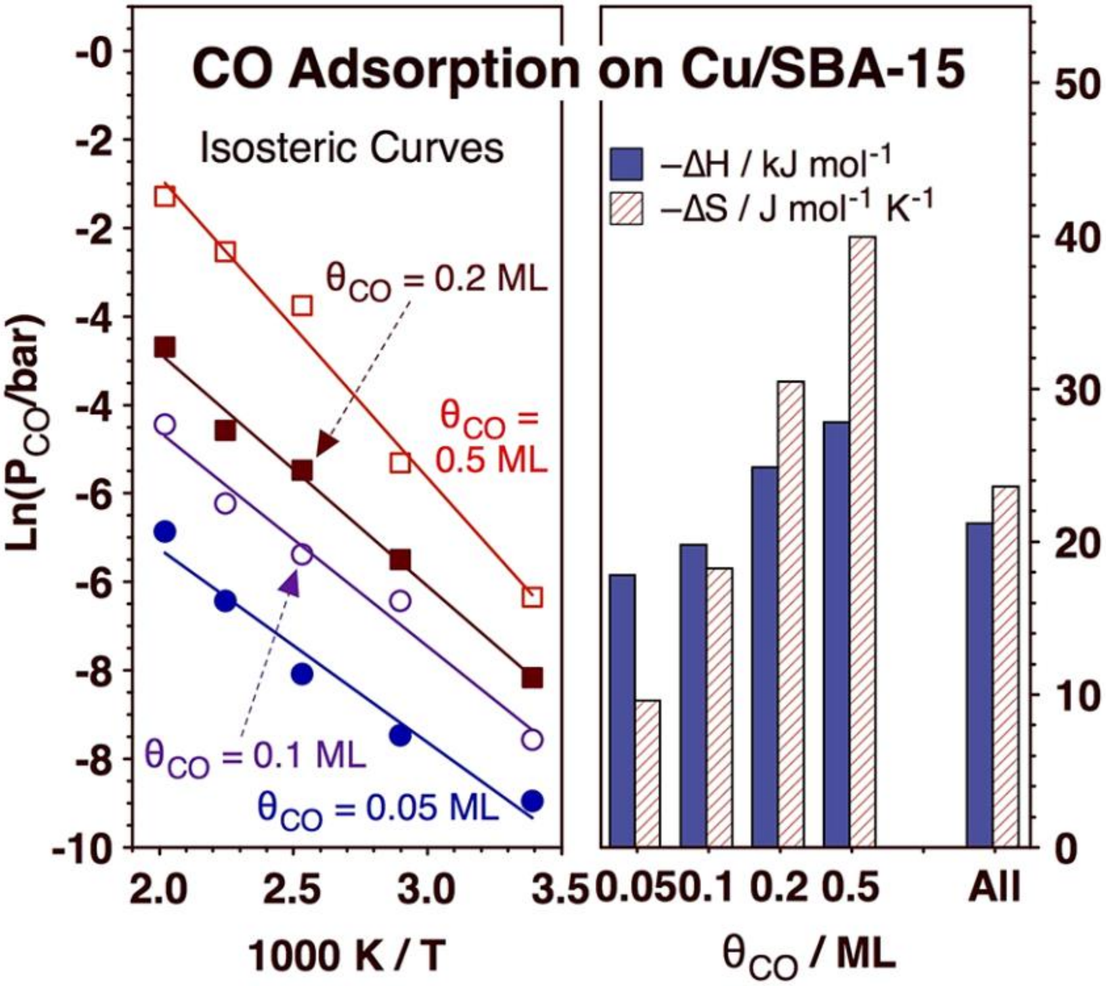

Figure 6-6. Left: Isosteric plots of CO pressure versus temperature, in Van't Hoff form, for four low values of the CO coverage (θ_{CO} = 0.05, 0.1, 0.2 and 0.5 ML). Right: standard enthalpy and standard entropy of adsorption estimated from the plots in the left panel.

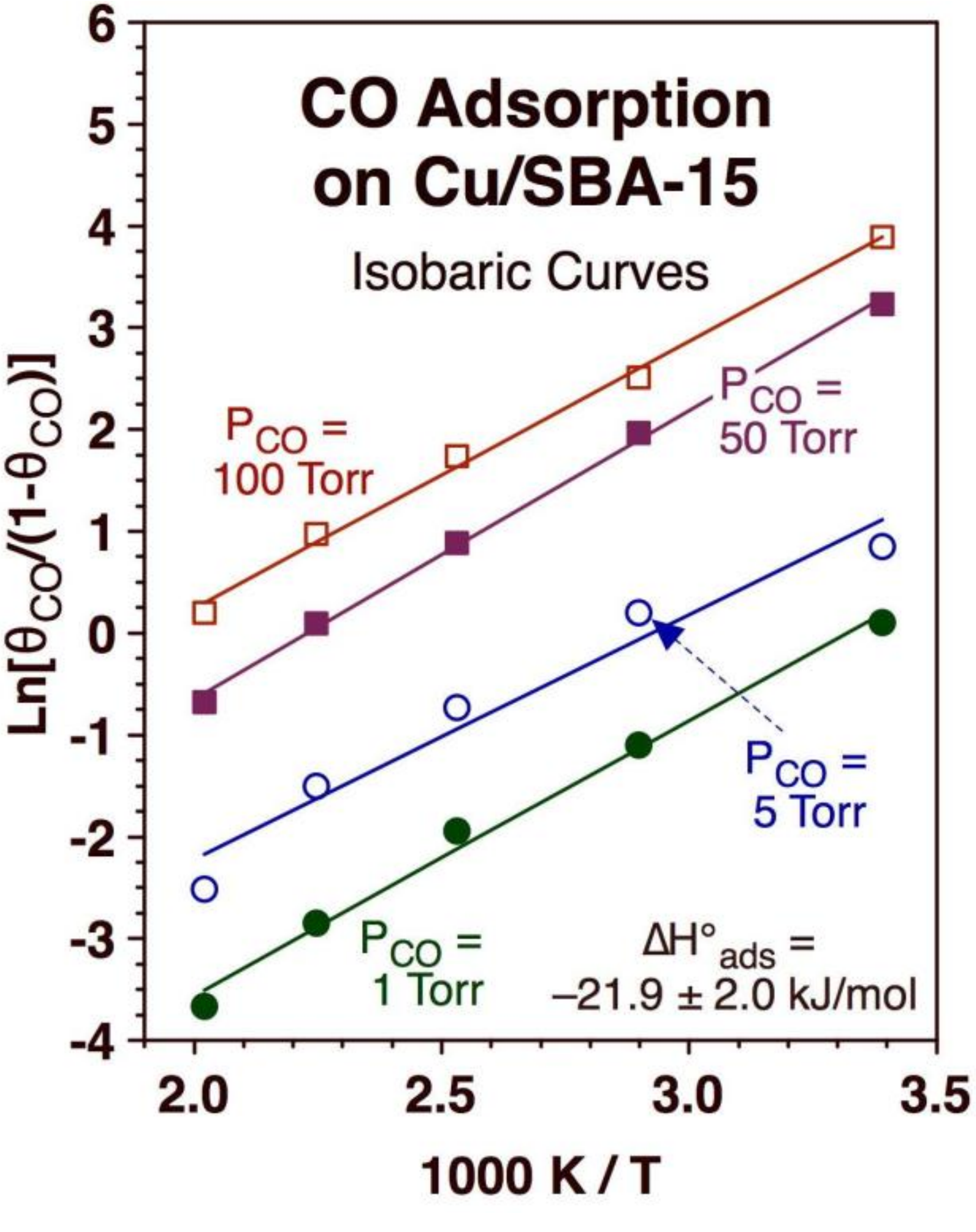

Figure 6-7. Isobaric plots of CO coverage versus temperature, in Van't Hoff form, for several CO pressures (P_{CO} = 1, 5, 50 and 100 Torr).

In this section, we start by briefly discussing our assignment of the main IR band at 2124 cm^{-1} seen in the spectra reported above to CO adsorbed on atop sites of metallic Cu, as there has been some discussion in the literature about such assignment, which is not straightforward.[41] Certainly, the C–O stretching frequency of carbon monoxide adsorbed on atop sites of copper single-crystal surfaces is typically below 2100 cm^{-1};[41-45] features in the spectra at higher frequencies have been assigned to CO bonding to oxidized Cu atoms[32, 46]. Nevertheless, higher frequencies are seen on stepped and kinked metallic Cu surfaces[47], and also on supported Cu catalysts[31-34, 48-49]. We here put forward two main arguments for why we believe that the peak seen at 2124 cm^{-1} in our data corresponds to adsorption on metallic copper. First, we are confident that our catalyst is fully reduced in the experiments carried out in the presence of a CO atmosphere. The catalyst was always pretreated in H_2 *in situ* before each experiment, but that sometimes may not be sufficient to fully reduce the Cu nanoparticles in the supported catalyst; a thin layer of an oxide may be still retained on the surface after that. However, carbon monoxide is itself an excellent reducing agent, and the data in Figure 6-3 show that, indeed, it is capable of removing any remaining oxygen from the Cu surface upon heating to high (495 K) temperatures; witness the formation of gas-phase carbon dioxide, as indicated by the IR features in the 2300 - 2400 cm^{-1} range, and the subsequent increase in CO uptake on the surface. Our second argument relates to the thermal stability of the adsorbed CO under vacuum, as indicated by the data in Figure 6-1: the CO associated with the 2124 cm^{-1} peak remains bounded to the catalyst until approximately 245 K, whereas the second feature seen at 2160 cm^{-1} identified with the weaker adsorption on oxidized Cu goes away by 150 K.

The adsorption energetics of CO on the Cu/SBA-15 catalyst was first probed under vacuum by performing a temperature-programmed experiment using IR for surface coverage determination. The data in Figure 6-1 indicate that the CO desorption rate peaks at about 245 K, which corresponds to an adsorption enthalpy of approximately $\Delta H_{ads,vacuum} = -82$ kJ/mol. This value is consistent with results obtained in the past with single crystals, with the caveat that the CO adsorption energy is highly dependent on surface coverage. For instance, a value of $E_{des} \sim -\Delta H_{ads,vacuum} = 84$ kJ/mol has been reported for the zero-coverage limit of the adsorption of CO on the atop step-edge sites of Cu(410).[37] Earlier reported data are also in the appropriate energy range, albeit with lower values for flat terraces: $E_{des} \sim 50$ to 55 kJ/mol was reported for both CO/Cu(111)[50] and CO/Cu(110)[51] for $\theta_{CO} < 1/3$ ML, and CO desorption from the steps in defective Cu(110) peaks at 205 K, a temperature equivalent to $E_{des} \sim 60$ kJ/mol.[47]

The equilibrium enthalpy of adsorption for CO on Cu/SBA-15 under an atmosphere of gas-phase CO turns out to be much lower in magnitude. Indeed, the isothermal adsorption data reported in Figure 6-4 and Figure 6-5 yielded an adsorption enthalpy value of $\Delta H_{ads,CO\text{-}atm} = -21.3$ kJ/mol, about a fourth of the value measured under vacuum. It could be argued that the difference originates from differences in surface coverage, but the isosteric analysis reported in Figure 6-6 indicates that this is not the case; if anything, the magnitude of the adsorption enthalpy decreases somewhat when approaching the low CO coverage limit. The isobaric plot in Figure 6-7 further confirms these results.

It may be worth asking if the ΔH_{ads} values obtained here for CO adsorption on Cu/SBA-15 in the presence of gas-phase CO make sense. Unfortunately, because of the weak adsorption energy involved, attempts to detect reversibly-bonded CO on Cu under a CO atmosphere with model systems, on Cu single-crystal surfaces and by using modern surface-science instrumentation, have not been successful; both infrared absorption[45] and atmospheric-pressure X-ray photoelectron spectroscopy (AP-XPS)[52] experiments with Pt-doped Cu could only reach CO pressures of up to 0.1 Torr, and could therefore only see the CO bonded to Pt sites. On the other hand, a couple of early reports on CO adsorption on supported Cu catalysts are consistent with our results. Using Cu/SiO2 catalysts, Kohler and coworkers reported heats of adsorption on metallic copper surfaces approaching a value of $\Delta H_{ads,CO\text{-}atm} \sim -22$ kJ/mol at coverages close to saturation,[32] essentially the same as what we have measured here. They did also report a CO coverage dependence of that parameter, with higher magnitudes for the adsorption energy at lower coverages (a trend opposite to that seeing by us in Figure 6-6), but this effect was the most pronounced with catalysts with high Cu loadings (>6 wt%), and minimal for Cu loadings below 4 wt%. In a more recent report, Dandekar et al. reported $\Delta H_{ads,CO\text{-}atm} = -20.1$ kJ/mol for CO adsorption on the metallic sites of a 5.1 wt% Cu/SiO2 catalyst,[33] again in good agreement with our results. It does appear that the severe reduction in CO adsorption energy observed on Cu catalysts when transitioning from vacuum to an atmosphere of CO is real.

What remains to be discussed here is an explanation for the difference. For that, we investigate the entropy of the adsorption processes, which has not been reported before but that we were able to extract from our data: values of $\Delta S^\circ_{ads,CO\text{-}atm} = -23.7$ and -22.8 J/(mol K) were obtained from the isothermal and isobaric analysis in Figure 6-5 and Figure 6-7, respectively. For comparison, the standard entropy of CO vaporization (the negative of the standard entropy of condensation) at the boiling point of CO ($T^\circ_b = 81.6$ K) is $\Delta S^\circ_{vap,81.6\,K} = -\Delta S^\circ_{cond,81.6\,K} = 74$ J/(mol K).[53] If we assume that the liquid remains fully frozen and that only the heat capacity of CO gas contributes to the entropy of vaporization change in transitioning from the boiling point to room temperature (admittedly an extreme approximation), the standard entropy of vaporization at room temperature is estimated at $\Delta S^\circ_{vap,298K} = -\Delta S^\circ_{cond,298\,K} \leq 111$ J/(mol K).[53] The fact that the magnitude of the adsorption entropy determined in our studies is so much lower than that or the CO condensation indicates that there is an entropy deficit in the former process beyond that related to immobilization of CO molecules on the surface. Stated a different way, the entropy of the adsorbed CO is larger than that expected for CO fully anchored on the solid surface. We suggest that such excess may reflect a certain degree of 2D mobility of the adsorbed CO within the surface, perhaps because of a relatively low barrier for surface diffusion. In that context, it is interesting to note that, according to the data in Figure 6-6, the magnitude of the adsorption entropy decreases significantly at low coverages, presumably because there is more room on the surface for the few CO molecules on the surface to diffuse around without the hindrance of other adsorbates. It is also possible that additional entropy is introduced by the presence of gas-phase CO because of possible adsorbate displacement by incoming molecules[54-56] and/or adsorbate-assisted desorption[57-60] steps, as seen in other systems. Both these processes can add degrees of disorder, and hence entropy, to the CO-covered surface. Note that the same argument does not hold for CO desorption in vacuum environments: according to transition state theory, a pre-exponential factor of $A = 1 \times 10^{15}\ s^{-1}$ for that process (as typically assumed) amounts to an increase in entropy upon desorption at room temperature of $\Delta S^{\ddagger}_{des,298\ K} = 43$ J/(mol K), and if the value of $A = 1 \times 10^{19}\ s^{-1}$ reported by Kokaji et al. for CO desorption from Cu(410) is used, $\Delta S^{\ddagger}_{des,298\ K} \sim 120$ J/(mol K). Clearly, low desorption entropies appear to be unique to processes taking place under atmospheric pressures of the adsorbing gas. This difference may explain the large reductions in desorption enthalpies seen in going from vacuum to atmospheric pressures, and it is likely to be general, not only applicable to the CO adsorption on Cu/SBA-15 but also to most reversible adsorption processes.

6.3 Conclusion

In this study, the thermodynamics of the adsorption of CO on the metal surface of a Cu/SBA-15 catalyst was contrasted in two different environments, under vacuum versus in the presence of atmospheric pressures of CO. Interestingly, marked differences were seen. Specifically, the enthalpy of adsorption was estimated to vary from $\Delta H^{\circ}_{ads,vacuum} = –$

82 kJ/mol to $\Delta H^\circ_{ads,CO\text{-}atm}$ ~ – 21 kJ/mol. This difference could not be explained by coverage effects, as isosteric calculations in the low CO surface coverage limit indicated that the enthalpy of CO adsorption actually decreases (instead of increasing, as seen in many other systems) as the coverage decreases. Instead, we explain the change on the basis of entropic effects introduced by the presence of CO gas such as adsorbate displacement and adsorbate-assisted adsorption steps.

6.4 Reference

1. Schumacher, N.; Boisen, A.; Dahl, S.; Gokhale, A. A.; Kandoi, S.; Grabow, L. C.; Dumesic, J. A.; Mavrikakis, M.; Chorkendorff, I., Trends in low-temperature water–gas shift reactivity on transition metals. *Journal of Catalysis* **2005,** *229* (2), 265-275.

2. Davies, J. C.; Nielsen, R. M.; Thomsen, L. B.; Chorkendorff, I.; Logadóttir, Á.; Lodziana, Z.; Nørskov, J. K.; Li, W. X.; Hammer, B.; Longwitz, S. R.; Schnadt, J.; Vestergaard, E. K.; Vang, R. T.; Besenbacher, F., CO Desorption Rate Dependence on CO Partial Pressure over Platinum Fuel Cell Catalysts. *Fuel Cells* **2004,** *4* (4), 309-319.

3. Johansson, M.; Lytken, O.; Chorkendorff, I., The sticking probability for H2 in presence of CO on some transition metals at a hydrogen pressure of 1bar. *Surface Science* **2008,** *602* (10), 1863-1870.

4. Nix, R. M.; Rayment, T.; Lambert, R. M.; Jennings, J. R.; Owen, G., An in situ X-ray diffraction study of the activation and performance of methanol synthesis catalysts derived from rare earth-copper alloys. *Journal of Catalysis* **1987,** *106* (1), 216-234.

5. Nerlov, J.; Sckerl, S.; Wambach, J.; Chorkendorff, I., Methanol synthesis from CO2, CO and H2 over Cu(100) and Cu(100) modified by Ni and Co. *Applied Catalysis A: General* **2000,** *191* (1), 97-109.

6. Yang, R. Q.; Gai, X. K.; Xing, C.; Mao, J. W.; Lv, C. X., Performance of Cu-Based Catalysts in Low-Temperature Methanol Synthesis. *Advanced Materials Research* **2014,** *1004-1005*, 1623-1626.

7. van de Water, L. G. A.; Wilkinson, S. K.; Smith, R. A. P.; Watson, M. J., Understanding methanol synthesis from CO/H2 feeds over Cu/CeO2 catalysts. *Journal of Catalysis* **2018,** *364*, 57-68.

8. Zhu, J.; Su, Y.; Chai, J.; Muravev, V.; Kosinov, N.; Hensen, E. J. M., Mechanism and Nature of Active Sites for Methanol Synthesis from CO/CO2 on Cu/CeO2. *ACS Catalysis* **2020,** *10* (19), 11532-11544.

9. Li, Y.; Fu, Q.; Flytzani-Stephanopoulos, M., Low-temperature water-gas shift reaction over Cu- and Ni-loaded cerium oxide catalysts. *Applied Catalysis B: Environmental* **2000,** *27* (3), 179-191.

10. Gawande, M. B.; Goswami, A.; Felpin, F.-X.; Asefa, T.; Huang, X.; Silva, R.; Zou, X.; Zboril, R.; Varma, R. S., Cu and Cu-Based Nanoparticles: Synthesis and Applications in Catalysis. *Chemical Reviews* **2016,** *116* (6), 3722-3811.

11. Chen, A.; Yu, X.; Zhou, Y.; Miao, S.; Li, Y.; Kuld, S.; Sehested, J.; Liu, J.; Aoki, T.; Hong, S.; Camellone, M. F.; Fabris, S.; Ning, J.; Jin, C.; Yang, C.; Nefedov, A.; Wöll, C.; Wang, Y.; Shen, W., Structure of the catalytically active copper–ceria interfacial perimeter. *Nature Catalysis* **2019,** *2* (4), 334-341.

12. Hannagan, R. T.; Giannakakis, G.; Flytzani-Stephanopoulos, M.; Sykes, E. C. H., Single-Atom Alloy Catalysis. *Chemical Reviews* **2020,** *120* (21), 12044-12088.

13. Kyriakou, G.; Boucher, M. B.; Jewell, A. D.; Lewis, E. A.; Lawton, T. J.; Baber, A. E.; Tierney, H. L.; Flytzani-Stephanopoulos, M.; Sykes, E. C. H., Isolated Metal Atom Geometries as a Strategy for Selective Heterogeneous Hydrogenations. *Science* **2012,** *335* (6073), 1209-1212.

14. Boucher, M. B.; Zugic, B.; Cladaras, G.; Kammert, J.; Marcinkowski, M. D.; Lawton, T. J.; Sykes, E. C. H.; Flytzani-Stephanopoulos, M., Single atom alloy surface analogs in Pd0.18Cu15 nanoparticles for selective hydrogenation reactions. *Physical Chemistry Chemical Physics* **2013,** *15* (29), 12187-12196.

15. Lucci, F. R.; Liu, J.; Marcinkowski, M. D.; Yang, M.; Allard, L. F.; Flytzani-Stephanopoulos, M.; Sykes, E. C. H., Selective hydrogenation of 1,3-butadiene on platinum–copper alloys at the single-atom limit. *Nature Communications* **2015,** *6* (1), 8550.

16. Yang, K.; Yang, B., Identification of the Active and Selective Sites over a Single Pt Atom-Alloyed Cu Catalyst for the Hydrogenation of 1,3-Butadiene: A Combined DFT and Microkinetic Modeling Study. *The Journal of Physical Chemistry C* **2018,** *122* (20), 10883-10891.

17. Liu, D.; Chen, H. Y.; Zhang, J. Y.; Huang, J. Y.; Li, Y. M.; Peng, Q. M., Theoretical investigation of selective hydrogenation of 1,3-butadiene on Pt doping Cu nanoparticles. *Applied Surface Science* **2018,** *456*, 59-68.

18. Lv, C.-Q.; Liu, J.-H.; Guo, Y.; Wang, G.-C., Selective hydrogenation of 1,3-butadiene over single Pt1/Cu(1 1 1) model catalysts: A DFT study. *Applied Surface Science* **2019,** *466*, 946-955.

19. Cao, Y.; Chen, B.; Guerrero-Sánchez, J.; Lee, I.; Zhou, X.; Takeuchi, N.; Zaera, F., Controlling Selectivity in Unsaturated Aldehyde Hydrogenation Using Single-Site Alloy Catalysts. *ACS Catalysis* **2019,** *9* (10), 9150-9157.

20. Cao, Y.; Guerrero-Sańchez, J.; Lee, I.; Zhou, X.; Takeuchi, N.; Zaera, F., Kinetic Study of the Hydrogenation of Unsaturated Aldehydes Promoted by CuPtx/SBA-15 Single-Atom Alloy (SAA) Catalysts. *ACS Catalysis* **2020,** *10* (5), 3431-3443.

21. Albiter, M. A.; Crooks, R. M.; Zaera, F., Adsorption of Carbon Monoxide on Dendrimer-Encapsulated Platinum Nanoparticles: Liquid versus Gas Phase. *The Journal of Physical Chemistry Letters* **2010,** *1* (1), 38-40.

22. Zhu, Y.; Zaera, F., Selectivity in the catalytic hydrogenation of cinnamaldehyde promoted by Pt/SiO2 as a function of metal nanoparticle size. *Catalysis Science & Technology* **2014,** *4* (4), 955-962.

23. Zaera, F., New advances in the use of infrared absorption spectroscopy for the characterization of heterogeneous catalytic reactions. *Chemical Society Reviews* **2014,** *43* (22), 7624-7663.

24. Bouman, M.; Zaera, F., Kinetics of Adsorption of Methylcyclopentadienyl Manganese Tricarbonyl on Copper Surfaces and Implications for the Atomic Layer Deposition of Thin Solid Films. *The Journal of Physical Chemistry C* **2016,** *120* (15), 8232-8239.

25. Hicks, R. F.; Kellner, C. S.; Savatsky, B. J.; Hecker, W. C.; Bell, A. T., Design and construction of a reactor for in situ infrared studies of catalytic reactions. *Journal of Catalysis* **1981,** *71* (1), 216-218.

26. Grunwaldt, J.-D.; Baiker, A., In situ spectroscopic investigation of heterogeneous catalysts and reaction media at high pressure. *Physical Chemistry Chemical Physics* **2005,** *7* (20), 3526-3539.

27. Yang, Y.; Disselkamp, R. S.; Szanyi, J.; Peden, C. H. F.; Campbell, C. T.; Jr., J. G. G., Design and operating characteristics of a transient kinetic analysis catalysis reactor system employing in situ transmission Fourier transform infrared. *Review of Scientific Instruments* **2006,** *77* (9), 094104.

28. Rasmussen, S. B.; Bañares, M. A.; Bazin, P.; Due-Hansen, J.; Ávila, P.; Daturi, M., Monitoring catalysts at work in their final form: spectroscopic investigations on a monolithic catalyst. *Physical Chemistry Chemical Physics* **2012,** *14* (7), 2171-2177.

29. Wang, J.; Kispersky, V. F.; Nicholas Delgass, W.; Ribeiro, F. H., Determination of the Au active site and surface active species via operando transmission FTIR and isotopic transient experiments on 2.3wt.% Au/TiO2 for the WGS reaction. *Journal of Catalysis* **2012,** *289*, 171-178.

30. Carías-Henriquez, A.; Pietrzyk, S.; Dujardin, C., Modelling and optimization of IR cell devoted to in situ and operando characterization of catalysts. *Catalysis Today* **2013,** *205*, 134-140.

31. Pritchard, J.; Catterick, T.; Gupta, R. K., Infrared spectroscopy of chemisorbed carbon monoxide on copper. *Surface Science* **1975,** *53* (1), 1-20.

32. Kohler, M. A.; Cant, N. W.; Wainwright, M. S.; Trimm, D. L., Infrared spectroscopic studies of carbon monoxide adsorbed on a series of silica-supported copper catalysts in different oxidation states. *Journal of Catalysis* **1989,** *117* (1), 188-201.

33. Dandekar, A.; Vannice, M. A., Determination of the Dispersion and Surface Oxidation States of Supported Cu Catalysts. *Journal of Catalysis* **1998,** *178* (2), 621-639.

34. Hadjiivanov, K.; Knözinger, H., FTIR study of CO and NO adsorption and coadsorption on a Cu/SiO2 catalyst: Probing the oxidation state of copper. *Physical Chemistry Chemical Physics* **2001,** *3* (6), 1132-1137.

35. Nielsen, N. D.; Smitshuysen, T. E. L.; Damsgaard, C. D.; Jensen, A. D.; Christensen, J. M., Characterization of oxide-supported Cu by infrared measurements on adsorbed CO. *Surface Science* **2021,** *703*, 121725.

36. Redhead, P. A., Thermal desorption of gases. *Vacuum* **1962,** *12* (4), 203-211.

37. Kokalj, A.; Makino, T.; Okada, M., DFT and TPD study of the role of steps in the adsorption of CO on copper: Cu(4 1 0) versus Cu(1 0 0). *Journal of Physics: Condensed Matter* **2017,** *29* (19), 194001.

38. Anderson, R. B., *Experimental Methods in Catalytic Research, Vol. 1*. Academic Press: 1968.

39. Sheppard, N., THE VIBRATIONAL SPECTRA OF CARBON MONOXIDE CHEMISORBED ON THE SURFACES OF METAL CATALYSTS: A SUGGESTED SCHEME OF INTERPRETATION. **1978**.

40. Hoffmann, F. M., Infrared reflection-absorption spectroscopy of adsorbed molecules. *Surface Science Reports* **1983,** *3* (2-3), 107-192.

41. Stacchiola, D. J., Tuning the properties of copper-based catalysts based on molecular in situ studies of model systems. *Accounts of Chemical Research* **2015,** *48* (7), 2151-2158.

42. Raval, R.; Parker, S.; Pemble, M.; Hollins, P.; Pritchard, J.; Chesters, M., FT-rairs, eels and leed studies of the adsorption of carbon monoxide on Cu (111). *Surface Science* **1988,** *203* (3), 353-377.

43. Wadayama, T.; Kubo, K.; Yamashita, T.; Tanabe, T.; Hatta, A., Infrared reflection absorption study of carbon monoxide adsorbed on submonolayer Fe-covered

Cu (100),(110), and (111) bimetallic surfaces. *The Journal of Physical Chemistry B* **2003,** *107* (16), 3768-3773.

44. Mudiyanselage, K.; An, W.; Yang, F.; Liu, P.; Stacchiola, D. J., Selective molecular adsorption in sub-nanometer cages of a Cu 2 O surface oxide. *Physical Chemistry Chemical Physics* **2013,** *15* (26), 10726-10731.

45. Kruppe, C. M.; Krooswyk, J. D.; Trenary, M., Polarization-dependent infrared spectroscopy of adsorbed carbon monoxide to probe the surface of a Pd/Cu (111) single-atom alloy. *The Journal of Physical Chemistry C* **2017,** *121* (17), 9361-9369.

46. Hollins, P.; Pritchard, J., Interactions of CO molecules adsorbed on oxidised Cu (111) and Cu (110). *Surface science* **1983,** *134* (1), 91-108.

47. Borguet, E.; Dai, H. L., Site‐specific properties and dynamical dipole coupling of CO molecules adsorbed on a vicinal Cu (100) surface. *The Journal of chemical physics* **1994,** *101* (10), 9080-9095.

48. Kavtaradze, N.; Sokolova, N., A study of the infrared spectra of carbon monoxide adsorbed on metals of the copper subgroup and on cobalt, ruthenium, rhodium, and palladium. *Journal of Applied Spectroscopy* **1966,** *4* (5), 325-330.

49. Padley, M. B.; Rochester, C. H.; Hutchings, G. J.; King, F., FTIR spectroscopic study of thiophene, SO2, and CO adsorption on Cu/Al2O3 catalysts. *Journal of Catalysis* **1994,** *148* (2), 438-452.

50. Hollins, P.; Pritchard, J., Interactions of CO molecules adsorbed on Cu (111). *Surface Science* **1979,** *89* (1-3), 486-495.

51. Harendt, C.; Goschnick, J.; Hirschwald, W., The interaction of CO with copper (110) studied by TDS and LEED. *Surface Science* **1985,** *152,* 453-462.

52. Simonovis, J. P.; Hunt, A.; Palomino, R. M.; Senanayake, S. D.; Waluyo, I., Enhanced stability of Pt-Cu single-atom alloy catalysts: in situ characterization of the Pt/Cu (111) surface in an ambient pressure of CO. *The Journal of Physical Chemistry C* **2018,** *122* (8), 4488-4495.

53. Clayton, J.; Giauque, W., The heat capacity and entropy of carbon monoxide. Heat of vaporization. Vapor pressures of solid and liquid. Free energy to 5000 K. From spectroscopic data. *Journal of the American Chemical Society* **1932,** *54* (7), 2610-2626.

54. Yates Jr, J. T.; Goodman, D. W., Carbon monoxide chemisorption on Ni (100)—direct detection of adsorbate–adsorbate interactions by desorption kinetic measurements. *The Journal of Chemical Physics* **1980,** *73* (10), 5371-5375.

55. Gland, J. L.; Fischer, D. A.; Shen, S.; Zaera, F., Displacement of carbon monoxide chemisorbed on metals by hydrogen. *Journal of the American Chemical Society* **1990,** *112* (15), 5695-5697.

56. Kash, P.; Yang, M.; Teplyakov, A.; Flynn, G.; Bent, B., Chemical displacement of molecules adsorbed on copper surfaces: Low-temperature studies with applications to surface reactions. *The Journal of Physical Chemistry B* **1997,** *101* (40), 7908-7918.

57. Bowker, M.; King, D. A., Anomalous adsorption kinetics. γ-Nitrogen on the {110} plane of tungsten. *Journal of the Chemical Society, Faraday Transactions 1: Physical Chemistry in Condensed Phases* **1979,** *75*, 2100-2115.

58. Arumainayagam, C. R.; McMaster, M. C.; Madix, R. J., Coverage dependence of molecular adsorption dynamics: ethane on platinum (111). *The Journal of Physical Chemistry* **1991,** *95* (6), 2461-2465.

59. Molinari, E.; Tomellini, M., Role of Vibrational Excitation of the Adlayer in'Precursor-Mediated'Sticking Probabilities of CO on Metal Surfaces: A Kinetic Model. *Zeitschrift für Physikalische Chemie* **2012,** *226* (4), 253-274.

60. Karakalos, S.; Lawton, T. J.; Lucci, F. R.; Sykes, E. C. H.; Zaera, F., Enantiospecific Kinetics in Surface Adsorption: Propylene Oxide on Pt (111) Surfaces. *The Journal of Physical Chemistry C* **2013,** *117* (36), 18588-18594.

Chapter 7 Core-shell Pt@Cu catalysts

In the previous chapter, the oxidation state and position of Cu and Pt atoms within Cu-Pt nanoparticles were analyzed. To further investigate the promotion of hydrogenation chemistry of Pt-Cu catalysts following our surface-science approach, we needed to prepare Pt-Cu in a unique nanostructure such as a core-shell. This will enable a direct comparison regarding catalytic performance to be made between fully mixed and segregated bimetallic samples. Above all, the best core-shell Pt@$Cu_{5.25}$/SBA-15 obtained will be shown here in this chapter including how it was synthesized and how our preparation method was developed.

7.1 Experimental Details

Different from the incipient wetness impregnation method mentioned in our previous work[1-2], sequential deposition was used in the synthesis of Pt@Cu catalysts via the reduction of proper precursors. All catalysts were prepared of commercial SBA-15 (ACS Material) using Copper(II) nitrate hemi(pentahydrate) ($Cu(NO_3)_2 \cdot 2.5H_2O$, Sigma-Aldrich, 98% purity) and Chloroplatinic acid hexahydrate ($H_2PtCl_6 \cdot 6H_2O$, Sigma-Aldrich, ≥37.50% Pt basis).

Synthesis of Pt/SBA-15. First prepare 20 mg/ml $H_2PtCl_6 \cdot 6H_2O$ solution in deionized water. Then Mix 45 ml Ethylene glycol (EG), 0.060 g Polyvinylpyrrolidone (PVP, Mw=

10,000), 0.31 g SBA-15, and 0.4 ml of H_2PtCl_6 aqueous solution in a 100 ml flask. Sonicate for 30 minutes, followed by stirring the mixture with a magnetic stir bar for one hour. Then reflux the mixture for three hours. After cooling the mixture to room temperature, wash the sample with 350 ml EtOH and water mixture (1:1) overnight. Then filter and dry in an oven overnight.

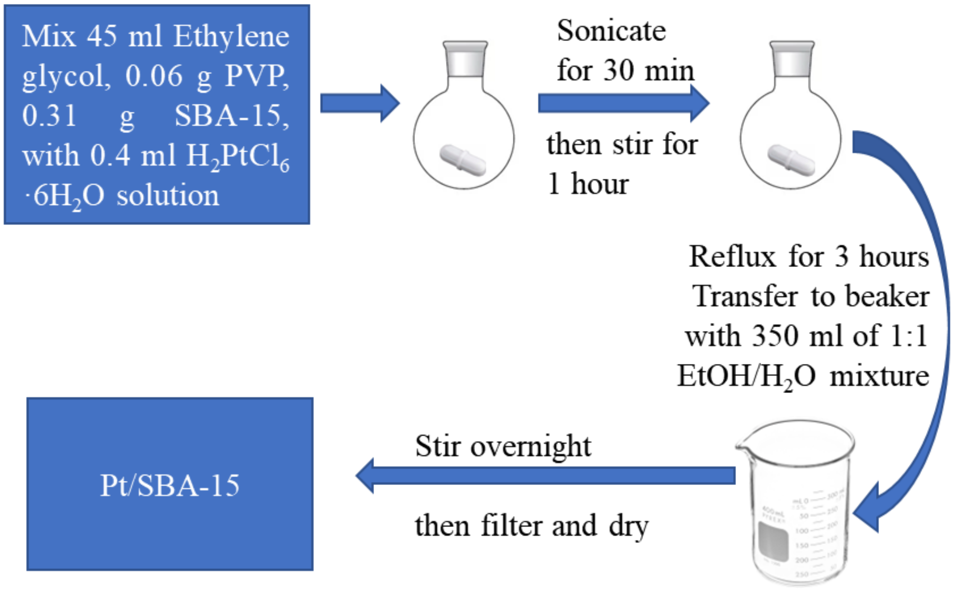

Figure 7-1. Process of synthesize Pt/SBA-15

Treat Pt/SBA-15 with Tert-Butylamine (TBA, Sigma-Aldrich). 300 mg Pt/SBA-15 is put in a 100 ml flask and filled with 100 ml of tert-Butylamine. Proceed to agitate the mixture with vigor for a period of 72 hours. Following agitation, cleanse the product thrice using ethanol, and allow it to desiccate overnight.

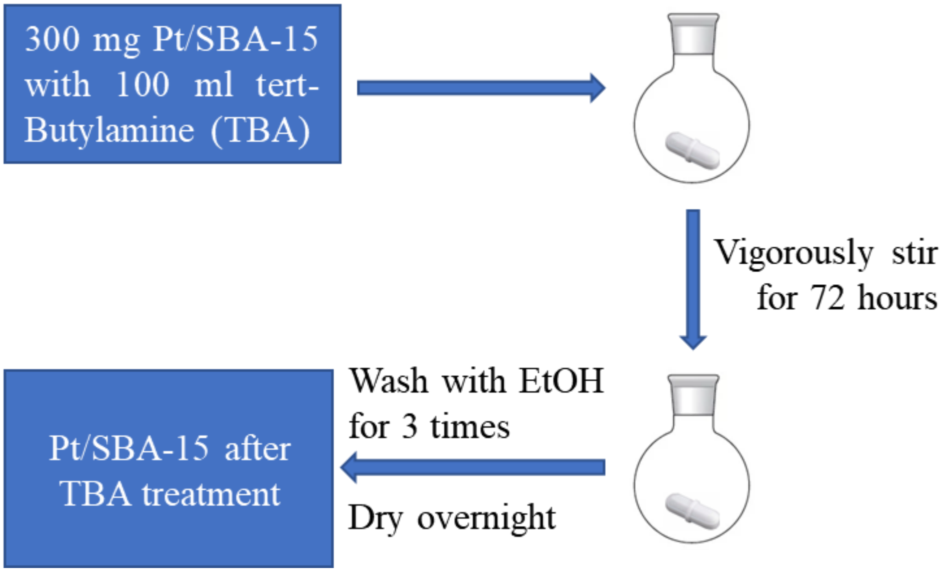

Figure 7-2. Process of pretreatment of Pt/SBA-15 with TBA to remove surfactant.

Synthesis of Pt@$Cu_{5.25}$/SBA-15. Prepare 20 mg/ml $H_2PtCl_6 \cdot 6H_2O$ solution and 20 mg/ml $Cu(NO_3)_2 \cdot 2.5H_2O$ with deionized water, respectively. Prepare L-ascorbic acid (AA) solution (mix 12.5 ml H_2O with 1 gram of L-ascorbic acid). Mix 0.1 g Pt/SBA-15 (washed with TBA for three days) with 0.56 ml Cu precursor solution with 12.5 ml water. Heat to 80 °C then add AA solution to the mixture above dropwise and heat for 16 hours at 80 °C. Then wash the resulting catalysts with distilled water and EtOH two times, respectively. Finally, dry the catalyst overnight.

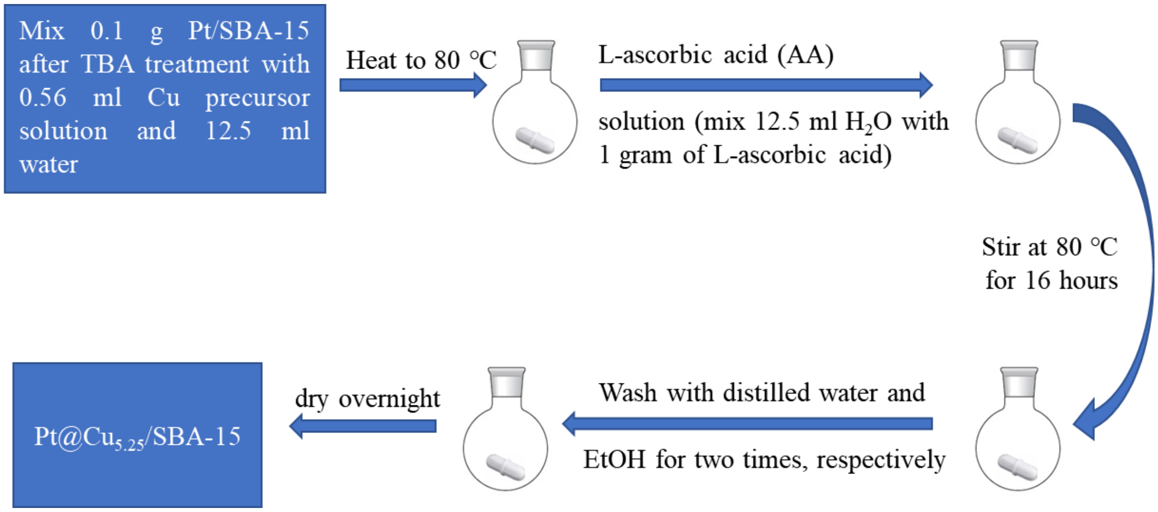

Figure 7-3. Process of synthesizing Pt@$Cu_{5.25}$/SBA-15.

The transmission Fourier transform infrared (FTIR) spectroscopy characterization experiments were performed by pressing about 15 mg of the catalyst into a self-supporting wafer and loading it inside a homemade quartz cell with NaCl windows. In this experiment, initially the transmission cell was evaluated, followed by adding 20 Torr carbon monoxide into the cell and then taking the data while heating the temperature from room temperature to 220 °C, then data was taken while cooling down the cell to RT. The heating-cooling cycle was repeated twice.

7.2 Results and Discussion

7.2.1 Characterization of Pt/SBA-15 and Core-shell Pt@$Cu_{5.25}$/SBA-15 Catalysts

This study was initiated by producing a well-defined Pt catalyst before synthesizing core-shell catalysts. Figure 7-4 provides TEM results for Pt/SBA-15. It should be noted that nanoparticles of Pt are well-dispersed on SBA-15 with an average size of 3.59 ± 0.54 nm. Afterward, the surfactant was removed by treating Pt/SBA-15 with TBA before depositing Cu atoms onto Pt atoms. From Figure 7-5, it can be seen that after the loading of Cu atoms, nanoparticles maintain well-dispersed all over the supporting material. Furthermore, the top panel of Figure 7-6 presents a clear indication of Pt@$Cu_{5.25}$ core-shell structure, as demonstrated by the existence of Cu signals on both sides of Pt signals and Cu seems to always extend beyond Pt. In other words, Pt nanoparticles are fully covered by a Cu shell. This is also consistent with IR data from Figure 7-7. However, it should be noted that for our optimized core-shell sample Pt@$Cu_{5.25}$/SBA-15, one potential pitfall still exists, which is the excessive Cu deposition on SBA-15 directly. This might arise from the forming Cu seeds on the surface of SBA-15 during the deposition process onto Pt NPs. Such a limitation could result in the occurrence of hydrogenation reactions not only on the core-shell Pt@Cu NPs but also on Cu-only NPs. We are still in the process of eliminating Cu-only NPs.

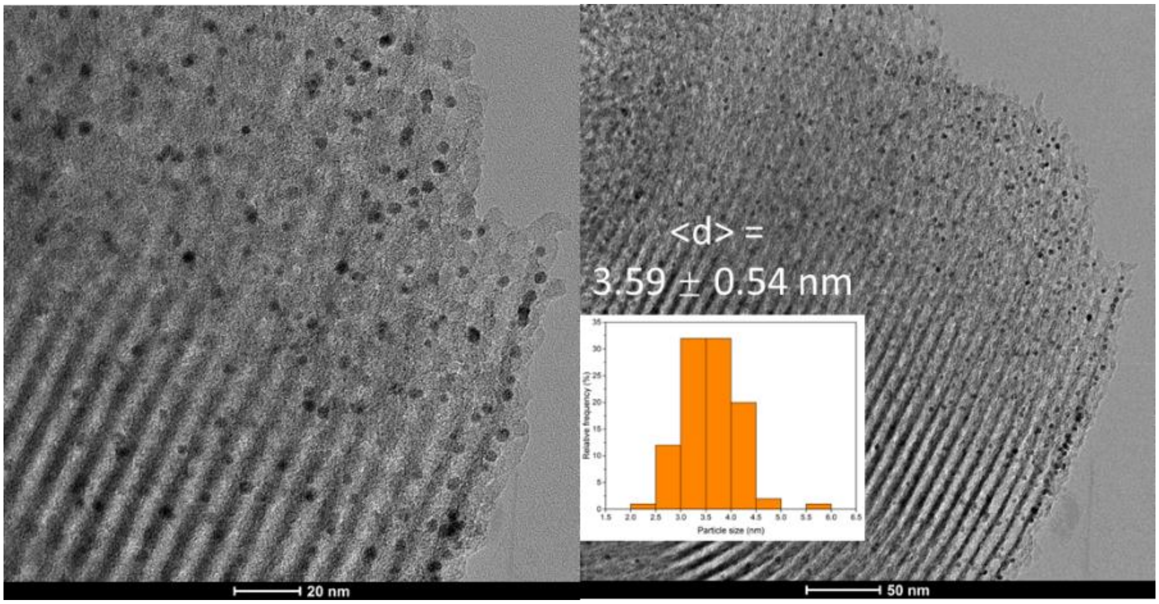

Figure 7-4. Pt/SBA-15 TEM & Particle size distributions. Scale bars (from left to right): 20 and 50 nm.

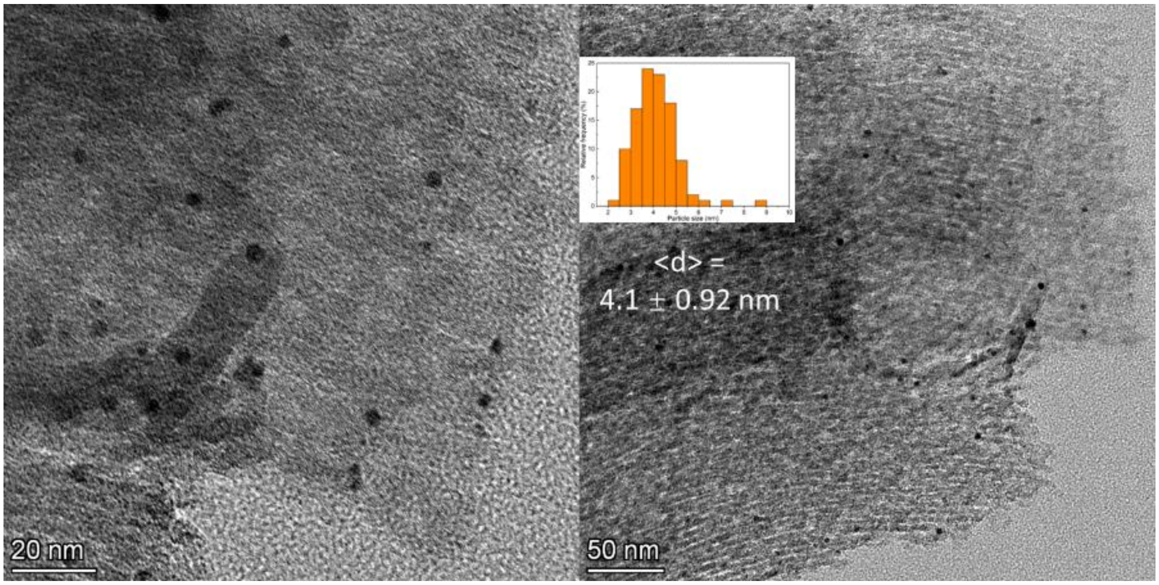

Figure 7-5. Pt@$Cu_{5.25}$/SBA-15 TEM & Particle size distributions. Scale bars (from left to right): 20 and 50 nm.

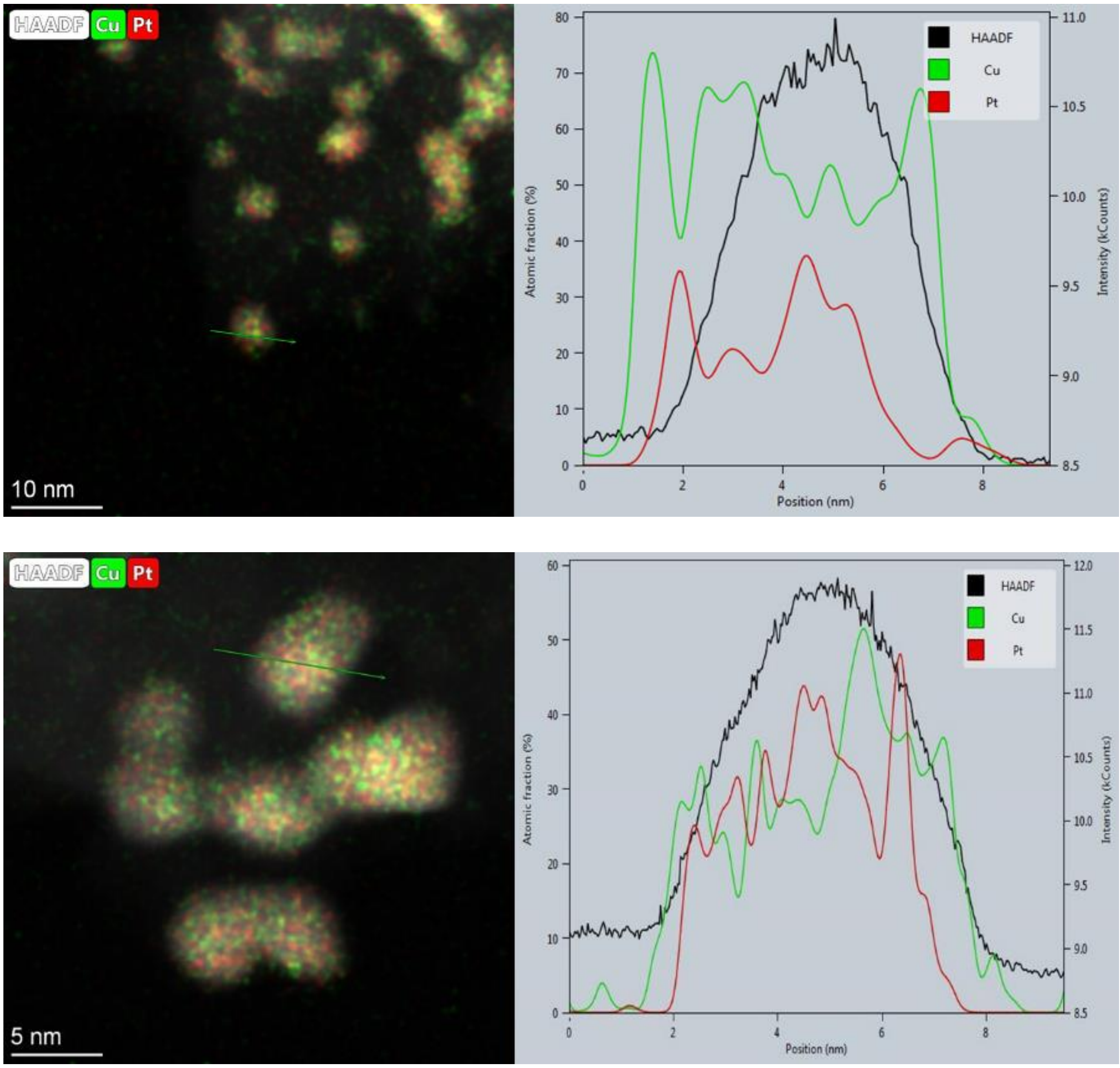

Figure 7-6. Pt@$Cu_{5.25}$/SBA-15 EDS images and line scan results, with the Pt and Cu atoms colored in red and green, respectively. Top row, 1st batch of Pt@$Cu_{5.25}$/SBA-15, bottom row, 2nd batch of Pt@$Cu_{5.25}$/SBA-15. Scale bars (from top to bottom): 10 and 5 nm.

In addition, the core-shell catalyst has been produced several times and nanoparticles are always approximately the same size as shown in Table 7-1 obtained from Figure 7-6.

Energy dispersive spectrometry (EDS) images of core-shell structure being found in those batches prove the reproducibility of our methods.

Table 7-1. Properties of Pt/SBA-15 and two batches of Pt@$Cu_{5.25}$/SBA-15.

Name	Batch	Weight percent from ICP		Particle size (nm)
		Pt	Cu	
Pt/SBA-15	\	0.826	\	3.59 ± 0.54
Pt@$Cu_{5.25}$/SBA-15	1st batch	0.966	1.959	4.10 ± 0.92
Pt@$Cu_{5.25}$/SBA-15	2nd batch	\	\	4.28 ± 0.84

7.2.2 FTIR Results

The preparation of core-shell Pt@Cu catalysts requires verification of the absence of Pt atoms on the surface. Carbon monoxide adsorption can therefore be used here to assess the metal nanoparticles on the surface in the presence of CO atmosphere. Three consecutive heating and cooling cycles experiments are presented in Figure 7-7. It should be noted that there is one peak located at approximately 2118 cm^{-1} but no peak located at around 2029 cm^{-1}, which can be assigned to CO adsorbed on Cu and Pt, respectively (bottom trace in the left panel of Figure 7-7). This indicates that initially on the surface of this catalyst, Pt cannot be observed. In other words, Pt is fully covered by Cu, which is consistent with our EDS data from Figure 7-6. After one cycle of heating-cooling, CO/Pt signal can be seen at around 2029 cm^{-1} under room temperature (bottom trace in second to left panel of Figure 7-7), suggesting Pt atoms are segregating to the surface. After that sequence of cycles, Pt can be continuously detected on the surface at RT, indicating the segregation of Pt atoms is not reversible.

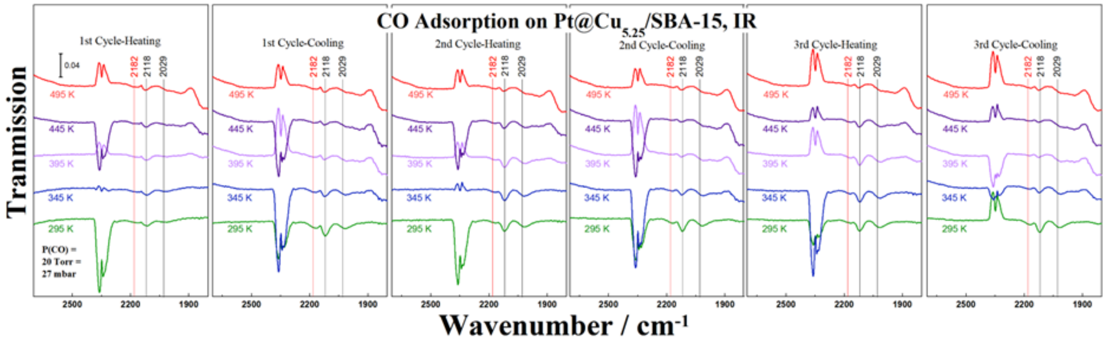

Figure 7-7. In-situ IR spectra in the C-O stretching region for Pt@Cu$_{5.25}$/SBA-15 catalyst exposed to 20 Torr (27 mbar) of carbon monoxide as a function of catalyst temperature, obtained via subtraction of the corresponding traces (recorded in the absence of the catalyst, for the gas alone). Shown are the data for three consecutive heating and cooling cycles.

7.3 Exposing Core-Shell Catalysts to CO Under Different Temperature

In this section, the same batch of core-shell Pt@Cu$_{5.25}$/SBA-15 were exposed to CO under different temperatures. In detail, about 10 mg of catalyst was exposed to 100 Torr (133 mbar) CO in our infrared transmission cell at temperature X (X = 300, 493 K) for 1 hour for 3 times in total. To be noted, at the end of the CO exposure experiment, CO was evacuated from the cell before the temperature was lowered to RT.

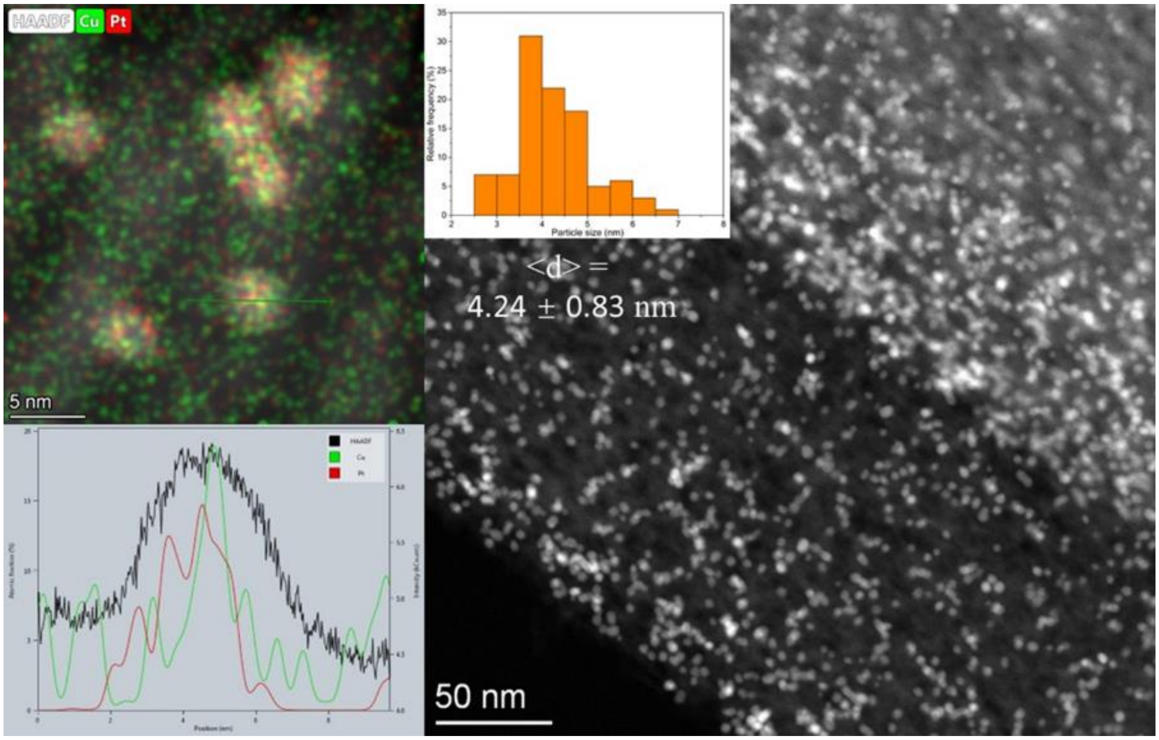

Figure 7-8. Pt@Cu$_{5.25}$/SBA-15 TEM results after exposing to 100 Torr CO under RT. The top left figure corresponds to the EDS mapping result and the bottom right figure corresponds to the EDS line scan results. The right figure corresponds to the HAADF image and nanoparticle size distribution for this sample.

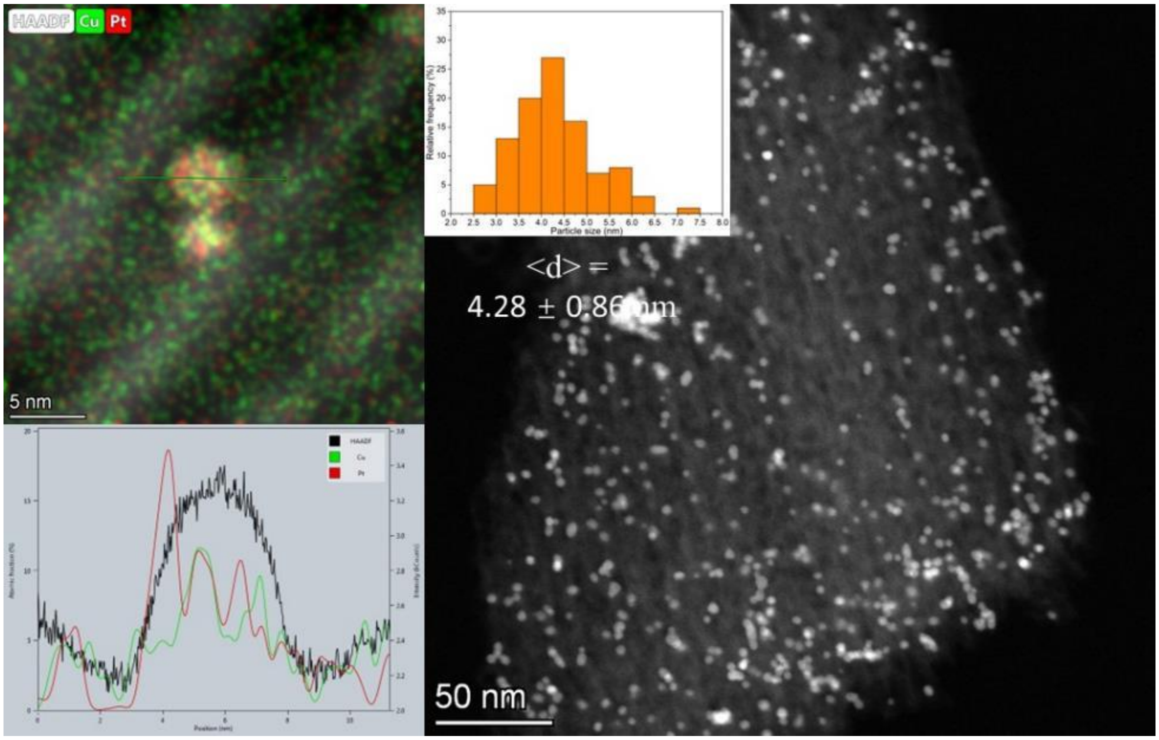

Figure 7-9. Pt@$Cu_{5.25}$/SBA-15 TEM results after exposing to 100 Torr CO under 493K. The top left figure corresponds to EDS mapping results and the bottom right figure corresponds to EDS line scan results. The right figure corresponds to the HAADF image and nanoparticle size distribution for this sample.

Our results suggest that the structure of our core-shell catalysts was maintained after being exposed to CO at room temperature (RT) and 493 K. This suggests the presence of a relatively thick Cu shell that effectively prevented CO-induced migration of Pt atoms to the surface.

7.4 Development of Preparation Method

7.4.1 Overview of the Development Route

Following the successful synthesis of well-defined Pt/SBA-15 catalyst, we deposited Cu onto Pt. The evolution of our synthesis method is depicted in Figure 7-10. Our first approach involved a sequential deposition method of preparing Pt@Cu core-shell catalyst, as shown in step 1 of Figure 7-10. Namely, after the deposition of Pt atoms onto SBA-15 in EG, the previously prepared Cu precursor solution was added directly to the mixture of Pt/SBA-15 and EG. However, such a reduction in EG led to the formation of large NPs. Moreover, our in situ IR results reveal the presence of Pt on the surface, indicating that the Cu shell did not fully encapsulate Pt NPs. This could be attributed to the high temperature used during the reduction of Cu under the reflux of EG (198 °C/ 471 K). After that, we found that L-ascorbic acid (AA) can be also applied here to reduce Cu^{2+} to Cu. In step 2, we added the prepared Cu precursor solution directly into AA solution mixed with Pt/SBA-15, but it would seem that adding Cu precursor solution (20 mg/ml) would introduce a very high concentration at the beginning of this reaction and therefore they could cause a high nucleation rate. Then in step 3, a syringe-pump was applied to add a diluted Cu precursor solution, and varied pumping rates were used for the same diluted Cu precursor solution. A reduction in pumping rate results in a diminished addition of copper precursor solution per unit of time, leading to a lower concentration. However, this did not lead to a core-shell catalyst with no Pt atoms on the surface. Therefore, we attempted to increase the ratio of Cu:Pt to as high as 12:1 in step

4, but this approach was also unsuccessful. Additionally, in step 4 we also considered the possibility that residual surface surfactant (PVP) could impede the deposition of Cu onto Pt NPs. Rather than calcinating the Pt/SBA-15 at high temperature, we used TBA to remove PVP. However, Pt can still be seen on the surface as well. At this point, we realized Cu^{2+} might not have been fully reduced by AA. Therefore, in step 5, an excessive amount of L-ascorbic acid was employed. Subsequently, it was observed that the color of the solution changed from dark red (0.12 g of L-ascorbic acid) to purple (1 g of L-ascorbic acid). This further supported our hypothesis, indicating that the reducing reaction was still ongoing with the aid of an additional 0.88 g of L-ascorbic acid. However, despite these observations, the presence of Pt signals remained. Up until step 5, we had been altering the quantity of Cu, adding an excessive amount of reducing agent, removing surfactant on Pt/SBA-15, and reducing Cu^{2+} under relatively low temperatures. We started to look at the initial reduction of Cu when we added Cu into the reducing environment to prompt an immediate reduction of Cu^{2+}, which resulted in an overly rapid reaction for the Cu precursor solution, preventing even dispersal throughout the mixture. Therefore, in step 6, we tried the opposite way by mixing Cu precursor solution with Pt/SBA-15 and H_2O first, then gradually adding the AA solution into the mixture. This method ultimately proved successful, as indicated by the absence of Pt signals in the in situ IR results. However, the ratio of Cu:Pt in step 6 was relatively high at 6:1. While we were trying to figure out why such a high ratio was required, multiple ways were deployed to decrease the high ratio of Cu:Pt, to eliminate the possibility of unfavored Cu-only NPs on the surface. Most of them failed. Also, during the synthesis process, the presence of floating black particles in the supernatant was observed. One reason for demanding such a high ratio could be: after filtration of the mixture of Pt/SBA-15 in EG, these particles were found to have adhered to the Pt/SBA-15 catalysts, thereby requiring an additional amount of Cu to cover all the Pt surface sites. In step 7, we modified our method of collecting Pt/SBA-15 to remove the floating particles first, then get the precipitation via filtration. With the aforementioned modification, in step 8, we obtained our optimized core-shell catalyst, Pt@$Cu_{5.25}$/SBA-15.

1. Cu reduction in EG. Large NPs. Pt signal appears in CO IR experiment.

2. Cu reduction via L-ascorbic acid under low temperature (80 °C). Pt signal still exist in CO IR experiment.

3. Syringe-pump was used for adding a variety of concentration of Cu solution to obtain lower initial concentration of Cu^{2+} during reduction process. Pt signal still exist in CO IR experiment

4. Increasing the ratio of Cu:Pt and removing surfactant with TBA was tried. Pt signal still exist in CO IR experiment

5. The amount of reducing agent L-ascorbic was increased from 0.12 g to 1 g. Pt signal still exist in CO IR experiment

6. Instead of adding Cu precursor solution into AA acid solution, we tried the reversed way by adding reducing agent to the well mixture Cu precursor solution with Pt/SBA-15. Core-shell Pt@Cu_6/SBA-15 was obtained. **Only Cu can be observed on the surface.**

7. Getting rid of the supernatant after mixing Pt/SBA-15 with EtOH/H_2O then get the precipitation catalyst via filtration. This method helped removing some black color floating stuff (which seems to be large aggregated Pt NPs).

8. The lowest ratio of Cu:Pt is found to be 5.25:1 so far.

Figure 7-10. Development of synthesis method of Pt@$Cu_{5.25}$/SBA-15

7.4.2 Results and Discussion of Unsuccessful Catalysts

With the development of the synthesis method discussed in the previous section, some results of unsuccessful catalysts are shown here.

a) Example of unsuccessful Pt/SBA-15

As already mentioned in step 7 in Figure 7-10, Pt/SBA-15 catalyst was obtained by getting rid of the supernatant after mixing Pt/SBA-15 with EtOH/H_2O then getting the precipitation catalyst via filtration. However, as shown below, our initial synthesis method encountered issues with aggregated NPs. In Figure 7-11, aggregated NPs can be seen for Pt/SBA-15. The aggregation was caused by the method used to obtain the precipitation within the solution. For this catalyst, after three hours of reflux in EG, it was washed and centrifuged with D.I. water and ethanol twice, respectively. This washing step may have led to the formation of aggregated nanoparticles. Therefore, washing was replaced with mixing the catalyst with EtOH/H_2O.

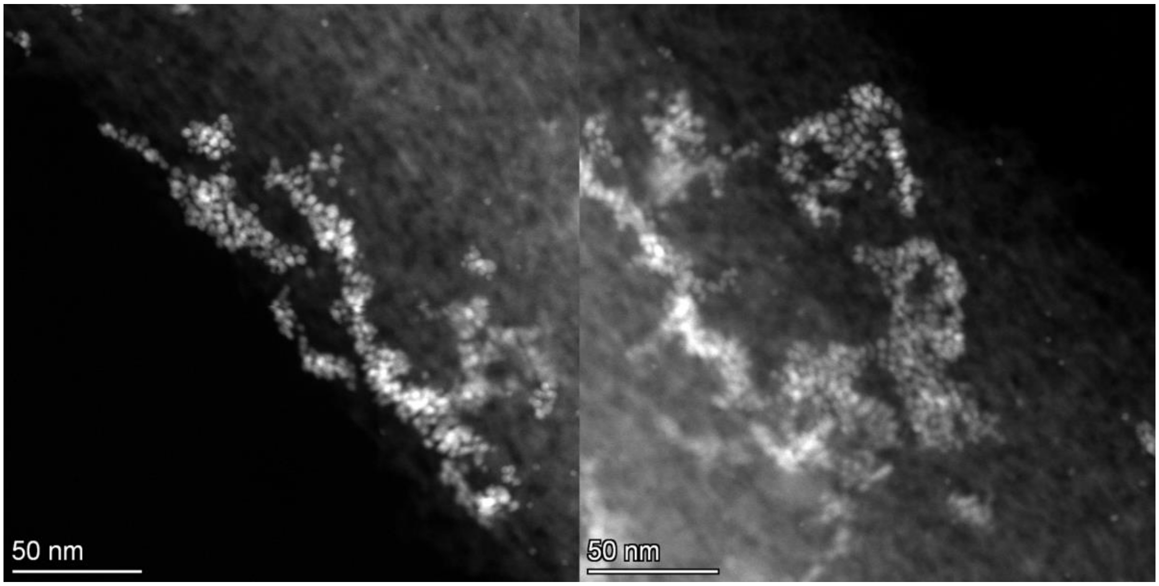

Figure 7-11. Pt/SBA-15 (#60-1) TEM results with scale bar as 50 nm. After three hours of reflux in EG, sample #60-1 was washed and centrifuged twice with D.I. water and ethanol twice, respectively.

Furthermore, various techniques were employed to eliminate PVP from the surface of our catalysts. One way is by annealing the catalyst under O_2 at high temperatures (773K), which has been demonstrated to be effective in previous studies conducted by our group. However, the issue for aggregated Pt NPs became even more severe when annealing was carried out under such conditions, compared to TEM results from Figure 7-11. This suggested that the most optimal way to remove PVP may not be through annealing at high temperatures under O_2, but rather through washing with TBA.

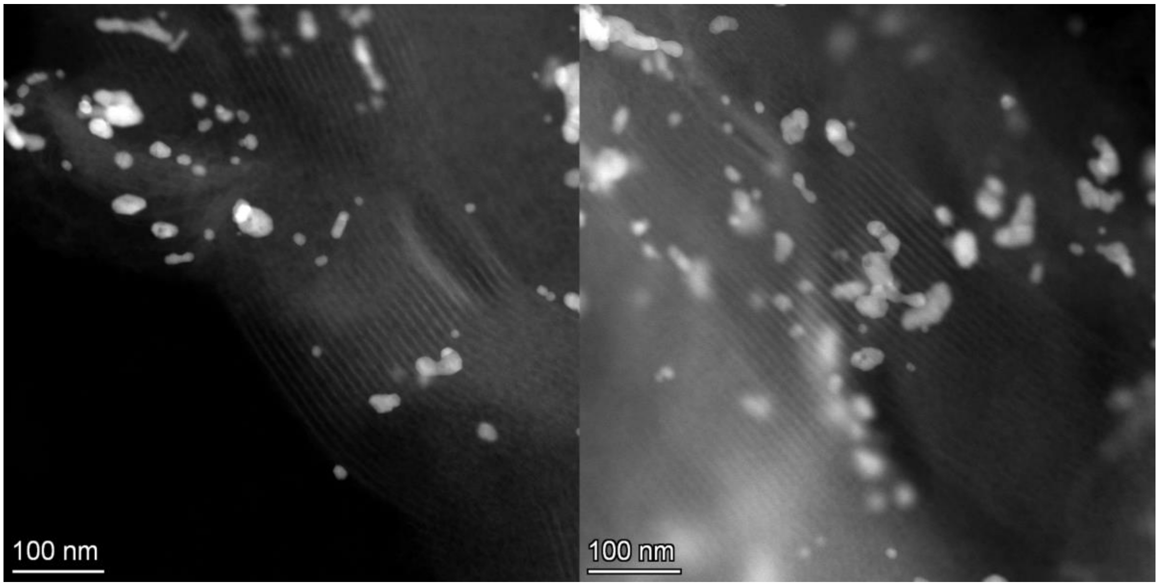

Figure 7-12. Pt/SBA-15 (#60-1-1) TEM results with scale bar as 100 nm. Sample #60-1-1 was obtained by annealing sample #60-1 in O_2 (773 K) for 24 hours.

b) Some examples of unsuccessful Pt@Cu/SBA-15 without core-shell structure

i. Deposit Cu atoms via the reduction in Ethylene Glycol

TEM, EDS linescan, and in-situ IR spectroscopy results are shown for $Pt@Cu_{5.8}/SBA-15$ in Figure 7-13, Figure 7-14, Figure 7-15, respectively. This catalyst was discussed in step 1 in Figure 7-10, which represents the failure of obtaining well-dispersed NPs with Ethylene Glycol as the reducing agent for Cu. As shown in Figure 7-15, it should be also noted that in situ IR results indicated Pt atoms can be observed on the surface of the catalysts, suggesting Pt NPs were not fully covered by Cu shell. It should be mentioned that linescan results in Figure 7-14 indicated excess deposition of Cu on the surface of SBA-15, while Cu are expected to only exist around Pt NPs signal.

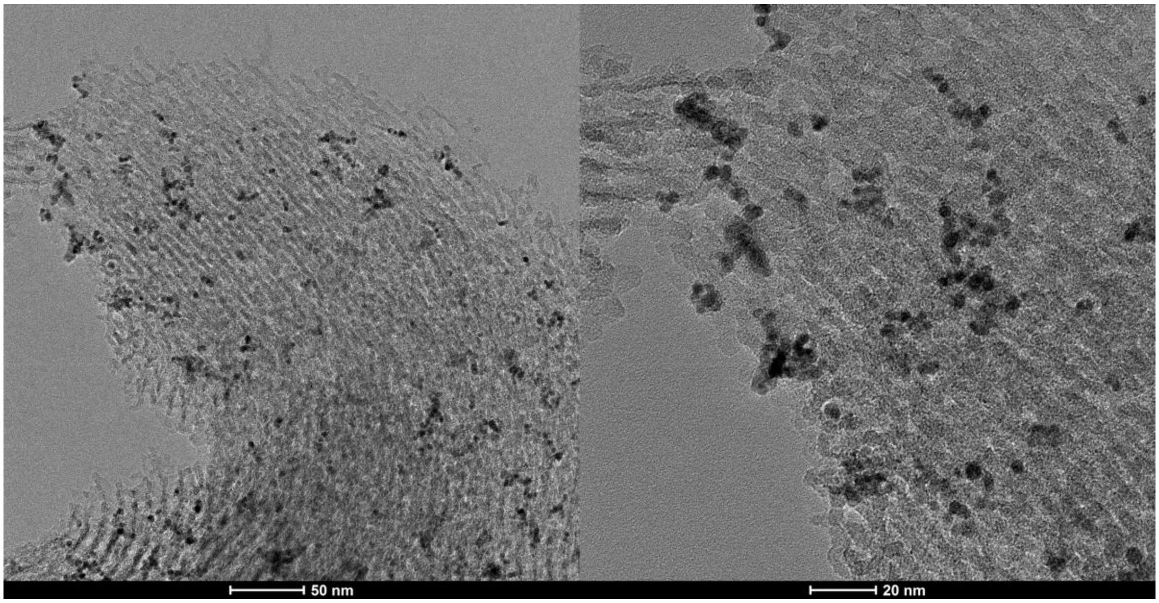

Figure 7-13. Pt@Cu$_{5.8}$/SBA-15 TEM results. Scale bars (from left to right): 50 and 20 nm.

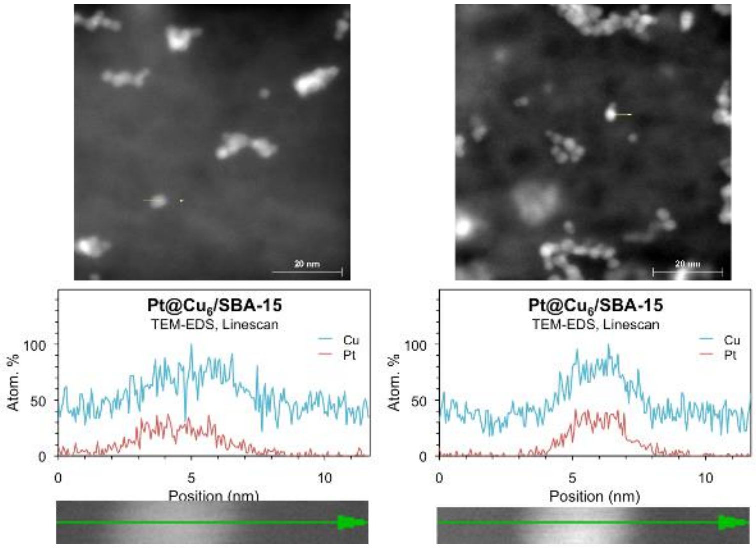

Figure 7-14. EDS linescan results of Pt@Cu$_{5.8}$/SBA-15. Pt@Cu$_6$/SBA-15 above indicated estimated ratio and Pt@Cu$_{5.8}$/SBA-15 indicated ratio obtained after ICP analysis.

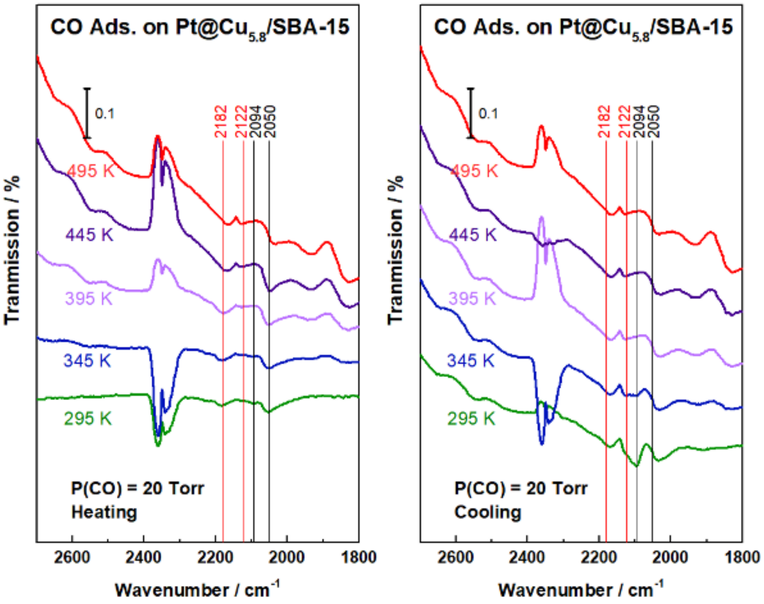

Figure 7-15. In-situ IR spectra in the C-O stretching region for Pt@Cu$_{5.8}$/SBA-15 catalyst exposed to 20 Torr (27 mbar) of carbon monoxide as a function of catalyst temperature, obtained via subtraction of the corresponding traces(recorded in the absence of the catalyst, for the gas alone).

ii. Excess amount of Cu atoms

Furthermore, we endeavored to achieve complete coverage of Pt atoms by depositing a surplus of Cu onto Pt/SBA-15, in addition to Pt@Cu5.8/SBA-15. In-situ IR results for this sample is shown in Figure 7-16. In this sample, the atomic ratio of Cu to Pt was 12:1. However, the existence of peak locates at around 2029 cm^{-1} still indicated the presence of Pt atoms on the surface. This result further confirms our conclusion that the surface of Pt/SBA-15 may be affected by surfactant and therefore hinder the deposition of Cu atoms.

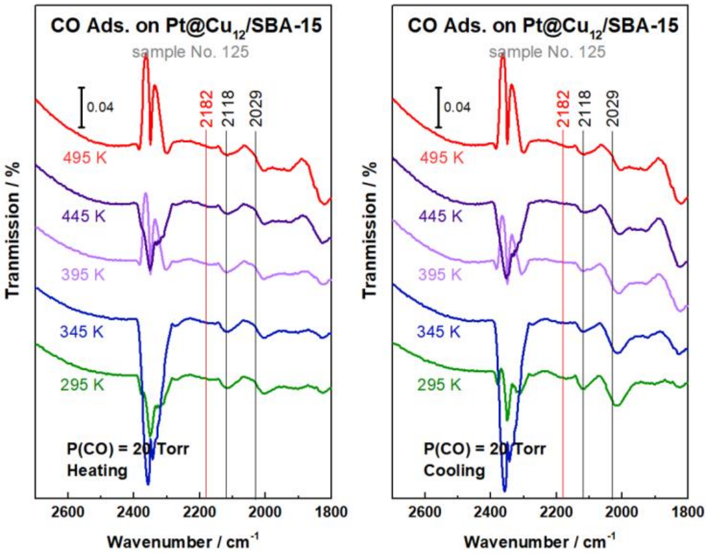

Figure 7-16. In-situ IR spectra in the C-O stretching region for Pt@Cu_{12}/SBA-15 catalyst exposed to 20 Torr (27 mbar) of carbon monoxide as a function of catalyst temperature, obtained via subtraction of the corresponding traces(recorded in the absence of the catalyst, for the gas alone).

iii. Synthesizing Pt@Cu NPs, then deposit onto SBA-15

One commonly used approach to synthesizing alloyed catalyst is to prepare alloy nanoparticles, then deposit them on the substrate. Such method was also tried here. For example, first Pt NPs are synthesized, then Cu atoms are deposited onto those Pt NPs. Until this step, it can be seen from Figure 7-17 that NPs seemed to be well-dispersed. Then the NPs were deposited onto SBA-15 and tested with in situ IR. The existence of peak locates at ~2045 cm^{-1} suggested that Pt are not fully covered by Cu as well. Although this approach appears promising, further investigation is necessary to achieve full coverage of Pt in the future.

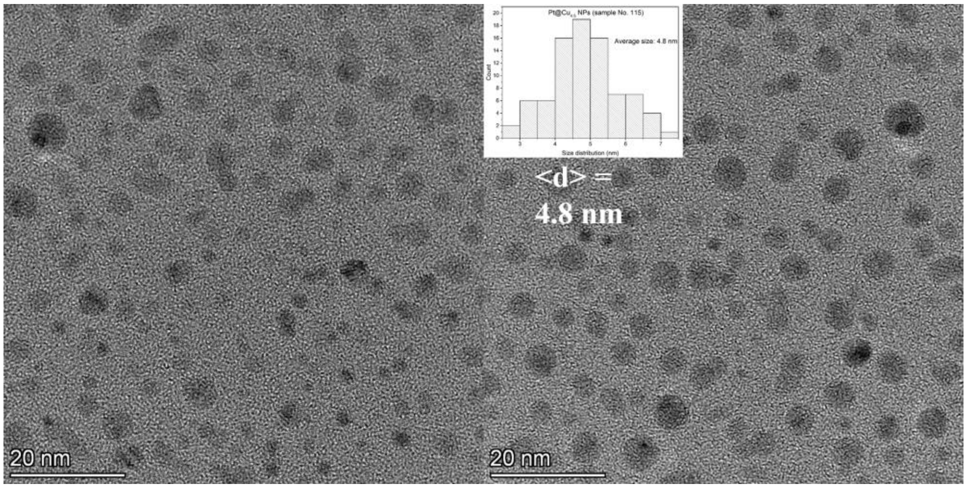

Figure 7-17. TEM images and size distribution of Pt@$Cu_{4.5}$ NPs

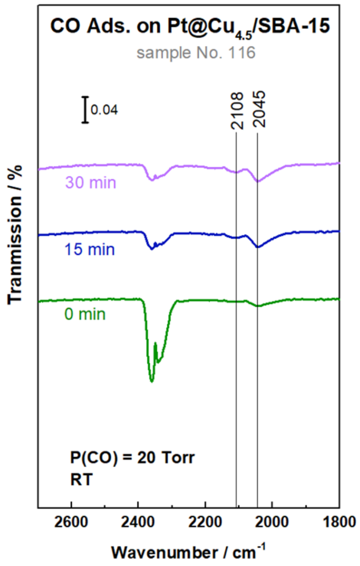

Figure 7-18. In-situ IR spectra in the C-O stretching region for Pt@$Cu_{4.5}$/SBA-15 catalyst exposed to 20 Torr (27 mbar) of carbon monoxide as a function of catalyst temperature, obtained via subtraction of the corresponding traces.

7.5 Conclusion

The ultimate goal of synthesizing core-shell catalysts is to gain a better understanding of how catalytic performance can be affected differently when comparing fully mixed and segregated bimetallic samples. In this work, Pt/SBA-15, and core-shell Pt@$Cu_{5.25}$/SBA-15 were synthesized. TEM, EDS, and CO adsorption experiments were performed to study them.

Figure 7-6 is the data taken with a copper grid and might indicate there are some Cu small-size nanoparticles dispersed alone. In the future, the synthesis method will be optimized to obtain a core-shell catalyst with only Pt@Cu nanoparticles but not Pt@Cu + Cu nanoparticles. To summarize, Pt/SBA-15 and core-shell structure were obtained with only Cu atoms on the surface.

7.6 Reference

1. Cao, Y.; Guerrero-Sańchez, J.; Lee, I.; Zhou, X.; Takeuchi, N.; Zaera, F., Kinetic Study of the Hydrogenation of Unsaturated Aldehydes Promoted by CuPtx/SBA-15 Single-Atom Alloy (SAA) Catalysts. *ACS Catalysis* **2020,** *10* (5), 3431-3443.

2. Cao, Y.; Chen, B.; Guerrero-Sánchez, J.; Lee, I.; Zhou, X.; Takeuchi, N.; Zaera, F., Controlling Selectivity in Unsaturated Aldehyde Hydrogenation Using Single-Site Alloy Catalysts. *ACS Catalysis* **2019,** *9* (10), 9150-9157.

Chapter 8 Conclusion and Thoughts on Future Work

8.1 Conclusions

Over the last decades, the hydrogenation of unsaturated aldehydes has played a crucial role in the manufacturing of many fine chemicals, such as perfumes[1] and medicine[2], via the synthesis of many valuable intermediates. Understanding the fundamental nature of Cu-Pt catalysts in hydrogenation is the goal we put forward in this Pd.D. thesis. The oxidation state of copper and the location of copper atoms, the position of platinum atoms, and the synthesis of core-shell structure Pt@Cu were explored.

It is noteworthy to highlight that our findings from the study of SAA catalysis have contravened previously established hypotheses regarding the mechanism of hydrogenation reactions facilitated by SAA catalysts. It can be seen in Figure 8-1, prior surface-science works have suggested that the H_2 molecule would be dissociated by individual Pt atoms on the surface of the catalyst. Then the resulting H atoms would spill over to the Cu surface.[3]

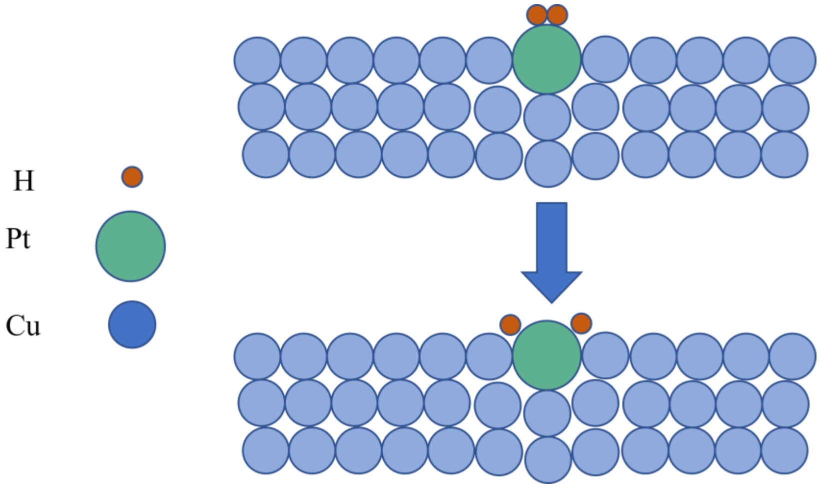

Figure 8-1. Previous proposed mechanism of H_2 dissociation on SAAs catalysts

On the other hand, our results indicated that there would be a different mechanism. First of all, as shown in Figure 8-2 - Figure 8-4, models for CuPt$_x$/SBA-15, where x = 0.2, 0.05, and 0.005, were analyzed with the help of Dr. Yuanyuan Li. These models are analyzed based on IR spectroscopies and XAS results. IR assisted to determine the metal composition and oxidation state on the surface of the substrate. XANES helped to identify the oxidation state of metal and EXAFS provided information regarding coordination environments.

From Figure 8-2 and Figure 8-3, two models for CuPt$_{0.2}$/SBA-15 and CuPt$_{0.05}$/SBA-15 are initially proposed, respectively. In the left panel of each figure, the models exhibited a single bimetallic Cu-Pt interstitial layer situated between the exterior shell and the Cu-rich core. Conversely, the right panel of the respective models showed the presence of discrete Pt atoms either on the surface or interspersed within the Cu-enriched nanoparticles. Upon the models for $CuPt_{0.2}$/SBA-15, XAS data revealed a Pt-Pt coordination number (CN) of approximately 6, and a Pt-Metal CN in the vicinity of 12. This evidence supported the hypothesis that platinum atoms segregate and are primarily situated within the bulk structure. Consequently, the proposed models depicted in the right panel appears to be more consistent with the observed phenomena. Regarding $CuPt_{0.05}$/SBA-15, XAS results shows a Pt-Pt CN to be around three, and a Pt-Metal CN near 9. These observations imply a segregation of Pt atoms and an increased presence of Pt atoms on the surface compared to $CuPt_{0.2}$/SBA-15. Consequently, the model depicted in the right panel of Figure 8-3 was considered to be more scientifically coherent. In summary, the models of $CuPt_{0.2}$/SBA-15 and $CuPt_{0.05}$/SBA-15, which align with our experimental findings, both demonstrated the presence of Pt atoms on the surface of the catalyst at RT. On the other hand, the coordination environment of Pt within the $CuPt_{0.005}$/SBA-15 catalyst exhibited interesting characteristics. The Pt-Pt CN is approximately two, while the Pt-Metal CN is around 8, and the Pt-Si CN is equal to or less than one. These observations implies that Pt atoms undergo segregation, are not located within the bulk, and interact with the support. Furthermore, the Pt-Cu CN of approximately 6 signifies that some Pt atoms are not situated at perimeter sites. Based on the findings above, a structural model was analyzed, as depicted in Figure 8-4. This model of $CuPt_{0.005}$/SBA-15 suggested the absence of Pt atoms on the surface at room temperature (RT) and the majority of Pt atoms residing at the SiO_2 interface.

In addition, our preliminary results have demonstrated that $CuPt_{0.005}$/SBA-15 exhibits the best activity for the hydrogenation reaction under room temperature. These results indicated that the SAA catalyst with no Pt atoms on the surface displays the highest activity. It appears that Pt atoms are dissociating H_2 molecules in a remote way. The nature of the interaction between Pt atoms and H_2 molecules is yet to be fully elucidated.

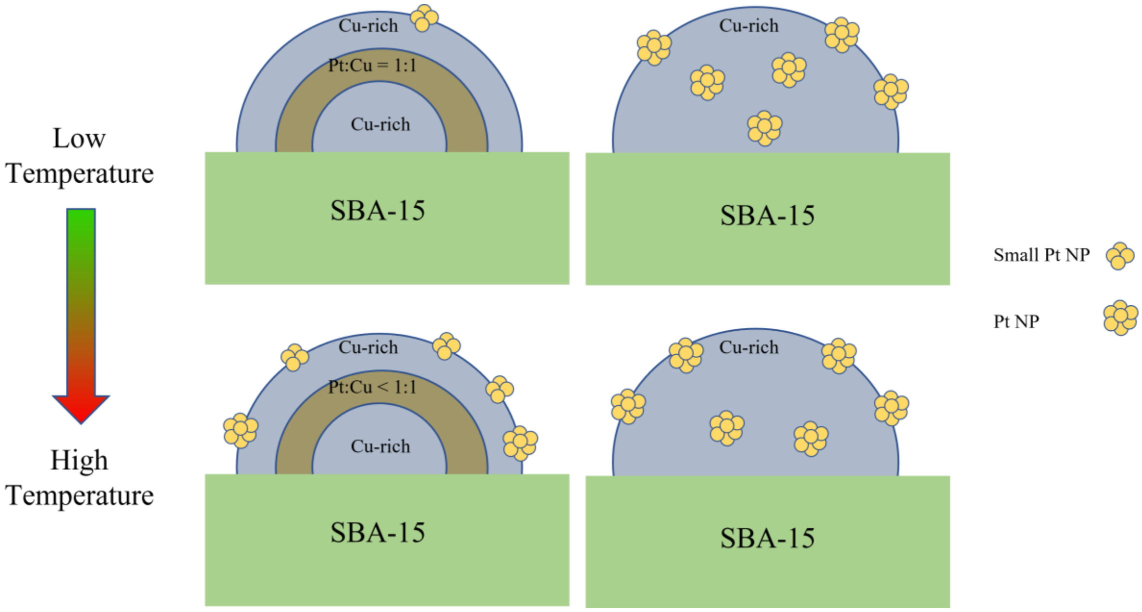

Figure 8-2. Models of $CuPt_{0.2}$/SBA-15, based on XAS results

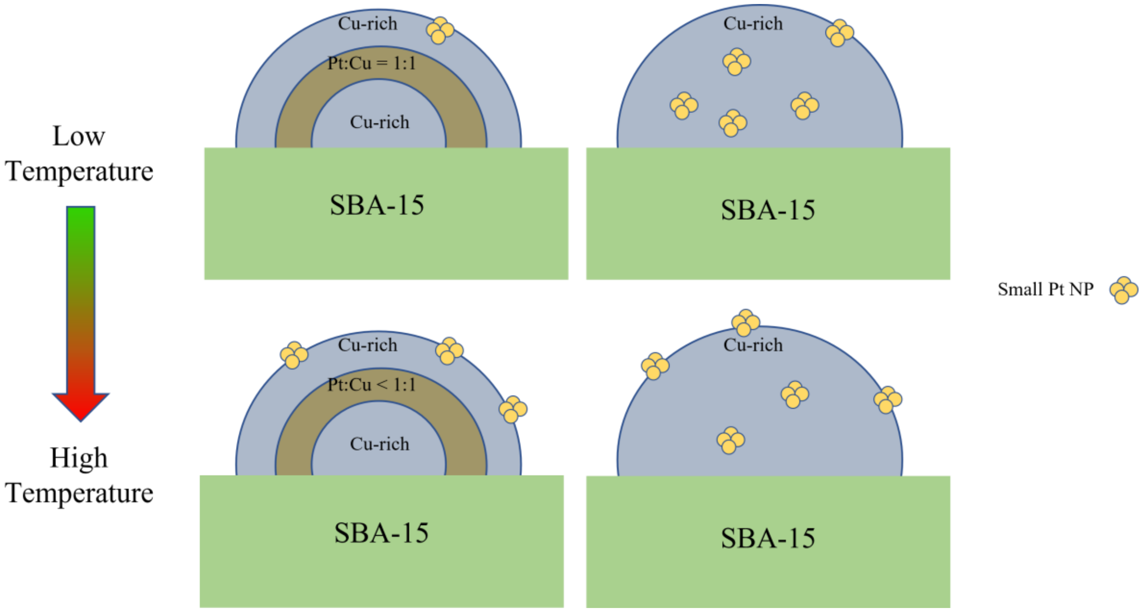

Figure 8-3. Models of CuPt$_{0.05}$/SBA-15, based on XAS results

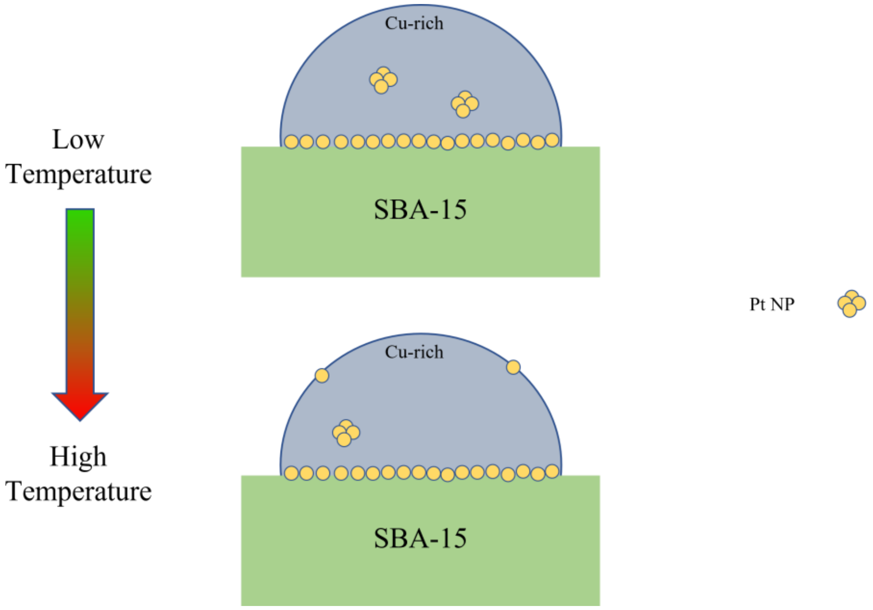

Figure 8-4. Models of CuPt$_{0.005}$/SBA-15, based on XAS results

The subsequent primary conclusions of the work are presented below.

First of all, in-situ IR and XAS studies of Cu-Pt bimetallic catalysts demonstrated the diffusion of Pt atoms within the nanoparticles under both vacuum and gaseous atmospheres. Results from CO adsorption experiments on $CuPt_x$/SBA-15 catalysts at low temperatures (125 K) revealed no Pt bonding, but heating to 225 K led to reversible segregation of Pt to the surface of high-Pt-content catalysts. The in situ IR study under the CO atmosphere indicated the reversibility of Pt segregation with temperature cycling between 295 K and 495 K, while the same trend was observed under H_2 atmosphere, albeit with some uncertainty due to interference from the CO probe molecule. XANES data showed that the change in gaseous atmosphere or temperature has an insignificant effect on the metallic and dispersed nature of Pt atoms or electronic structure. In the meantime, EXAFS analysis discovered a change in the coordination sphere of Pt atoms upon heating, namely, the ratio of Cu to Pt changed from 6:6 at 445 K to 8:4 at 495 K. This implies better intermetallic mixing at elevated temperature and possible additional surface segregation of Pt. These findings imply that the surface composition of Cu-Pt bimetallic catalysts is dynamic and temperature-sensitive in gaseous atmospheres.

Secondly, even though thermodynamic data have indicated the preference of bulk Cu to remain in metallic form under the hydrogen atmosphere, our result showed the metallic Cu catalysts became oxidized under such reducing conditions, resulting from the formation of a thin layer of oxidized copper, as indicated by a variety of techniques including in situ IR and XAS studies. However, our recent XAS results suggested such oxidation for Cu/SBA-15 and $CuPt_{0.05}$/SBA-15 under H_2 atmosphere may be avoided, contrary to previous observations. These results suggest that copper oxidation can occur under certain circumstances, even in reducing environments, although the specific circumstances have not been fully identified. The formation of oxide on the surface instead of the bulk and small NPs have a non-negligible impact on the associated thermodynamics. This is because the surface tension of metal oxides is lower than that of metals and if metal oxides are mixed with zero-valent metal solids, the oxide is expected to segregate to the surface. The probable scenario for low-temperature metal oxidation is the presence of small amounts of oxidizing impurities, in the H_2 feed. The formation of these thin oxide layers on Cu-based catalysts is an issue that needs to be kept in mind when designing Cu-based hydrogenation catalytic systems, especially as the catalytic hydrogenation of most organic reactants is typically carried out at low temperatures. However, it has been observed that oxygen-modified surfaces still hydrogenate unsaturated aldehydes with similar energetics and high selectivities as metallic substrates.

Thirdly, the thermodynamics of CO adsorption onto the Cu/SBA-15 metal surface was evaluated with in situ IR data in two distinct environments, under vacuum conditions and in the presence of atmospheric CO pressures. The results revealed significant disparities, with the enthalpy of adsorption estimated to range from $\Delta H°_{ads,vacuum} = –82$ kJ/mol to $\Delta H°_{ads,CO\text{-}atm} \sim – 21$ kJ/mol. This discrepancy could not be attributed to coverage effects, as low CO surface coverage calculations indicated that the enthalpy of CO adsorption actually decreased as coverage decreased, contrary to the typical observation in many other systems. In our conclusion, the observed change was instead attributed to entropic effects introduced by the presence of CO gas, including adsorbate displacement and adsorbate-assisted adsorption processes.

Last but not least, core-shell Pt@$Cu_{5.25}$/SBA-15 was successfully synthesized, evident by TEM, EDS, and in situ IR spectroscopy. In situ IR experiments indicated no Pt atoms on the surface even NPs were exposed to CO under 495 K. In addition, the development of our synthesis method was also discussed.

8.2 Future Work

8.2.1 Flow Reactor for In Situ IR Experiments

Our current in situ IR spectroscopy is limited to a certain stable gaseous atmosphere. In the future, we plan to run IR experiments with reactions under gas flow. For this reason, such a flow reactor is designed and will be assembled, as shown in Figure 8-5. In this reactor, we design to allow reactant flow through the reactor with other specific gas such as H_2 or O_2.

8.2.2 Further Investigation and Optimization of Core-Shell Catalysts

As mentioned in the previous chapter, our core-shell catalysts might have the limitation of Cu-only NPs on SBA-15. We are in the progress of confirming that and will work synthesizing Pt@Cu only nanoparticles onto SBA-15.

Additionally, in order to delve deeper into the mechanism of SAA catalysts and to explicate the reason for optimal activity in the absence of Pt on the surface, we plan to manipulate the thickness of the Cu shell. As shown in Figure 8-6, by varying the thickness, we aim to determine the optimal distance between Pt and H_2 molecules for hydrogenation reactions. Subsequently, we intend to investigate the mechanisms underlying these remote interactions.

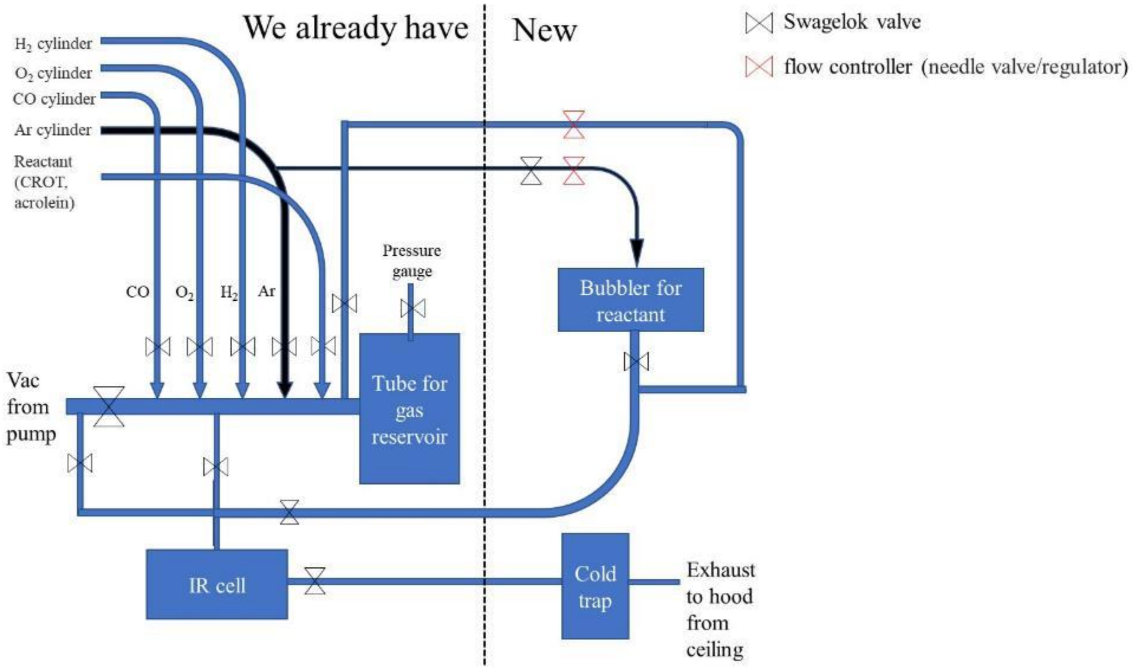

Figure 8-5. Setup for gas flow reactor for in situ IR spectroscopy

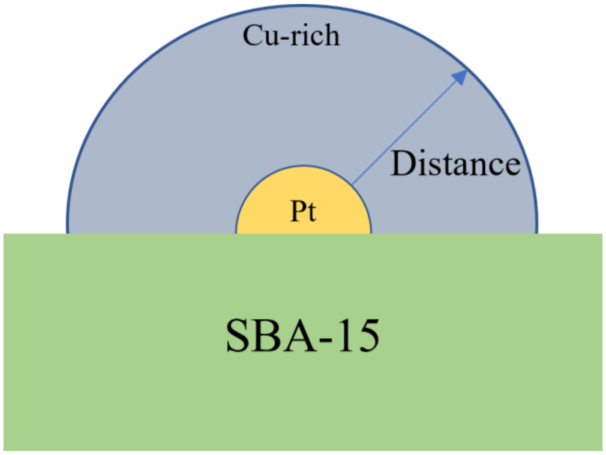

Figure 8-6. Core-shell Pt@Cu_x/SBA-15 catalyst

8.3 References

1. Bauer, K.; Garbe, D.; Surburg, H., *Common fragrance and flavor materials: preparation, properties and uses*. John Wiley & Sons: 2008.

2. Weissermel, K.; Arpe, H.-J., *Industrial organic chemistry*. John Wiley & Sons: 2008.

3. Hannagan, R. T.; Giannakakis, G.; Flytzani-Stephanopoulos, M.; Sykes, E. C. H., Single-Atom Alloy Catalysis. *Chemical Reviews* **2020,** *120* (21), 12044-12088.